

AD-A266 626



2



**Mississippi State**  
UNIVERSITY

Technical Report 93-1  
1 July 1993

**Center for Air Sea Technology**

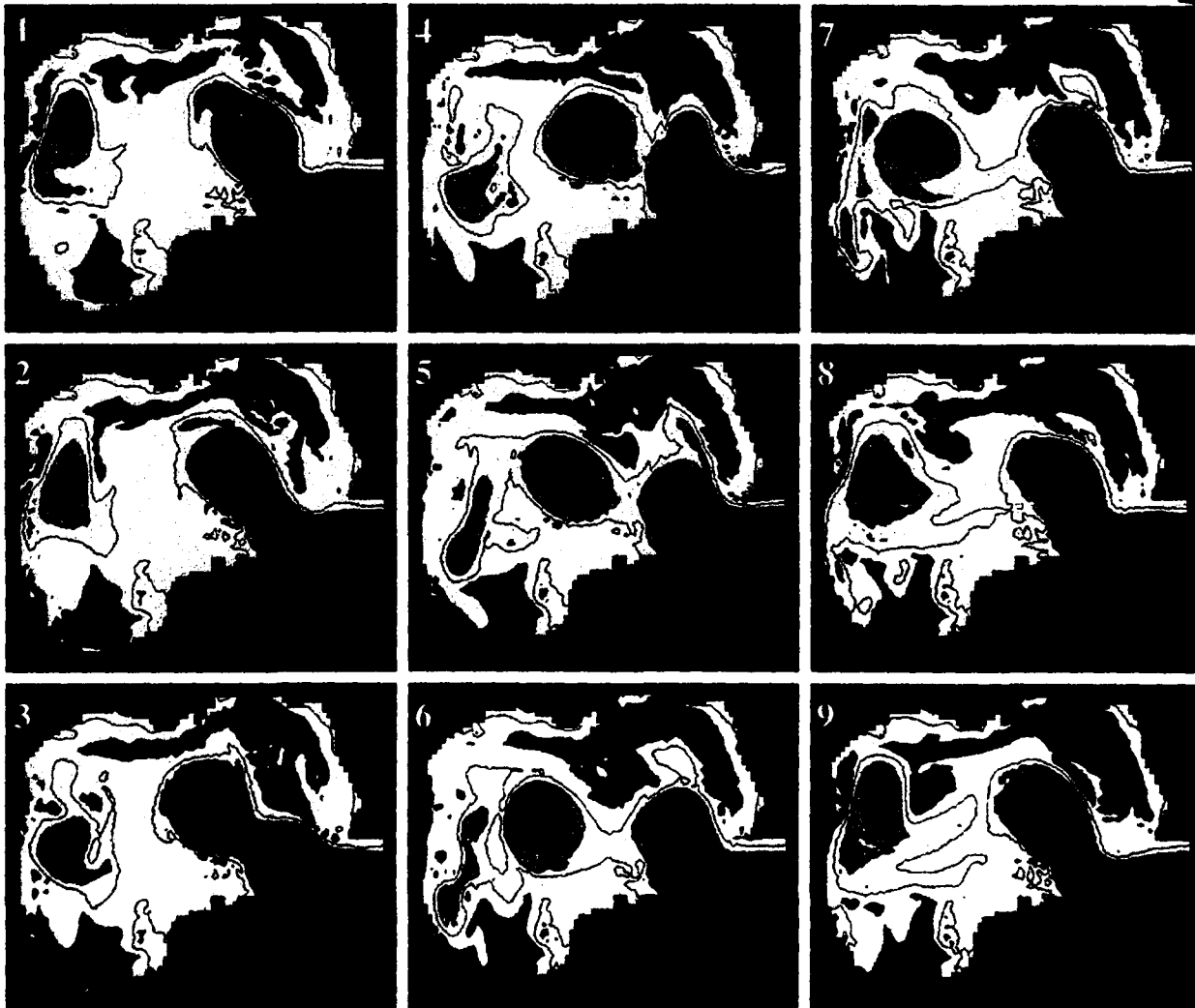
Stennis Space Center, MS 39529-6000

**ON THE APPLICATION AND EVALUATION OF THE  
RELOCATABLE DIECAST OCEAN CIRCULATION  
MODEL IN COASTAL AND SEMI-ENCLOSED SEAS**

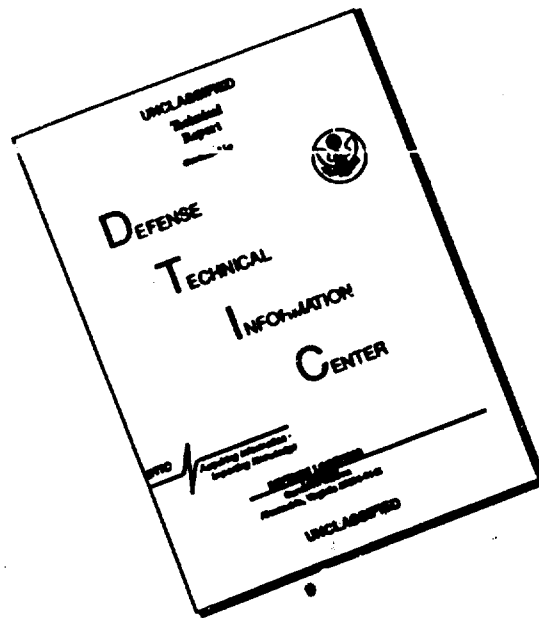
by

David E. Dietrich, Dong-Shan Ko, and Lanny A. Yeske

**S**  
DIED  
ELECTE  
JUL 09 1993



# DISCLAIMER NOTICE



**THIS DOCUMENT IS BEST  
QUALITY AVAILABLE. THE COPY  
FURNISHED TO DTIC CONTAINED  
A SIGNIFICANT NUMBER OF  
PAGES WHICH DO NOT  
REPRODUCE LEGIBLY.**

**COVER:** DieCAST model output of sea-surface temperature at 30 day intervals in the Gulf of Mexico showing an eddy shedding event.

## ADDENDUM

The cover shows a model output surface temperature sequence from a Gulf of Mexico run. The run is identical to Case B3 of Sections 3.1 and 5.3 except the lateral momentum diffusivity is ten times larger ( $200 \text{ m}^2/\text{sec}$ ). The panels are 30 days apart. The run (with Prandtl number equal to 10) thus approximately emulates layered models, which generally have small or zero thermal diffusivity, while having finite momentum diffusivity. The increased lateral momentum diffusivity reduces the amplitude of paired cool core cyclonic recirculation eddies that are observed in the western Gulf of Mexico. Increasing lateral heat diffusivity to  $200 \text{ m}^2/\text{sec}$  eliminates them. In such higher diffusivity cases, the old warm core western GOM eddies elongate along the shelfbreak as they dissipate. The substantial effects of Reynolds number on GOM dynamics is discussed further in this report. Color VHS animation of the Case B3 model results and model output data are available on request.

All GOM runs in this report were done on a Silicon Graphics workstation using approximately 20 km lateral resolution with 20 layers ( $83 \times 60 \times 20$  grid) and depths truncated at 3.5 km. In the South China Sea run (Section 6.1) with 110-element vectors, the model runs at over 205 megaflops on a single Cray YMP pipe. This is equivalent to less than 2 minutes per layer per model year with our GOM resolution (comparable to the fastest ocean models). The entire model vectorizes and over 99 percent of it compiles to parallel vectors. No modifications of the original SOMS model were required to achieve this full vectorization and parallelization by the Cray YMP compiler.

The version of the model used here assumes constant horizontal grid increments while using the actual latitudinal Coriolis parameter distribution. The latitudinal increment is about 22 km, while the longitudinal is about 18 km. The latter is slightly less than the minimum (about 19 km) that would occur on a true sphere at the northern GOM boundary (based on  $1/5$  degree spacing of the bathymetry data used). This reduces the port separation between the Yucatan and Florida Straits by about 10 percent. A fully spherical version of our model is also available.

**TECHNICAL REPORT 93-1**

**ON THE APPLICATION AND EVALUATION OF THE  
RELOCATABLE DIECAST OCEAN CIRCULATION MODEL IN  
COASTAL AND SEMI-ENCLOSED SEAS**

by

**David E. Dietrich <sup>1</sup>, Dong-Shan Ko<sup>2</sup>, and Lanny A. Yeske<sup>1</sup>**

**<sup>1</sup>Senior Research Scientist, Mississippi State University Center for Air Sea  
Technology, Stennis Space Center, MS 39529-6000**

**<sup>2</sup>Research Scientist, Rosenstiel School of Marine and Atmospheric Sciences,  
University of Miami, 4600 Rickenbacker Causeway, Miami, FL 33149-1098**

**1 July 1993**

This research was supported by the Department of the Navy, Office of the Chief of Naval Research under Cooperative Agreement N00014-90-CA-0001 with the Institute for Naval Oceanography and Research Grant N00014-92-J-4109 with Mississippi State University. The opinions, findings, conclusions, and recommendations expressed in this publication are those of the authors and do not necessarily reflect the views of the U.S. Government. No official endorsement should be inferred.

**93 7 08 06 7**

**93-15471**



## ABSTRACT

To improve coastal and semi-enclosed seas modeling, a new ocean model called DieCAST (Dietrich-Center for Air Sea Technology) has been developed. In application to the Gulf of Mexico (GOM), this model gives remarkably similar results to that obtained from the Sandia Ocean Model System (SOMS) and at a computational speed much faster than SOMS or other ocean models presently applicable using high coastal resolution.

In this report, the effects of lateral diffusivity, resolution, and other parameters on SOMS and DieCAST modeled Gulf of Mexico eddies are explored. Results show: (1) that diffusivity on the order of 100 m<sup>2</sup>/sec or larger significantly decreases maximum velocity and frontal intensity, and greatly decreases the amplitudes of modeled paired eddies near the western GOM shelfbreak similar to those observed; and (2) that at least 10 km resolution is needed for accurate modeling of nonlinear interactions and dissipation of paired eddies.

In addition, shelf resolving GOM and northwestern Caribbean simulations show significant interactions between the deep water and continental shelf flows. Separation of cool positive vorticity shelf water leads to cold core cyclonic eddies on the north side of old Loop Current eddies in the western GOM. It also leads to cold core cyclonic eddies that can block Loop Current penetration and delay or halt eddy shedding. Reducing lateral diffusivities amplifies this effect. Bottom drag induced secondary flows contribute to this cool positive vorticity shelf water. Fronts near continental shelfbreaks result from secondary flows and are related to enhanced western GOM eddy activity. Significant nonlinear interaction occurs between small-scale shelf processes and mesoscale deep water paired eddies. Recently separated shelf water can accumulate in nonlinear critical areas, where advection and Rossby wave propagation are roughly in balance, and organize into larger-scale deep water paired eddies.

The results are supported by many GOM observations including GEOSAT rms sea surface height anomaly data; mean thermocline and empirical orthogonal functions; the evolution of vortex pairs in the western GOM; major Loop Current eddy shedding period; shed eddy size, phase speed, dispersion rate and vorticity; detailed Loop Current and shed eddy structure such as a shallow cool pool near the top surface and small-scale vertically coherent oscillations of temperature surfaces under separated Caribbean western boundary current water; and a cool core eddy on the order of 100 km near the Florida shelfbreak during eddy shedding.

DieCAST is easily relocated to any geographical region of the globe. Preliminary applications in several regions such as the Mediterranean, South China Sea, Great Lakes, and Labrador Current are described.

The SOMS and DieCAST models are unique in that they are robust with raw (unfiltered) real topography and with very low (realistic) dissipation. DieCAST requires about 250 operations per grid point per time step and is stable with a 45 minute time step and 20 km horizontal resolution in the GOM. It fully vectorizes on the Cray YMP. On a single vector pipe, this gives over 205 megaflops. Use of parallel multiple pipes should also be efficient, because over 99 percent of the model calculation compiles to parallel vectors.

DTIC COPY AVAILABLE 3

Accession for	
NHS OSA&I	<input checked="" type="checkbox"/>
DTIC TAB	<input type="checkbox"/>
Unannounced	<input type="checkbox"/>
Justification	
By	
Date	
Dist	
A-1	

## TABLE OF CONTENTS

	<u>Page</u>
1. INTRODUCTION .....	1
2. DESCRIPTION OF THE DIECAST MODEL .....	1
3. VALIDATION AND COMPARISON OF THE DIECAST AND SOMS MODELS IN THE GULF OF MEXICO (GOM) .....	2
3.1 Extensive Comparison of the SOMS Model with Observations .....	2
3.2 Comparison of the SOMS and DieCAST Models .....	9
3.3 Further Discussion .....	12
4. MODEL PARAMETER SENSITIVITY STUDIES USING GOM EDDIES .....	12
4.1 Lateral Diffusivity Effects on Paired Eddy Formation .....	13
4.2 Other Dissipative and Dispersive Effects .....	17
4.3 Resolution Effects .....	20
5. NUMERICAL STUDIES OF THE GOM GENERAL CIRCULATION AND COMPARISONS WITH OBSERVATIONS .....	31
5.1 Model Formulation .....	32
5.2 Effects of Lateral Diffusivity on Eddy Shedding .....	33
5.3 Simulations Based on Detailed Caribbean Inflow Observations .....	38
5.4 Further Interpretation of Results .....	51
5.5 Truncation Error Effects .....	54
6. PRELIMINARY APPLICATIONS OF DIECAST IN THE SOUTH CHINA SEA, STRAIT OF SICILY, LABRADOR CURRENT, AND GREAT LAKES .....	54
6.1 South China Sea .....	55
6.2 Labrador Current .....	55
6.3 Strait of Sicily .....	55
6.4 Great Lakes .....	55
7. CONCLUDING REMARKS .....	59
APPENDIX I .....	61
APPENDIX II .....	61
ACKNOWLEDGEMENTS .....	62
REFERENCES .....	62

## 1. INTRODUCTION

There is a need for better coastal and semi-enclosed seas models, particularly of the interaction between continental shelf and deep water flows. The exchange of deep water with shallow continental shelf water is important in carbon cycle issues and large-scale circulations as well as in coastal pollution studies and military operations. Shelfbreak fronts, boundary current separation, and paired counter-rotating eddies in and near continental shelf regions play significant roles in this exchange.

There is also a major need for a numerical ocean model that is easily relocatable to any given region in the world, and in particular coastal and semi-enclosed seas. Present methods to accomplish relocation are not only complex, but are slow and tedious as well. These needs have spurred the development by Mississippi State University (MSU) of the DieCAST Ocean Model under sponsorship of the Navy Ocean Modeling and Prediction Program (NOMP). The development of DieCAST is an integral part of the MSU CAST research program under NOMP. Not only does this research seek to enhance coastal and semi-enclosed seas (or larger scale) modeling efforts, DieCAST is also used by CAST in its technology support tasks of: (1) Data Management and Consolidation for Ocean Model Initialization and Evaluation, (2) Objective Ocean Model Verification and Evaluation, (3) Scientific Visualization for Model Evaluation, and (4) Advanced Development/Transitions.

In this report, the DieCAST Model is described in Section 2. The validation and comparison of the DieCAST and Sandia Ocean Modeling System (SOMS) models in the GOM is presented in Section 3. In Section 4, the results of relatively short time parameter sensitivity studies with modeled eddies are discussed. Section 5 highlights shelf-resolving numerical studies of longer term GOM circulations using SOMS, including extensive and favorable comparisons with many GOM observations. Finally, Section 6 shows early results with the easily relocatable DieCAST Model configured for various geographical regions including the Mediterranean

Sea, South China Sea, Great Lakes, and the Labrador Current.

## 2. DESCRIPTION OF THE DIECAST MODEL

The governing equations upon which the model is based are as follows:

For longitudinal momentum conservation,  
$$u_t = -p_x + f_v - \nabla \cdot (u\underline{v}) + (CX u_x)_x + (CY u_y)_y + (KM u_z)_z.$$

For latitudinal momentum conservation,  
$$v_t = -p_y - fu - \nabla \cdot (v\underline{v}) + (CX v_x)_x + (CY v_y)_y + (KM v_z)_z.$$

For internal energy conservation,  
$$T_t = -\nabla \cdot (T\underline{v}) + (CX T_x)_x + (CY T_y)_y + (KH T_z)_z.$$

For salinity transport equation,  
$$S_t = -\nabla \cdot (S\underline{v}) + (CX S_x)_x + (CY S_y)_y + (KS S_z)_z.$$

For hydrostatic approximation of vertical momentum conservation,

$$P_z = (\rho - \bar{\rho}^{x,y}) g.$$

For incompressibility,

$$\nabla \cdot \underline{v} = 0.$$

For equation of state,

$$\rho = \rho(S,T)$$

The DieCAST Model evolved from the free-stream submodel of SOMS, which uses an Arakawa "c" staggered grid, as described by Dietrich et al. (1987), Dietrich (1992), and Dietrich (1993). DieCAST is a refined and extended version of the laterally "semi-located" modified Arakawa "a" grid approach described by Dietrich et al (1990). The "a" grid has advantages in lateral-boundary-fit curvilinear coordinates. These coordinates have potentially great advantages in coastal and semi-enclosed seas modeling.

DieCAST is a hydrostatic, incompressible, rigid-lid, partially implicit, fully conservative ocean and lake model. The numerical differences from the SOMS model stem only from using an Arakawa "a" grid instead of the Arakawa "c" grid.

DieCAST solves all conservation equations on a common grid of cell-centered control volumes. The incompressibility (mass conservation) equation and pressure gradient terms, which are the weak points of colocated grids, receive special treatment as follows.

A special contravariant horizontal advection velocity is defined by using fourth order interpolations of the covariant cell centered results to the conventional staggered Arakawa "c" grid locations. The incompressibility of the staggered advection velocity is then satisfied by removing the divergence using a hydrostatic elliptic pressure adjustment that is identical to the method in SOMS and similar to the one described by Dukowicz and Malone (1992). The resulting overall advection scheme for the transport of scalar cell-centered quantities is identical to SOMS. It is fully conservative, including quadratic energy related quantities.

Similarly, the pressure gradient is approximated by fourth order differences. These use grid data spaced over four full grid intervals on the colocated grid. For well-resolved flow components, these approximations are more accurate than the standard second order Arakawa "c" grid approximations using data spaced over one grid interval.

The less accurate small-scale flow components are also robust with the DieCAST fourth order pressure gradient. As with SOMS, DieCAST requires very little total dissipation for numerical stability. Although boundary points are less accurate, this can be compensated by a lateral-boundary-fit version under development.

The DieCAST model includes several features not originally in SOMS. First, nearly all controlling parameters are read from files created by a front end program. The only exceptions are the resolution parameters, which must match those set in the front end. This streamlines DieCAST and avoids the need to recompile for any parameter changes.

Second, a flexible open lateral boundary condition procedure has been automated for all points along the closed rectangular domain boundary determined by the model resolution

parameters. Points on land are automatically excluded from this procedure by masking arrays. The remaining points are treated by a combination of climatology, modified upwind and integrated volume flux constraints. This is done using a streamlined procedure that can be vectorized. All boundary values, except normal advection velocity at the boundary, use a modified upwind approach with external values, when needed, specified from climatology. At present, only advection normal to the boundary is considered, but full upwind can be implemented. The normal advection velocity on the boundary is relaxed toward climatology on a long-time scale. It is also relaxed toward upstream values on a much shorter time scale, but only for outflow. A full upwind approach can be implemented for the latter, if desired.

### **3. VALIDATION AND COMPARISON OF THE DIECAST AND SOMS MODELS IN THE GULF OF MEXICO (GOM)**

#### **3.1 Extensive Comparison of the SOMS Model with Observations**

The GOM is an extensively observed ocean basin. It is dominated by a 25 Sverdrup Loop Current that feeds into the Gulf Stream after passing through the Florida Strait. The Loop Current sheds major eddies that propagate westward and dominate the western GOM circulation.

Previously, the SOMS Model has been successfully applied with high lateral resolution (263 m) to Lake Neuchatel (Dietrich and Zuur, 1990) and demonstrated grid convergence in resolution sensitivity experiments with a prototype ocean problem (Dietrich, et al, 1990). SOMS was also recently applied to a series of GOM studies as described by Dietrich and Lin (1993) and in Section 5 of this report.

Here we compare Case B3 of Section 5 extensively with observations. Further details are given in Section 5. Case B3 uses 20 layer vertical and 20 km horizontal resolution and is run for seven model years with prescribed time independent inflow into the Caribbean patterned after observations (Schmitz and

Richardson, 1991). Open outflow conditions are prescribed in the Florida Strait. Local wind forcing and thermohaline effects are ignored. Inflows are switched on full amplitude the first time step. The results show shed eddy size (300 km), phase speed (4 cm/sec), and mean shedding period (254 days) that are close to observations and theory.

Figures 1 through 5 compare various aspects of a single model run (Case B3) with corresponding observations. For a discussion of our approach to contouring graphics, see Appendix I to this report. Figure 1 compares model results with rms sea surface height anomaly derived from satellite altimetry. Major features are in close agreement. Figures 2 and 3 compare the mean thermocline and empirical orthogonal functions (EOF) derived from the full history of available GOM data. Only winter data is included, because the winter surface mixed layer corresponds to the zero surface stratification resulting from the insulated surface condition used by the model. The model accurately simulates the mean thermocline. The model's deep water temperature is 6°C in both the initial conditions and the water entering the Caribbean, rather than the 5°C observed. The linear equation of state used in this study gives a bottom density at 6°C equal to the true nonlinear value at 5°C.

Figure 3 compares model EOF modes for vertical temperature profiles, derived from Case B3, with the EOF modes derived from observations (Ko, 1992). The observations are derived from all available seasonal data in deep water locations. Above 500 meters depth, the model functions are quite similar to those observed. Remarkable is the agreement of the higher order modes 4 to 7 in this region, because they contain relatively little energy and thus are most susceptible to observation errors. This agreement suggests that the observation errors have little effect even on these modes, so the EOFs from observations are probably quite reliable. It also shows that deep water wind driving effects, not included in the model simulations, are quite secondary, because the response to wind driving is mainly in a thin mixed layer with highly time dependent thickness. The main difference between the model functions and those

observed is that the model functions generally have larger amplitudes in the 500 to 1500 m depth range. This is a region where the model thermal stratification is less than the observations, because of the initial and boundary conditions used, which can favor stronger and deeper eddies resulting from baroclinic instability.

The Figure 4 series (a through c) compares model results with a very extensively studied eddy (Forristall, et al, 1992), and shows that even secondary features are realistically represented in the model. Figure 4a shows a vertical cross-section of a recently separated Loop Current eddy from Case B3. The structure revealed is typical of recently shed eddies in the model results. It is strikingly similar to the cross-section from the fast eddy shown by Forristall, et al (1992). This similarity even includes such details as the amplitude and location of the kink in the isotherms in the outer part of the Loop Current (for example, the 8 and 7 degree isotherms change depth O(50)m in about 30 km distance in cross-sections through the central part of the eddy), and the shallow pool of cool water (upward bending 26°C isotherm and downward bending of the below 26°C isotherms). The cool surface water above the warm central core is also evident in results presented later. Although the observed eddy is quite asymmetric because of its recent smaller ghost eddy shedding, previous observations of recently shed eddies (Elliott, 1982; Kirwan and Lewis, 1987) generally show similar structure.

The thin strongly stratified surface layer in the observations does not occur in the model results. It is a result of summer heating not included in the model simulation. Such an increased stratification layer can have significant effect on eddy shedding.

There are many interesting features in the Figure 4 series. The upward bowing of the 26 degree isotherm in Figure 4a probably reflects the broad upwelling in the upper levels of the Loop Current core indicated by Figure 4b. (Vertical velocity is negative for upward motions.) During the Loop Current northward penetration, this bowing increases along with maximum Loop Current speeds,

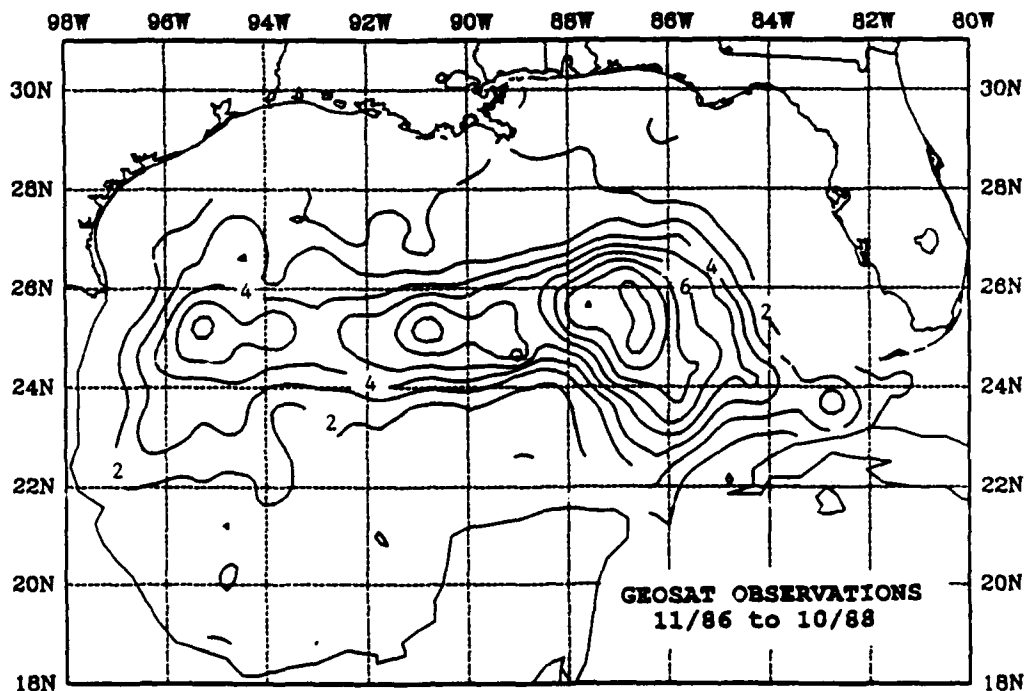
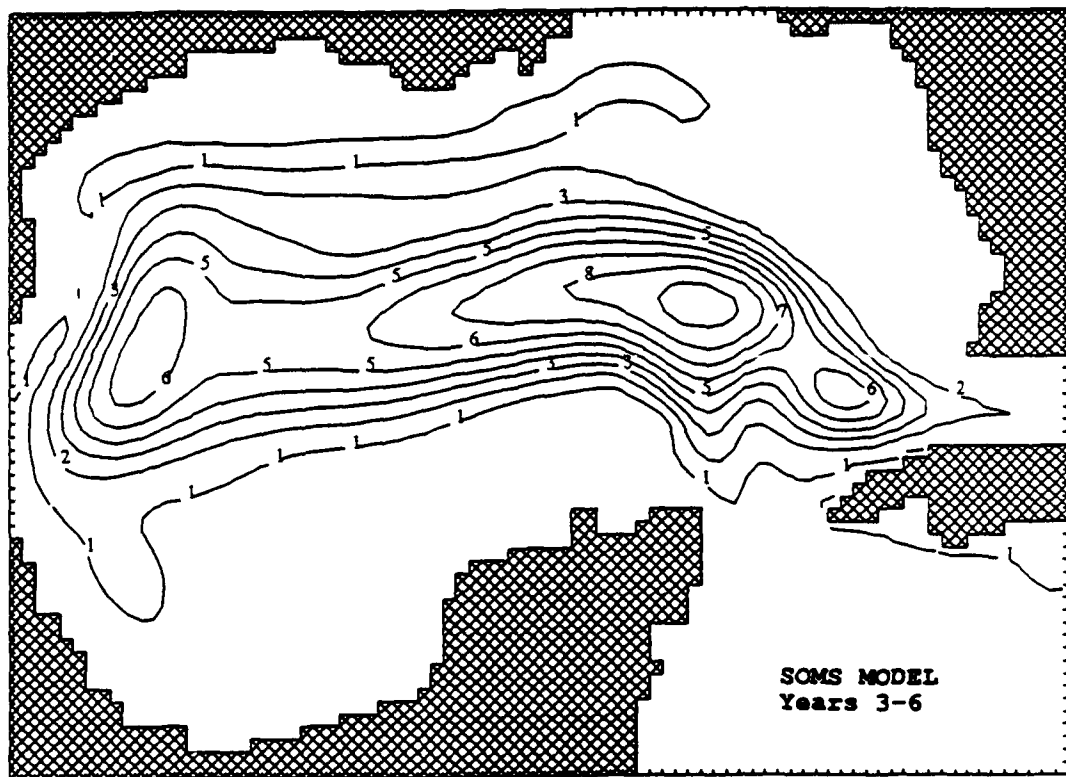


Figure 1. Comparison of model and observed RMS sea surface height anomaly. Both plots have a 2.5 cm contour interval. To obtain rms height in centimeters multiply the single-digit contour labels by 2.5. The model equivalent sea surface height is derived hydrostatically from top level pressure.

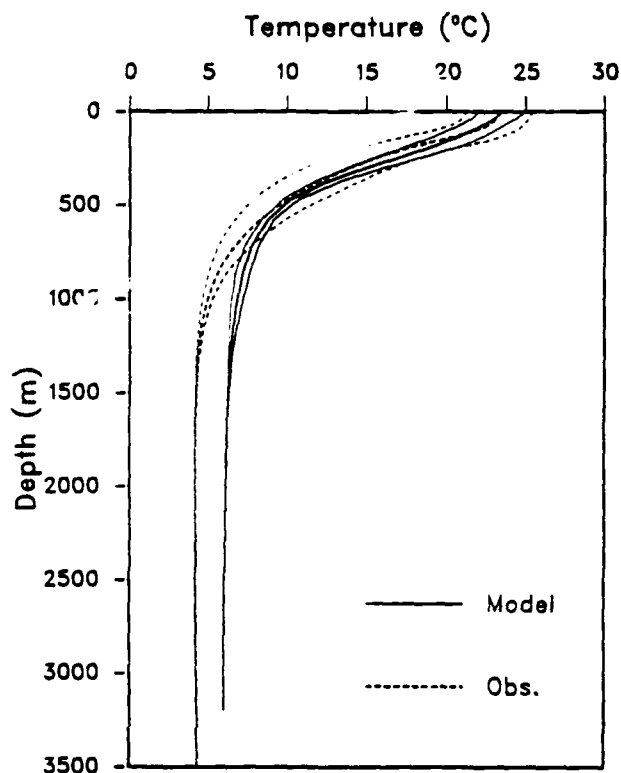


Figure 2. Comparison of model and observed winter time vertical temperature profiles. These are laterally and time averaged. Standard deviations are also shown. The thermally insulated free surface condition used in this particular calculation results in a well-mixed surface layer profile.

especially during the late stages just before eddy separation. Although upwelling occurs in the central core, leading to locally cool upwelling water, the downwelling of cooler water recently separated from the Yucatan Shelf near the outer edges of the Loop Current also shown by Figure 4b, results in a net decrease of potential energy consistent with the increased kinetic energy. There is net positive pressure work because the divergence at the surface occurs at higher pressure than the convergence into the core below. Although baroclinic instability can occur at the Loop Current front, this potential energy reducing direct circulation is not clearly related to baroclinic instability, because it involves Yucatan Shelf boundary current separation.

This implied quasi-axisymmetric vertical circulation in the upper levels of the Loop Current is very likely consistent with quasi-

geostrophic dynamics governed by the omega equation (Dietrich and Lin, 1993). For such consistency, bottom drag and vertical diffusion terms must be appropriately included in the forcing function, as explained below.

The Yucatan shelf bottom boundary layer is dominated by a balance among bottom drag, Coriolis acceleration, and pressure gradient forces. For high Reynolds number flow, it separates near the westward bend of the Yucatan depth contours. The bottom drag thus disappears quickly. This leads to high frequency oscillations and a net westward displacement of the separated water. The oscillations are not of much interest because their energy disperses rapidly, and they lead to little net displacement on general circulation time scales. While the omega equation filters them, it is useful for interpreting observations. It includes longer term effects such as the net westward displacement which is accompanied by sinking of the coolest water from the Yucatan shelf near the Loop Current front. Thus vortex stretching occurs. Positive vorticity advection limits this sinking, so the front does not disappear. A similar phenomenon occurs when the Florida shelf water separates just upstream of the Florida Strait. Thus, there is a net outward movement from the upper Loop Current core, which increases the velocity in the separated Loop Current because of the Coriolis terms and creates a shallow upper level pool of upwelled cool water.

The aforementioned vertically coherent kink in the isotherms underlies the separated Caribbean western boundary current water. This is shown by the vorticity distribution in Figure 4b, which clearly indicates the positive vorticity water recently separated from the Yucatan shelf. As noted above, the separated water is locally unbalanced, resulting in locally strong downwelling, which changes the pressure throughout the water column because of the hydrostatic relation. This requires geostrophic adjustment in deeper water, leading also to vertical circulation. The vertical circulation is amplified by the reduced deep water stratification, as governed by the omega equation. This is shown by the vertical velocity in Figure 4b. Further, the separated boundary water has locally large

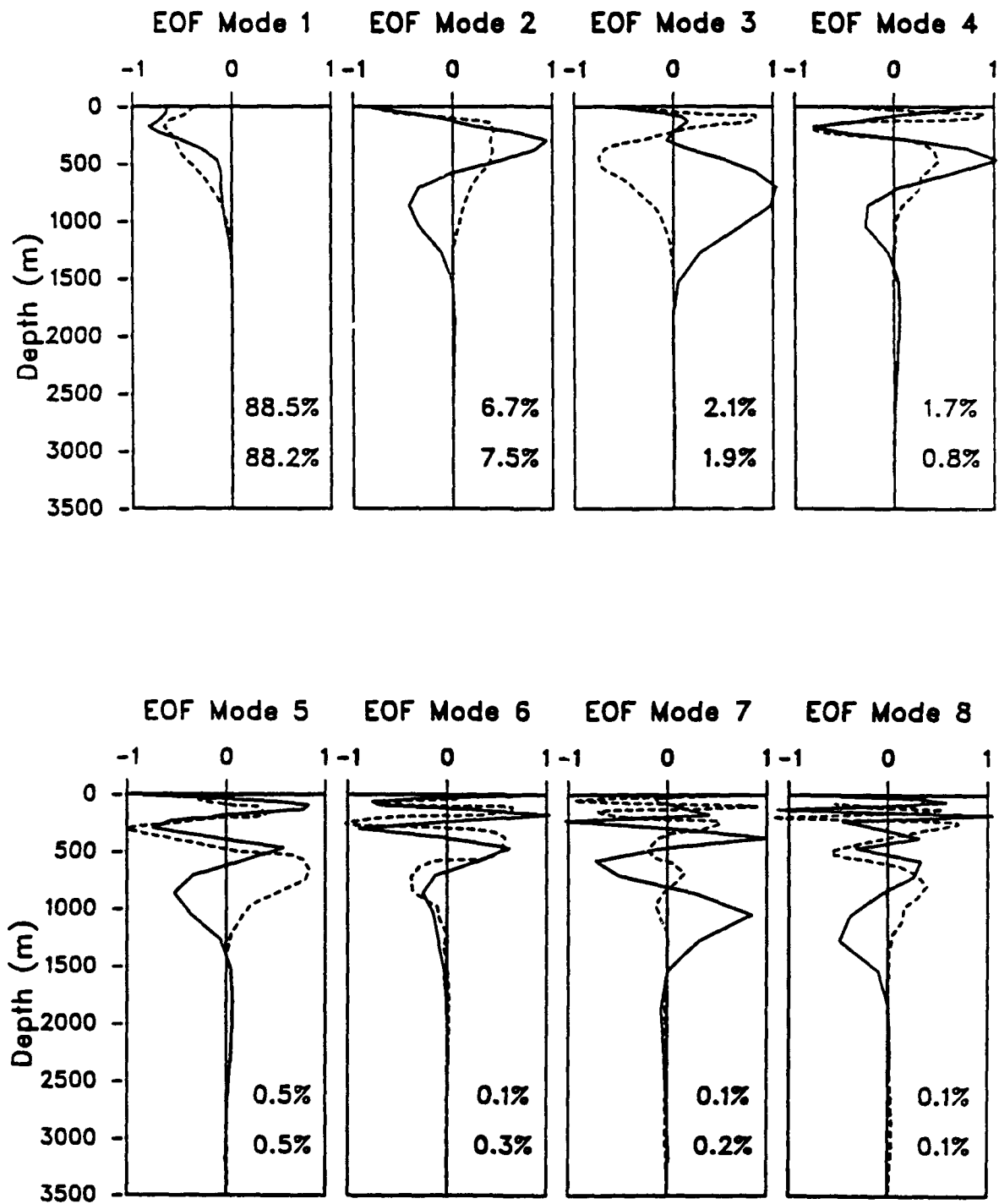


Figure 3. Comparison of model vertical EOF modes (solid lines) with those from observations (dashed lines). The percent of total variance represented by each EOF mode is given in each panel, with the observation value located above the model value.

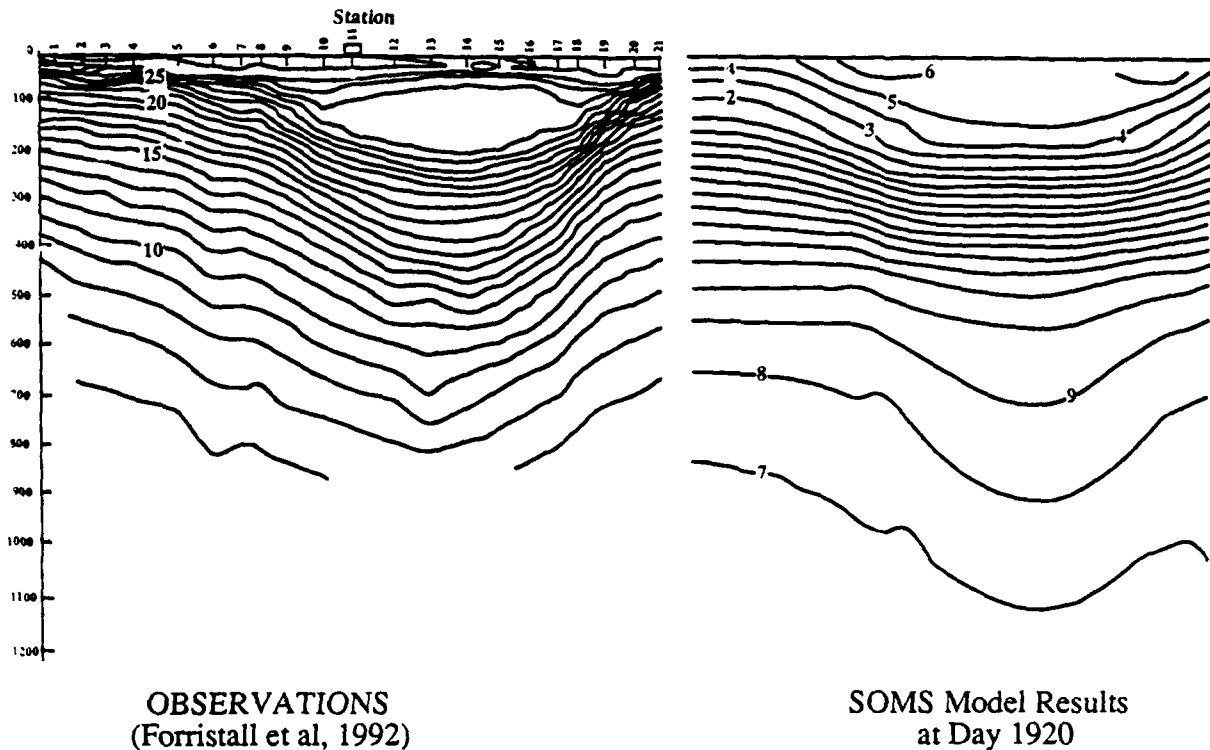


Figure 4a. A vertical cross-sections of temperature ( $^{\circ}\text{C}$ ) through a recently shed Loop Current eddy. The observations and model cross-sections have the same vertical and horizontal scales. The horizontal scale is approximately 400 km. The observations are from a NE-SW slice through the eddy. Model results are from a longitudinal-depth cross-section through the Loop Current core. Temperatures in the model results are given mod (10); thus the "6" isotherm near the top surface represents  $26^{\circ}\text{C}$ , while the "7" isotherm near 900 m depth represents  $7^{\circ}\text{C}$ .

vertical gradients of vorticity and density advection, with small lateral scale. Under such conditions, the maintenance of quasi-geostrophic flows by vertical motions, governed by the quasi-geostrophic omega equation, implies overturning with small lateral scale. The details of the resulting vertical motions depend on time and angular location around the shed eddy, so exact correspondence with observations in Figure 4a is not expected. However, qualitative correspondence reflects the realistic behavior of the SOMS model even for these detailed features.

Larger scales become more dominant as the separated Loop Current eddy moves away from the Yucatan. This is indicated by Figure 4c. The deep water vertical motions are consistent with a dominant beta term in the omega equation.

Figure 5 compares Case B3 results to observations of a paired eddy formation in the western GOM reported by Brooks and Kelly (1986). They are qualitatively similar to other eddy interactions with the western GOM shelfbreak in the Case B3 discussed later. Case B3 is characterized by low lateral diffusivities ( $20 \text{ m}^2/\text{sec}$ ) and 25 Sverdrups volume flow rate into the Caribbean. This gives an  $O(10^4)$  Loop Current Reynolds number. The good comparison is remarkable because the model calculation assimilated no real data. These extensive model comparisons with observations make Case B3 one of the most extensively validated runs ever in ocean modeling.

The SOMS model gives these realistic GOM results with reasonable computing requirements. These results were calculated using one processor of an SGI 4D/340 GTXB

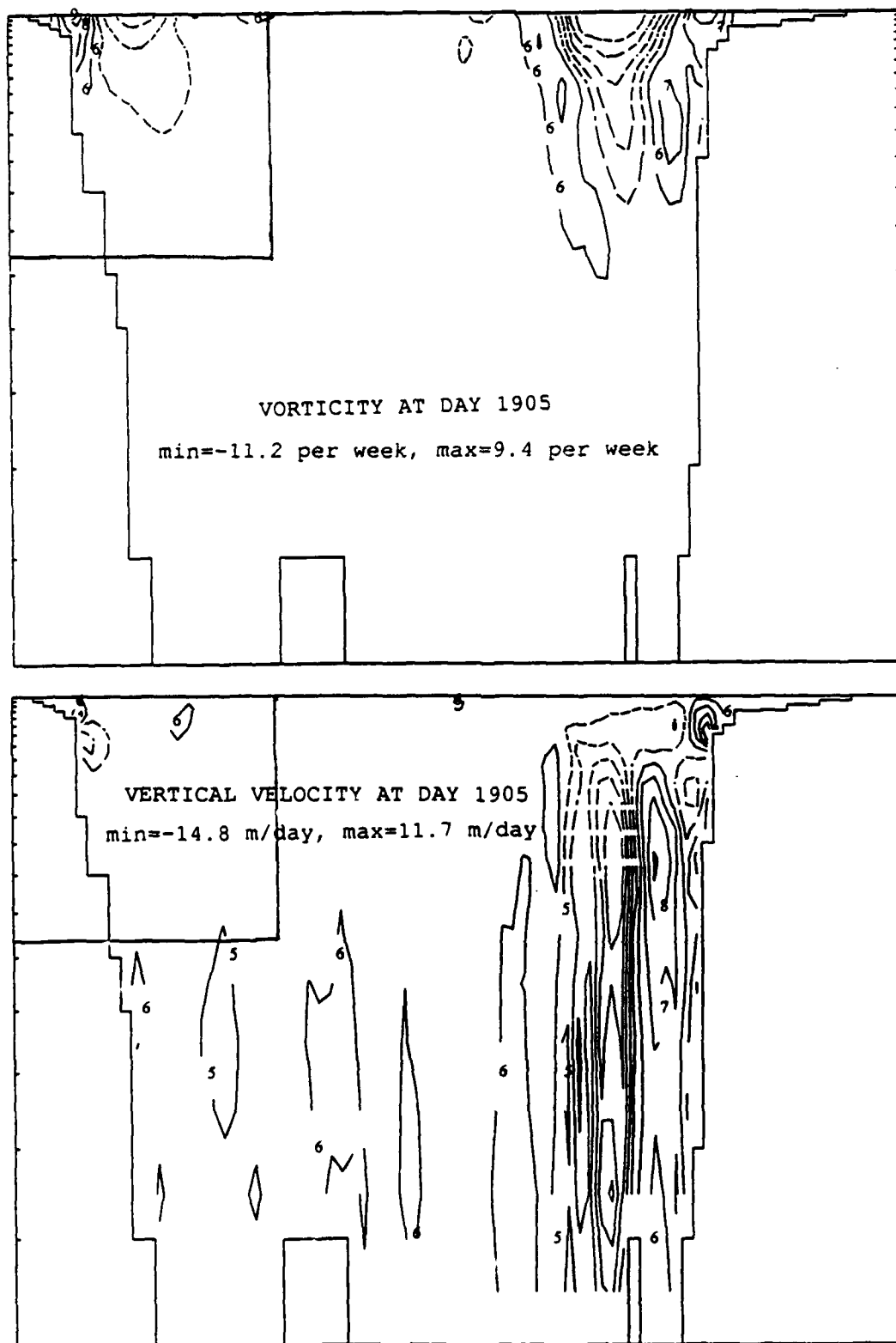


Figure 4b. Vertical cross-sections at the same latitude as in Figure 4a.

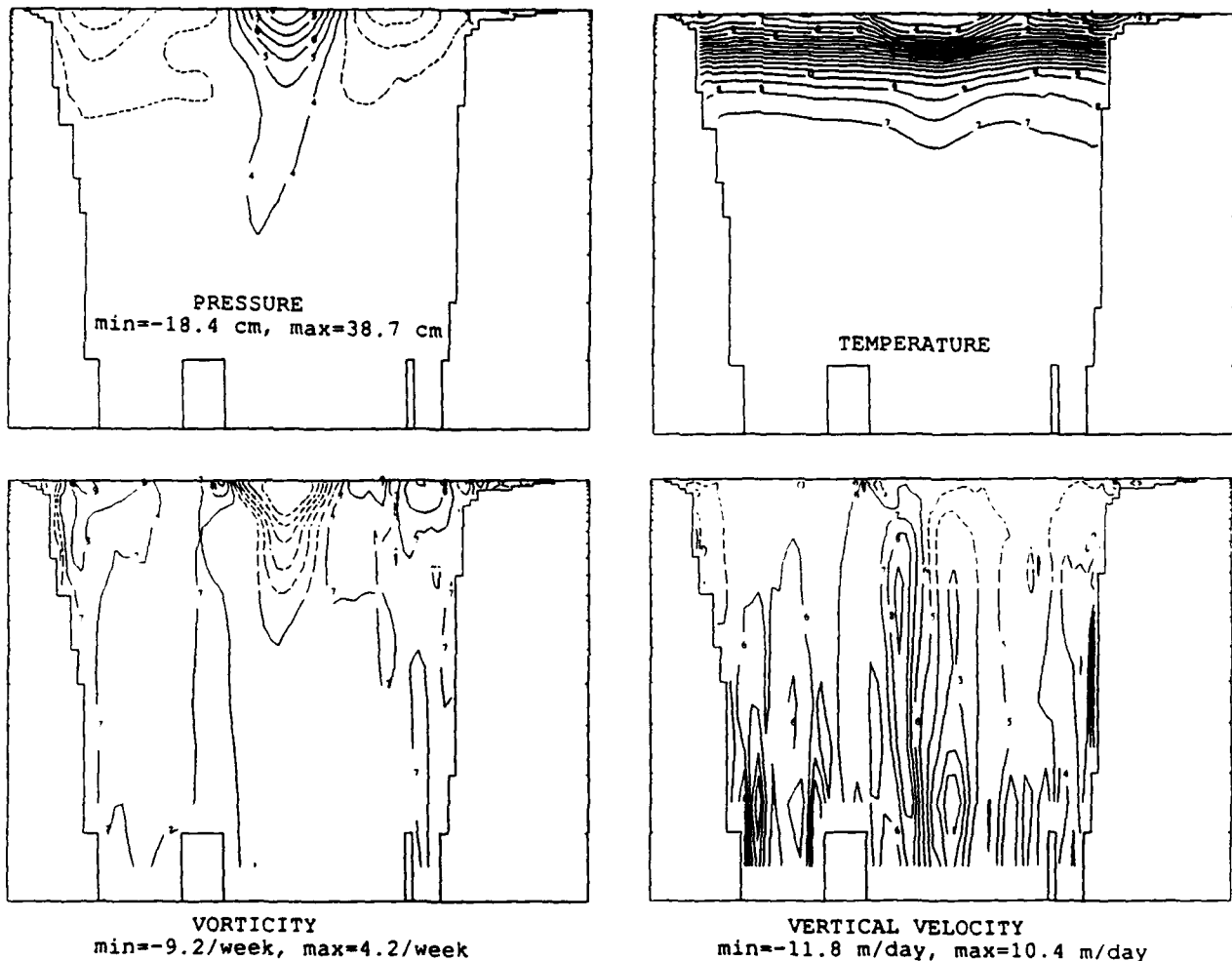


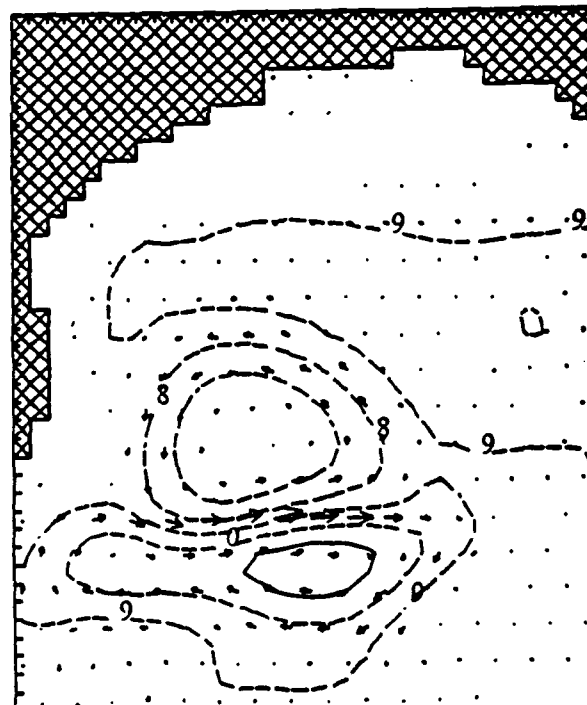
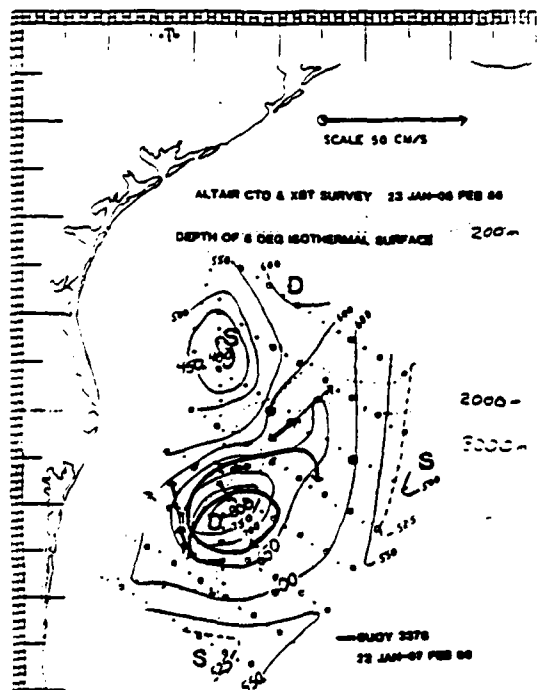
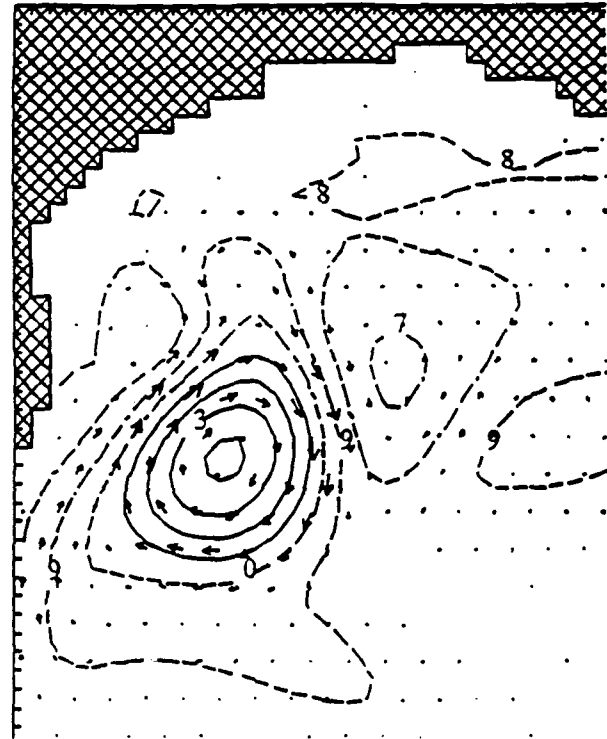
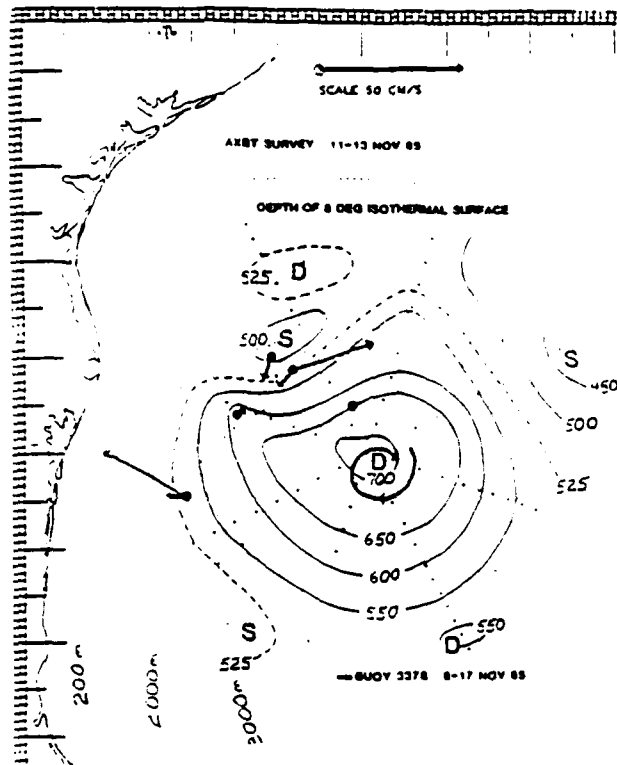
Figure 4c. Vertical cross-sections showing warm-core eddy structure at day 2025, and at the same locations as in Figure 4b.

Workstation. Such single processor runs SOMS at about 5 megaflops, compared to the  $O(500)$  megaflops now obtainable on supercomputers. The computing cost, with the resolution used, is about 20 hours per model year.

### 3.2 Comparison of the SOMS and DieCAST Models

Figure 6 compares SOMS and DieCAST results for Case B3. Neither model assimilates data and both use the same initial/boundary conditions, resolution, and physical parameters. Thus, the difference between the two is a measure of the truncation error difference between their grids. The first three major

Loop Current eddy shedding times agree within a few days (near days 570, 900 and 1210). Even secondary features are similar through the first three model years and nearly identical through the first eddy shedding cycle. The major eddy-scale advection time scale is  $O(10)$  days. Thus, the remarkable similarity even after  $O(1000)$  days supports the quality of both models, as well as the extensive data used in their validation. It also suggests that if the boundary and initial condition errors are known with errors smaller than the truncation errors of these runs, the GOM might be quite predictable through at least two eddy shedding cycles.



**OBSERVATIONS** (Brooks and Kelly, 1986)  
(Depth of 8°C isotherm)

**MODEL RESULTS**  
(Top layer pressure and velocity)

*Figure 5. Paired eddy formation near the western GOM shelfbreak; observations and model results with no data assimilation. The observations are 80 days apart, whereas the model results are 75 days apart (Days 1935 and 2010 from Case B3). The maximum velocity in the region shown in the results is about 50 cm/sec. The model results are from a seven-year simulation of the full GOM driven by realistic annual average Caribbean inflow.*



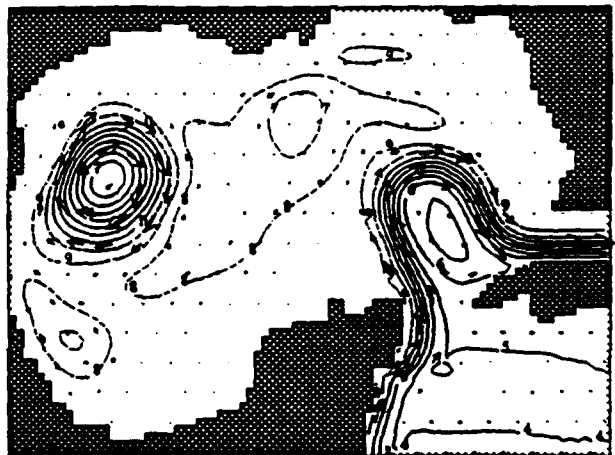
B3 / 1 P(cont. line, cm) and Vel(cm/sec) at day 360, depth= 10.0 m. PMS= 58.8, Vmax=103.0



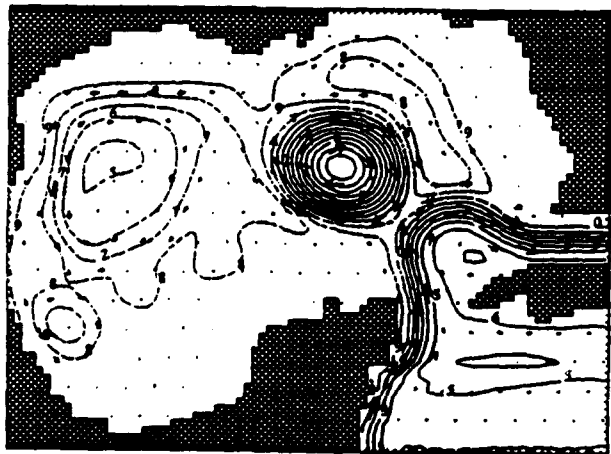
B3C / 379 P(cont. line, cm) and Vel(cm/sec) at day 360, depth= 10.0 m. PMS= 57.9, Vmax=105.1



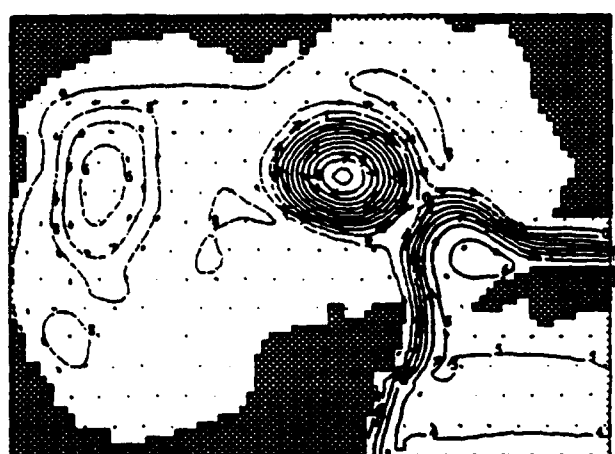
B3 / 1 P(cont. line, cm) and Vel(cm/sec) at day 720, depth= 10.0 m. PMS= 64.9, Vmax=99.8



B3C / 849 P(cont. line, cm) and Vel(cm/sec) at day 720, depth= 10.0 m. PMS= 57.2, Vmax=105.9



B3 / 160 P(cont. line, cm) and Vel(cm/sec) at day 900, depth= 10.0 m. PMS= 80.1, Vmax=112.8



B3C / 160 P(cont. line, cm) and Vel(cm/sec) at day 900, depth= 10.0 m. PMS= 73.2, Vmax=116.3

Arakawa "c" grid SOMS model

Arakawa "a" grid DieCAST model

Figure 6. Intercomparison of SOMS and DieCAST models in the Gulf of Mexico. Rigid-lid pressure (converted hydrostatically to free surface height anomaly) contours and velocity vectors are shown.

In Figure 6 DieCAST gives realistically larger maximum Loop Current velocities, while the total pressure range is slightly smaller than from SOMS. Apparently, DieCAST gives slightly more intense Loop Current fronts with the 20 km resolution used. Thus, fronts which contain a range of scales as in the Fourier series of a step function, appear slightly better represented by DieCAST. SOMS could also be improved by using analogous fourth order pressure gradient approximations, but the improvement would be limited by the accuracy of the Coriolis terms even with the fourth order interpolations used.

### 3.3 Further Discussion

In concluding this section, observations include an extensive base of time dependent aspects of GOM general circulation as well as detailed instantaneous snapshots. The close agreement of SOMS with these observations, even with steady inflow conditions and no transient data assimilation, shows that the natural time dependencies that develop spontaneously with SOMS are very similar to the observed ones. This supports the dynamic similarity of SOMS and GOM. Such similarity is critical to the reliable and useful application of ocean models.

The close agreement of  $O(1000)$  day simulations in GOM between the Arakawa "c" staggered grid SOMS and the Arakawa "a" semi-colocated grid DieCAST shows that the truncation error has secondary effect on major time dependencies for at least  $O(1000)$  days in both models. Thus, we have shown that two full primitive equation ocean models are dynamically similar to each other, as well as to the real GOM even though they use entirely different finite difference approximations because of their different grids.

DieCAST is simpler and requires less computation per time step than SOMS. It is also more stable with substantially longer time steps, because the closest data used in the pressure gradient approximation is two grid intervals apart, which reduces the frequency of the smallest scale resolved internal waves compared to SOMS. In the present GOM simulations, the combination of reduced computation, per time step and longer time step,

give about 30 percent net savings. (The time step increase depends on the ratio of the fastest flow velocity to the fastest internal wave speed.) Of course, the spatial accuracy of the smallest resolved scales is reduced compared to the Arakawa "c" grid approach even with the higher order approximations used. About 80 megaflop-hours calculation per model year are required with 20 km horizontal resolution and 20 layers ( $83 \times 60 \times 20$  grid) in the GOM simulations.

### 4. MODEL PARAMETER SENSITIVITY STUDIES USING GOM EDDIES

Dietrich et. al. (1990) and Dietrich (1992) studied the effects of lateral diffusivity and resolution on a prototype flat bottom closed rectangular ocean basin using SOMS. The results showed that 20 km resolution is adequate for typical eddies with scale  $O(100)$  km, and that lateral diffusivity greater than  $100 \text{ m}^2/\text{sec}$  leads to significant damping.

Dietrich and Lin (1993) showed that 20 km resolution is also adequate for modeling eddy shedding in an idealized GOM with flat bottom and ports patterned after the Florida and Yucatan Straits. They also showed, by analysis of the quasi-geostrophic omega equation for vertical velocity, that buoyancy can significantly affect vortex stretching. They also analyzed results with realistic GOM topography, using 16 levels vertical resolution and discuss the dissipation of GOM eddies. Although a stretched (log-linear) vertical coordinate was used, only two levels are used to resolve the top 200 meters, with nearly linear vertical resolution below 200 meters.

More recently, as shown in Section 5, higher vertical resolution can be employed to resolve dissipative GOM continental shelf processes. Twenty levels are used, with levels more concentrated near the top. The top level horizontal velocity, pressure, and density are 10 m from the surface. A vertical grid expansion factor of 1.19 is used to determine the 20 layer interfaces (21, 46, 75, 111, 153, 203, ..., 2920, 3500 m). Thus, six layers resolve the top 200 m, so the continental shelf is adequately resolved.

In Section 5, we will show that vorticity creation and secondary vertical circulations near shelfbreaks can strongly affect the interior GOM long-term general circulation. Notably, reducing lateral diffusivity, below the range normally used, can stop the Loop Current eddy shedding that dominates the GOM general circulation. This is caused by increased separation of cool positive vorticity water from the Yucatan shelf, which blocks the Loop Current (warm core negative vorticity) water northward penetration needed for eddy shedding.

Here, we explore the effects of lateral diffusivity and resolution on central and western GOM eddies in relatively short model simulations. A primary focus of these parameter sensitivity studies is their effects on cool core cyclonic eddies that form when old warm core anticyclonic Loop Current eddies approach the western GOM shelfbreak. Observations by Brooks and Kelly (1986) show an old warm core Loop Current eddy approaching the western GOM shelfbreak, leading to the formation of a paired cyclonic eddy over a period of about 80 days. This is followed by eastward movement of the old warm core eddy, and then, by its return to the shelfbreak region on a longer time scale. The Case B3 model results between days 1935 and 2010 are quite similar as shown in Figure 5.

In Sections 4.1 and 4.2, we examine the effects starting with the Case B3 results at day 1800 for initial conditions in all cases. Later (Section 5.3) we discuss B3 in great detail. In Section 4.3, we study resolution effects on an isolated eddy, in a closed rectangular basin, with latitude-independent western basin continental shelf patterned after the GOM.

#### **4.1 Lateral Diffusivity Effects on Paired Eddy Formation**

A common practice in modeling is to use the smallest eddy diffusivity consistent with numerical stability for a given resolution. This often reflects the fact that smaller diffusivities are more realistic. Sometimes, even scale selective filters are used to reduce unphysical damping of adequately resolved flow components.

With DieCAST, there is no need to use larger-than-realistic eddy diffusivity purely for numerical stability purposes. Indeed, using conventional ocean model diffusivities with our model eliminates certain observed features such as paired cyclonic eddy formation in the western GOM.

Thus, DieCAST's effective numerical diffusion and dispersion are of interest. The total numerical diffusion and dispersion includes numerical effects associated with averaging processes used in the control volume formulation, as well as the model's explicit diffusion and internal wave terms. All ocean models exhibit numerical diffusion and dispersion effects except in the limit of infinite resolution. Diffusion and dispersion effects can appear similar. For example, both decrease the intensity of fronts and associated currents.

Figure 7 series (a-e) show the effects of lateral diffusivity on model simulations initialized by Case B3 results at day 1800. The intermediate diffusivity results shown are from Case B3 in Section 5. This is one of the most extensively validated single runs in ocean modeling. Besides the paired cyclonic eddy formation, a large number of observations are in close agreement with the model results, (Dietrich and Lin, 1993), including spatial distribution of rms sea surface height time variance from satellite measurements; major Loop Current eddy shedding period; shed eddy size, phase speed, decay and dispersion rate, and vorticity; detailed Loop Current and shed eddy structure (penetration depth, cool pool near surface, and vertically coherent kink under separated Yucatan boundary current); small cool core eddy along Florida shelfbreak just before eddy shedding; small-scale eddies and waves along the Loop Current front; major Loop Current penetration along the Florida shelfbreak after eddy shedding; mean thermocline structure; and empirical orthogonal vertical structure functions including higher order modes.

To determine whether similar paired cyclonic eddies develop when larger values of lateral diffusivity are used, we did a similar calculation starting with the Case B3 results at day 1800 for initialization. The only difference from Case B3 is the increased lateral

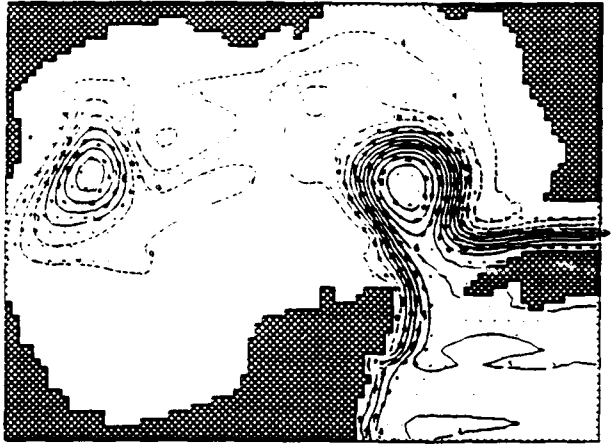
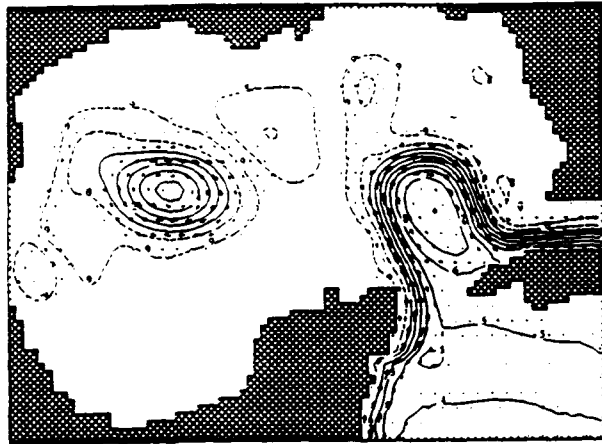
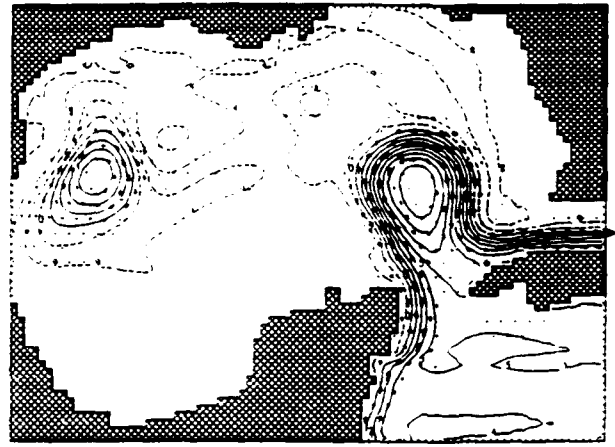
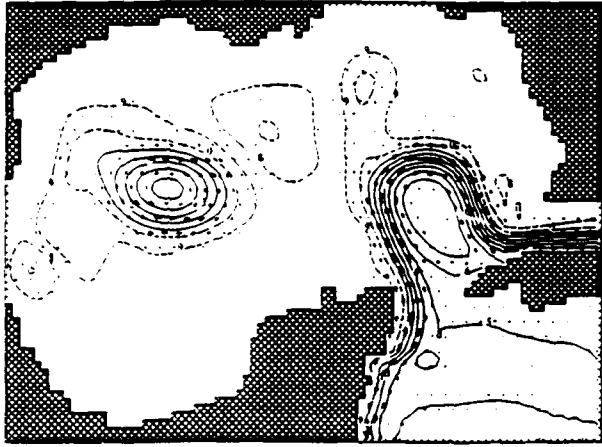


*Figure 7a. Day 60 Top Layer Pressure and Velocity.*

*Top Panel--lateral diffusivity = 2 m<sup>2</sup>/sec, maximum velocity = 104.9.*

*Center Panel--lateral diffusivity = 20 m<sup>2</sup>/sec, maximum velocity = 101.2.*

*Bottom Panel--lateral diffusivity = 200 m<sup>2</sup>/sec, maximum velocity = 79.4.*

*Figure 7b. Day 120 Top Layer Pressure and Velocity.*

*Top Panel--lateral diffusivity = 2 m<sup>2</sup>/sec, maximum velocity = 115.5.*

*Center Panel--lateral diffusivity = 20 m<sup>2</sup>/sec, maximum velocity = 112.8.*

*Bottom Panel--lateral diffusivity = 200 m<sup>2</sup>/sec, maximum velocity = 83.3.*

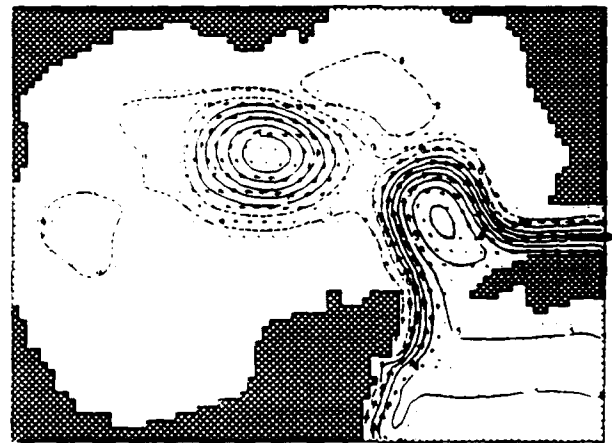
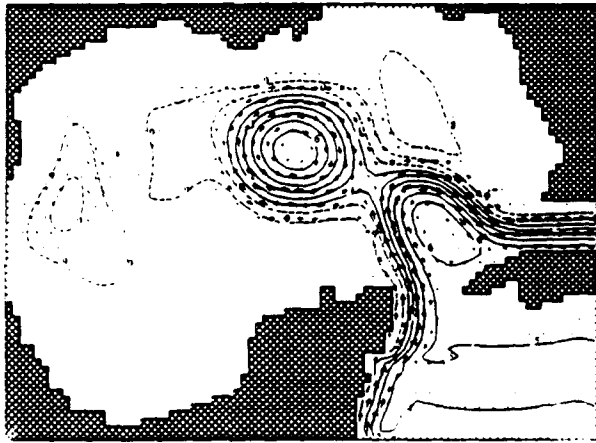
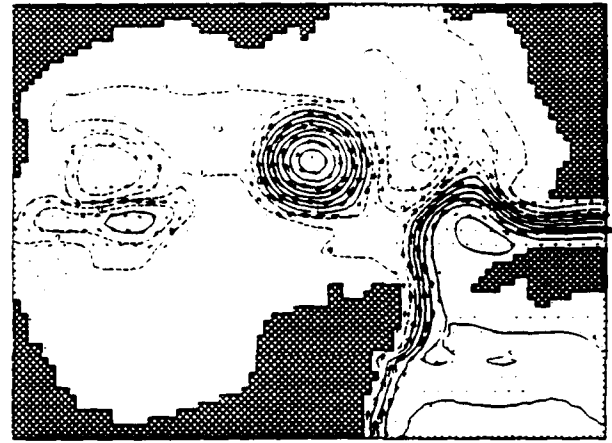
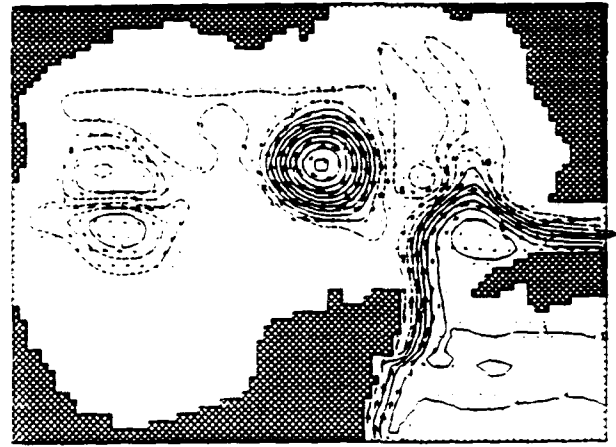


*Figure 7c. Day 180 Top Layer Pressure and Velocity.*

*Top Panel--lateral diffusivity = 2 m<sup>2</sup>/sec, maximum velocity = 112.5.*

*Center Panel--lateral diffusivity = 20 m<sup>2</sup>/sec, maximum velocity = 99.6.*

*Bottom Panel--lateral diffusivity = 200 m<sup>2</sup>/sec, maximum velocity = 81.4.*

*Figure 7d. Day 210 Top Layer Pressure and Velocity.*

*Top Panel--lateral diffusivity = 2 m<sup>2</sup>/sec, maximum velocity = 106.5.*

*Center Panel--lateral diffusivity = 20 m<sup>2</sup>/sec, maximum velocity = 91.9.*

*Bottom Panel--lateral diffusivity = 200 m<sup>2</sup>/sec, maximum velocity = 80.4.*

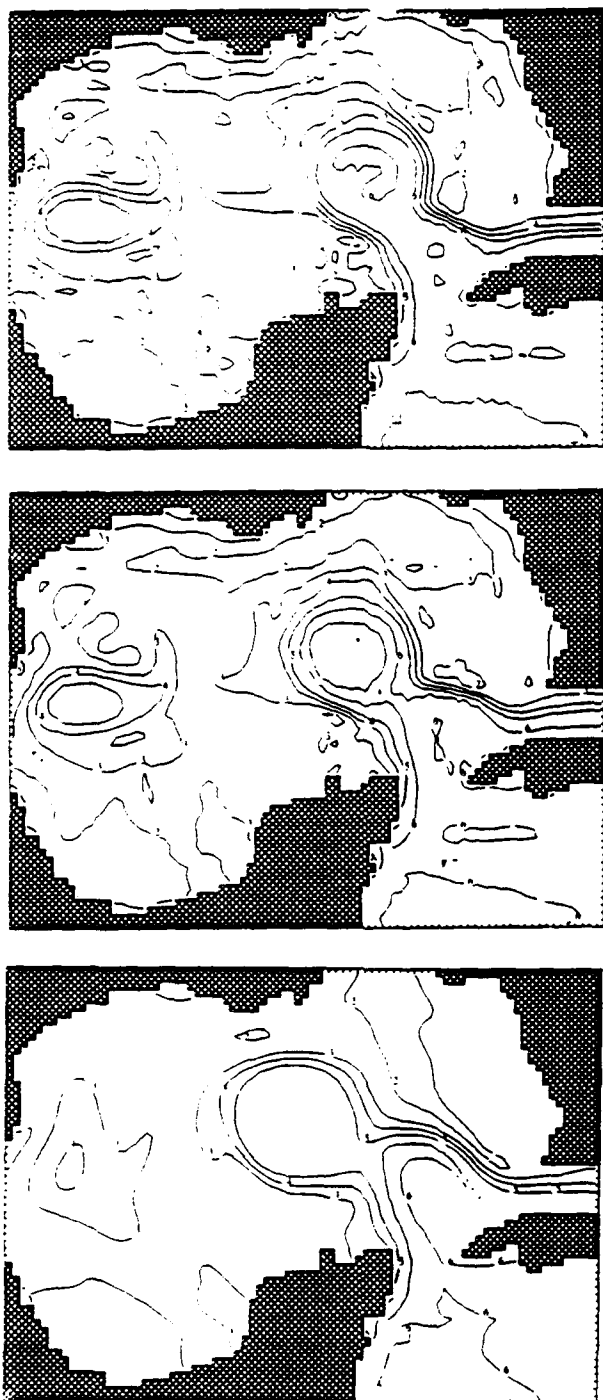


Figure 7e. Day 180 Top Layer Temperature.  
 Top Panel--lateral diffusivity =  $2 \text{ m}^2/\text{sec}$ .  
 Center Panel--lateral diffusivity =  $20 \text{ m}^2/\text{sec}$ .  
 Bottom Panel--lateral diffusivity =  $200 \text{ m}^2/\text{sec}$ .

diffusivity from  $20$  to  $200 \text{ m}^2/\text{sec}$  at day 1800, giving a Loop Current Reynolds number  $O(10^3)$ . We also ran an experiment with lateral diffusivity decreased to  $2 \text{ m}^2/\text{sec}$ , giving a Loop Current Reynolds number  $O(10^5)$ . The smallest diffusivities give a large cell Reynolds number  $O(10^4)$ , which is not numerically acceptable for most applications (Roache, 1976) because of possible contamination of large scale effects by nonlinear interaction with energetic small scale flow components. However, energy dissipation by bottom drag, dispersion by internal waves, numerical dispersion and dissipation effects, and the quasi-linear behavior of large-scale ocean flows tend to limit accumulations of energy in poorly resolved flow components.

The results of these experiments are summarized in Table 1, which shows the variation of maximum current speeds with specified lateral diffusivity. All cases use the same initial conditions (from Day 1800 of Case B3), thus the time is relative to Day 1800. The Table 1 data imply that the effective numerical diffusivity is less than  $O(100) \text{ m}^2/\text{sec}$ ; otherwise, less effect of decreasing the lateral diffusivity would occur. The Figure 7 results show that  $200 \text{ m}^2/\text{sec}$  diffusivity is too large to model the observed paired eddy formation and also leads to significant reduction of Loop Current front intensity in less than 15 days. Separation of cool, positive vorticity water from the shelf region, needed to get the observed paired eddies, does not occur with  $200 \text{ m}^2/\text{sec}$  diffusivity. Instead, the positive vorticity spreads along the shelfbreak as the warm core elongates. The smaller diffusivities also result in realistically larger maximum velocities and more concentrated fronts. These results show that such small diffusivity is needed to model the observed paired eddies.

Figures 7a-d show top layer P and V vectors for days 60, 120, 180, and 210. The maximum velocity is given in cm/sec for each panel. P is given in units of equivalent free surface height anomaly in centimeters.

All cases shown use equal momentum and thermal diffusivity. To emulate Lagrangian layered models, such as used by Hurlburt and

Table 1. Effects of Lateral Diffusivity on Maximum Velocity

Time/ Days	Lateral Diffusivity				
	2 m <sup>2</sup> /sec m/sec	20 m <sup>2</sup> /sec m/sec	50 m <sup>2</sup> /sec m/sec	100 m <sup>2</sup> /sec m/sec	200 m <sup>2</sup> /sec m/sec
15	95.7	94.6	92.9	90.3	85.5
30	94.6	93.5	91.9	88.6	81.2
45	102.7	99.2	94.4	86.6	80.3
60	104.9	101.2	94.7	87.6	79.4
75	95.9	94.2	90.2	88.7	82.0
90	109.0	102.0	96.2	93.2	83.0
120	115.5	112.8	102.6	97.3	83.3
150	113.9	112.4	105.3	94.4	79.3
180	112.5	99.6	89.4	85.8	81.4

Thompson (1980), one must use zero thermal diffusivity. To approximate this condition, we repeated the above experiment with 200 m<sup>2</sup>/sec momentum diffusivity and 20 m<sup>2</sup>/sec thermal diffusivity. This gives paired eddy formation similar to the lower diffusivity experiments shown in the Figure 7 series; however, both the old warm core eddy and the paired secondary eddies are less intense.

The difference between the lowest diffusivity used of 2 m<sup>2</sup>/sec and the intermediate 20 m<sup>2</sup>/sec case is much less than the 200 m<sup>2</sup>/sec case and the 20 m<sup>2</sup>/sec case. However, longer term results such as shown in Figure 8 indicate that the case with 2 m<sup>2</sup>/sec diffusivity compares best with the Brooks and Kelly (1986) observations. The paired cyclonic cool core eddy is slightly more intense. In both cases, the old warm core anticyclonic eddy is advected eastward by the cool core eddy. However, it returns to the shelfbreak region, similar to the observed eddy, but only in the lower diffusivity case. In the higher diffusivity case, it merges with an incoming new warm core eddy before returning to the shelfbreak region.

The small difference between the two lowest diffusivity calculations is not surprising, because the Reynolds number based on the eddy scales is very large in both cases, indicating very small diffusivity effects. However, results in Section 4.3 suggest that

increasing lateral resolution to 10 km might lead to more significant differences.

#### 4.2 Other Dissipative and Dispersive Effects

Our use of small lateral diffusivities raises the question of what is our effective lateral diffusivity? Or, what lateral diffusivity would affect front intensity and maximum velocity in a way similar to the combined effects of our lateral diffusivity and numerical effects? Effective values O(100) m<sup>2</sup>/sec or larger would be inconsistent with the Figure 7 series results. To address this, we performed experiments to assess numerical effects that could act like increased lateral diffusivities.

Our time filter weight parameter (FLTW) described by Roache and Dietrich (1988) could have a diffusivity-like effect in transient flows. We apply a weak time filter at the end of each time step by taking a weighted average of the leap frog intermediate value, and a time filtered value equal to the average of the forward and backward values. The result is used for the initial value for the next leap frog time step. This is similar to the Asselin (1972) filter and is analyzed by Roache and Dietrich (1988). Case B3 uses FLTW = 0.1 (90 percent leap frog plus 10 percent filtered), as do all other cases except the one shown in Figure 9. Figure 9 shows results using FLTW = 0.5. Comparisons with Case B3 results (Figure 7) shows that the time filter has little effect on the dominant time scales in these calculations.

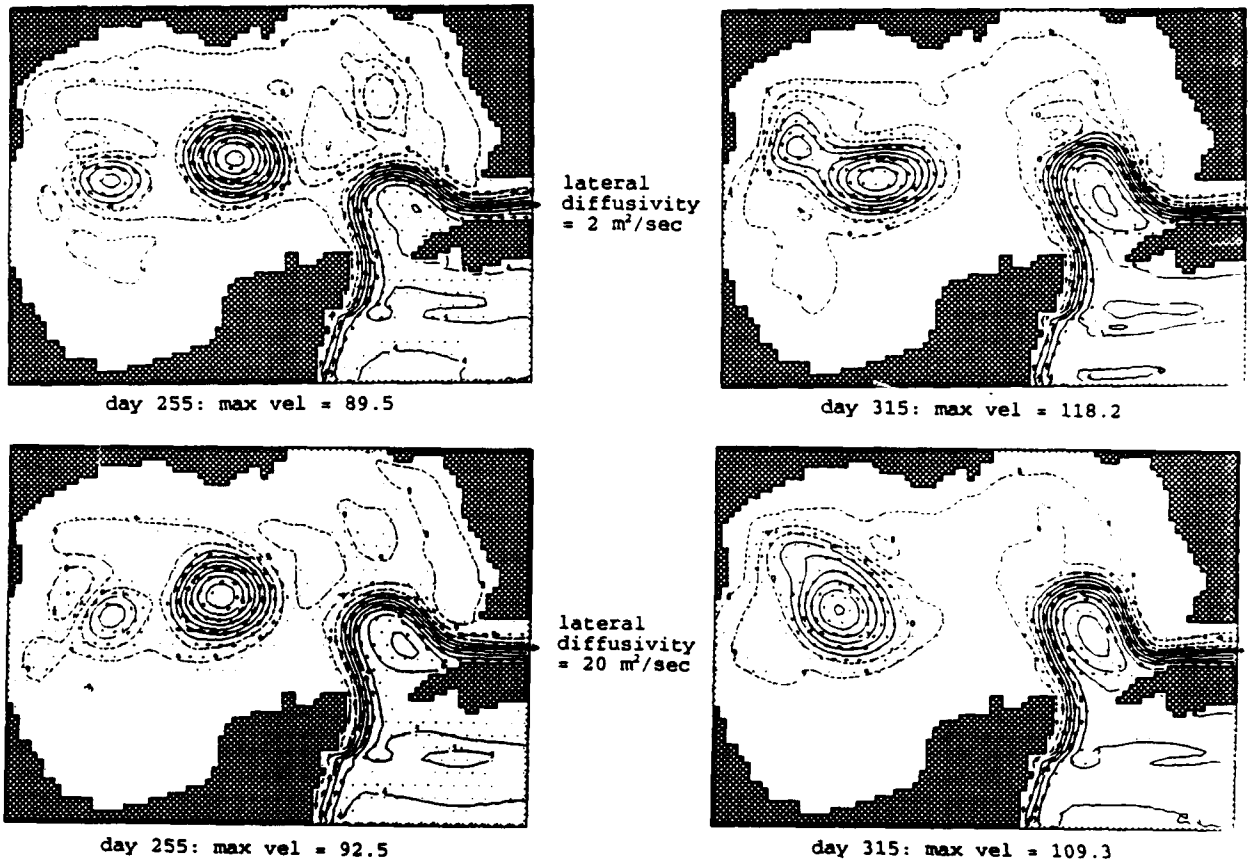


Figure 8. Longer term lateral diffusivity effects. Similar to Figures 7a-d except that days 255 and 315 are shown for the two lower diffusivity cases.

Our fully implicit backward treatment of the Coriolis and vertical diffusion terms could also have a diffusivity-like effect. Accordingly, we did an experiment with a non-damping trapezoidal (half implicit) treatment of the Coriolis terms. Figure 10 comparisons with Figure 7 show that the time damping associated with the backward differencing used in Case B3 has very little effect.

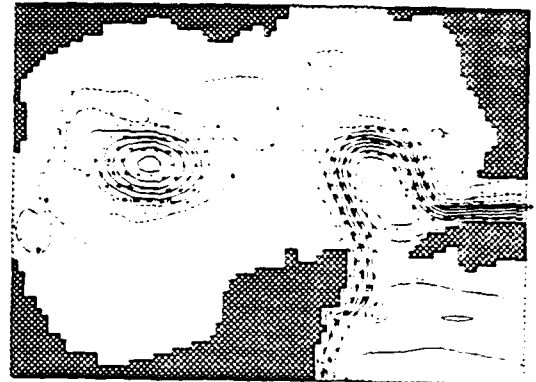
Probably the largest numerical diffusivity-like effect results from the interpolations used in evaluating the Coriolis terms. This effect increases with decreasing time step. Thus, we performed an experiment with a time step of 18 instead of 36 minutes, as shown in Figure 11. Comparisons with Figure 7 shows noticeable effects, but these are less than the effects of increasing lateral diffusivity to more

conventional values ( $O(100)m^2/sec$  or larger). This implies interpolations used for the Coriolis terms have little effect, especially with the 36 minute time step used. Dietrich (1993) shows that dispersion errors in the popular energy conserving Arakawa scheme used by "c" grid modelers are much larger than the errors in the present scheme. However, it is also clear that the present scheme would benefit by using a larger time step, which requires implicit internal wave treatment not in the present model.

In summary, the most realistic physical behavior occurs when smaller than  $O(100) m^2/sec$  lateral diffusivity is used by DieCAST, which has relatively small additional numerical dissipation.



Day 60



Day 120



Day 180



Figure 9. Effects of FLTW Time Filter Parameter. Like intermediate diffusivity Case B3 in Figures 7a-c except the time filter parameter is 0.5.

Figure 10. Effects of fully implicit (backward) Coriolis treatment. Like Case B3 in Figures 7a-c except non-damping trapezoidal (half implicit) treatment is used for the Coriolis terms instead of fully implicit treatment.

Day	<u>MAX VELOCITY (cm/sec)</u>	
	<u>Present Case</u>	<u>Case B3</u>
60	101.1	101.2
120	112.8	112.8
180	99.7	99.6

Day	<u>MAX VELOCITY (cm/sec)</u>	
	<u>Present Case</u>	<u>Case B3</u>
60	104.1	101.2
120	103.5	112.8
180	91.3	99.6

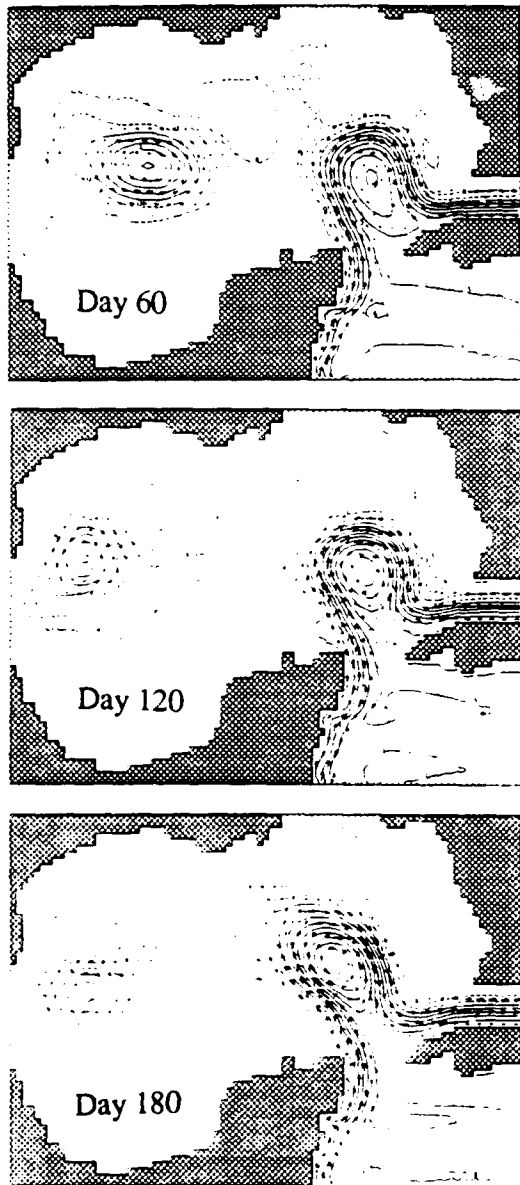


Figure 11. Effects of interpolations in evaluating Coriolis terms. Like diffusivity Case B3 in Figures 7a-c except the time step is reduced to 18 minutes instead of 36 minutes.

<u>MAX VELOCITY (cm/sec)</u>		
<u>Day</u>	<u>Present Case</u>	<u>Case B3</u>
60	96.6	101.2
120	97.5	112.8
180	105.1	99.6

### 4.3 Resolution Effects

To reduce the calculations required, we use a smaller rectangular basin to address resolution sensitivity. The basin modeled is 860 km wide, corresponding roughly to the western GOM. Its latitudinal extent is 1200 km, slightly larger than the western GOM. An idealized latitude-independent western continental shelf is specified. Its structure is indicated in longitudinal cross-section plots discussed below. The depth is 3500 m everywhere else.

Instead of specifying a drag coefficient to parameterize bottom boundary layer effects, we use a non-slip condition and vertical diffusivities which are largest at the bottom and decay away from it. A bottom value of 100 cm<sup>2</sup>/sec and a vertical decay scale of 100 m are prescribed. This allows the calculations to resolve a continental shelf Ekman layer without having significant deep water effects. The flow is entirely determined by initial conditions, since the basin is closed and there are no wind stress/thermohaline effects.

The initial temperature distribution is determined from the first eddy shed by the Loop Current of the Case B3 simulation soon after shedding (day 600). A window of data containing the eddy is first transplanted to the eastern part of the rectangular 860 by 1200 km basin. The transplanted data is then extended outside the window in the new 860 by 1200 km rectangular basin.

The initial temperature extension is done as follows. A two-dimensional Laplace equation is solved for temperature at each level. Temperature at the window boundary provides Dirichlet inner boundary conditions for the extended region. In deeper layers, the window becomes irregular as it fills with bottom topography. Insulated conditions are specified on the rectangular outer large-basin boundary. (Even reasonable Dirichlet conditions, such as specified constant temperature equal to the mean on the window boundary, can result in substantial breakup of the eddy as it propagates westward in the larger domain.)

Figure 12 shows the resulting initial top level temperature, while Figure 13 shows the initial temperature in a longitudinal/vertical cross-section near the center of the eddy.

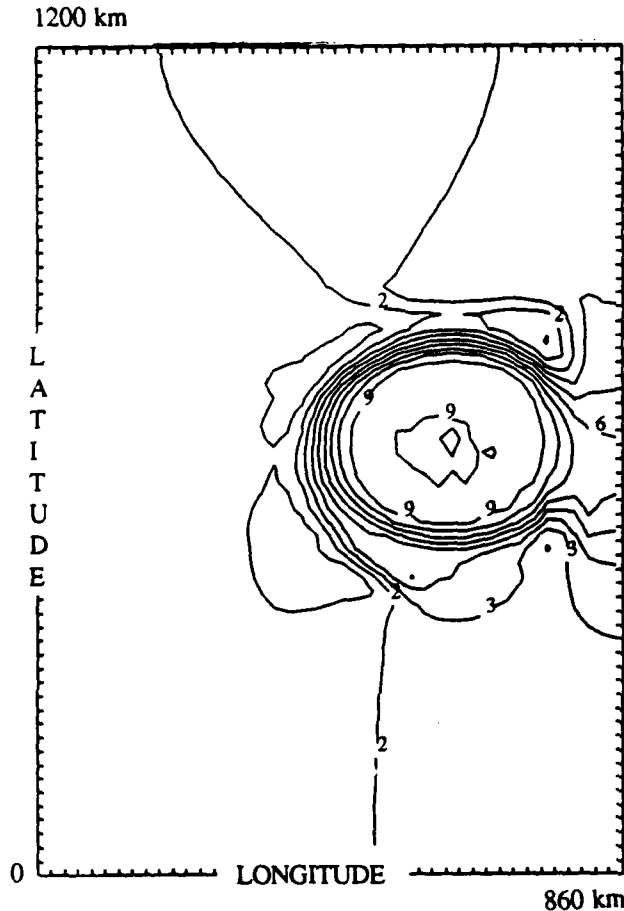


Figure 12. Initial Top Level Temperature. Contours show the horizontal structure of the transplanted GOM eddy used to initialize the resolution sensitivity study. Boundary tick marks show the lower resolution grid line locations. This is 20 km resolution with a 43 x 60 grid. The higher resolution case uses 10 km resolution with an 86 x 120 grid.

The initial velocity conditions are also transplanted from the GOM window to the rectangular basin. Outside the window, the initial velocity is zero, but it quickly adjusts to the relatively weak pressure gradients outside. The resulting eddy remains coherent and propagates in a manner similar to the Case B3 calculations.

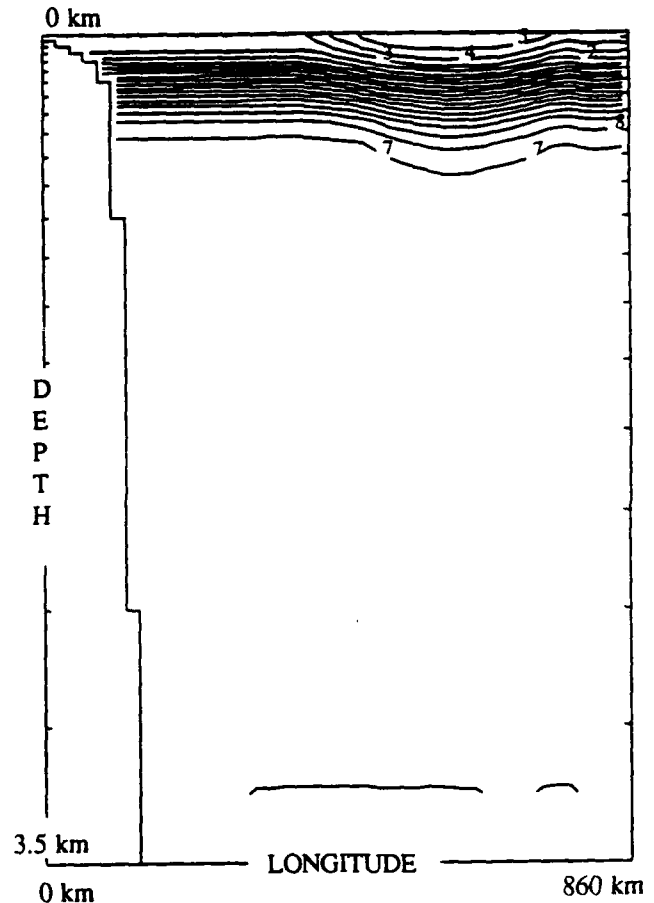


Figure 13. Initial Longitudinal Temperature Cross-Section Near Eddy Center. Vertical structure of transplanted GOM eddy used in initialized resolution sensitivity study. Boundary tick marks show the expanding vertical grid used in the lower resolution case. This is 20 levels with top layer being 20.9 m thick. The double resolution case is 40 levels with top layer being 10.0 m thick and the second layer being 10.9 m thick; every second level exactly matches the corresponding level of the lower case.

We found that transplanting only the top 1000 m of the shed eddy into a 1000 m deep basin results in separation of substantial parts of the eddy, even though the deep water flow is weak. This indicates that deep water vortex stretching is an important part of the eddy dynamics, which is a result of reduced deep water stratification as discussed later. We have also found that the long term eddy dynamics near the shelfbreak are significantly affected by the reduced longitudinal extent of the basin, because circulation of the vorticity

around the basin occurs more rapidly. However, the goal here is not to mimic actual GOM conditions, but simply to explore resolution effects.

The Figure 14 series (a. Days 30, 60, 90, 120, 150, 180, 210, and 240/ b. Days 90 and 180) show the evolution of the initial warm core anticyclonic eddy as it propagates westward and interacts with the western shelfbreak, resulting in the generation of paired cool core cyclonic eddies. The results are shown for 20 km resolution with 20 levels and 10 km resolution with 40 levels. These results show that higher resolution results in: a more intense eddy front and other small-scale nonlinear features (especially evident in Figure 14b); increased maximum velocity, especially during nonlinear interaction and dissipation in the shelfbreak region; stronger intensification of the original warm core eddy near the shelfbreak; and a longer lasting warm core eddy. However, the deep water eddy propagation speed is affected very little.

The Figure 15 series shows vertical cross-sections from both 20 km and 10 km resolutions. The day 30 panels of Figure 14 show the locations of these cross-sections. With 10 km resolution, small-scale secondary vertical circulation results in the intensification of the warm core eddy front (see Figure 15a). This is reflected by the increased velocities shown in Figure 14 (Day 60).

Small-scale effects are more evident in vertical velocity than in other fields, because it is related nonlinearly to the density field, while horizontal velocity and pressure are related linearly according to quasi-geostrophic dynamics. Even density appears less dominated by small-scale features; this is probably because the horizontal velocity tends to be nearly parallel to temperature contours thus decreasing the magnitude of the nonlinear terms needed to produce smaller scale features. This nonlinearity results in the vertical velocity field showing larger resolution effects than the other fields. Nevertheless, the larger scale vertical velocity components that are dominated by the linear beta term in the quasi-geostrophic omega equation are less affected. In deep water, this term produces downwelling (solid contours) ahead of the

warm core eddy and upwelling (dashed contours) behind the warm core eddy.

As the eddy pushes onto the shelf, the downwelling ahead of the warm core eddy is at least partly compensated by upwelling associated with the sloping Ekman layer near the shelfbreak. Smaller scales develop and the flow becomes more nonlinear. The difference between the 20 km and 10 km resolution results increases more rapidly. Notably, the 10 km case shows a much more intense and longer lasting warm core eddy during its nonlinear evolution and dissipation near the shelfbreak. The separated paired eddies propagate around the old warm core eddy to the southwestern region of the basin until the old warm core eddy energy has been sapped. They then merge near the southwestern corner of the basin to produce a strong cool core cyclonic circulation. Rossby wave effects tend to oppose eastward advection of the separated vorticity away from the corner.

In both resolutions, there is a stronger tendency for separated positive continental shelf vorticity and upwelled cool water to be advected around the dissipating warm core eddy than in Case B3. This reflects a more energetic warm core eddy and perhaps also the latitude independence of the shelfbreak. (The Case B3 eddy is transplanted closer to the western continental shelf in the present calculations, leaving less time for its energy to disperse and dissipate before reaching the shelfbreak than in Case B3).

These results show that 10 km or better resolution is desirable for accurate description of eddy interactions with shelfbreaks, and also for accurate front descriptions in deep water. The front description is especially important when modeling multiple interacting deep water eddies.

In concluding this section, it has been shown that more realistic modeling of GOM eddies and their interaction with continental shelf flows occurs when using less than 100 m<sup>2</sup>/sec lateral diffusivity. We also have shown that although 20 km resolution appears adequate for deep water modeling, better than 20 km resolution is desirable for the shelf region.

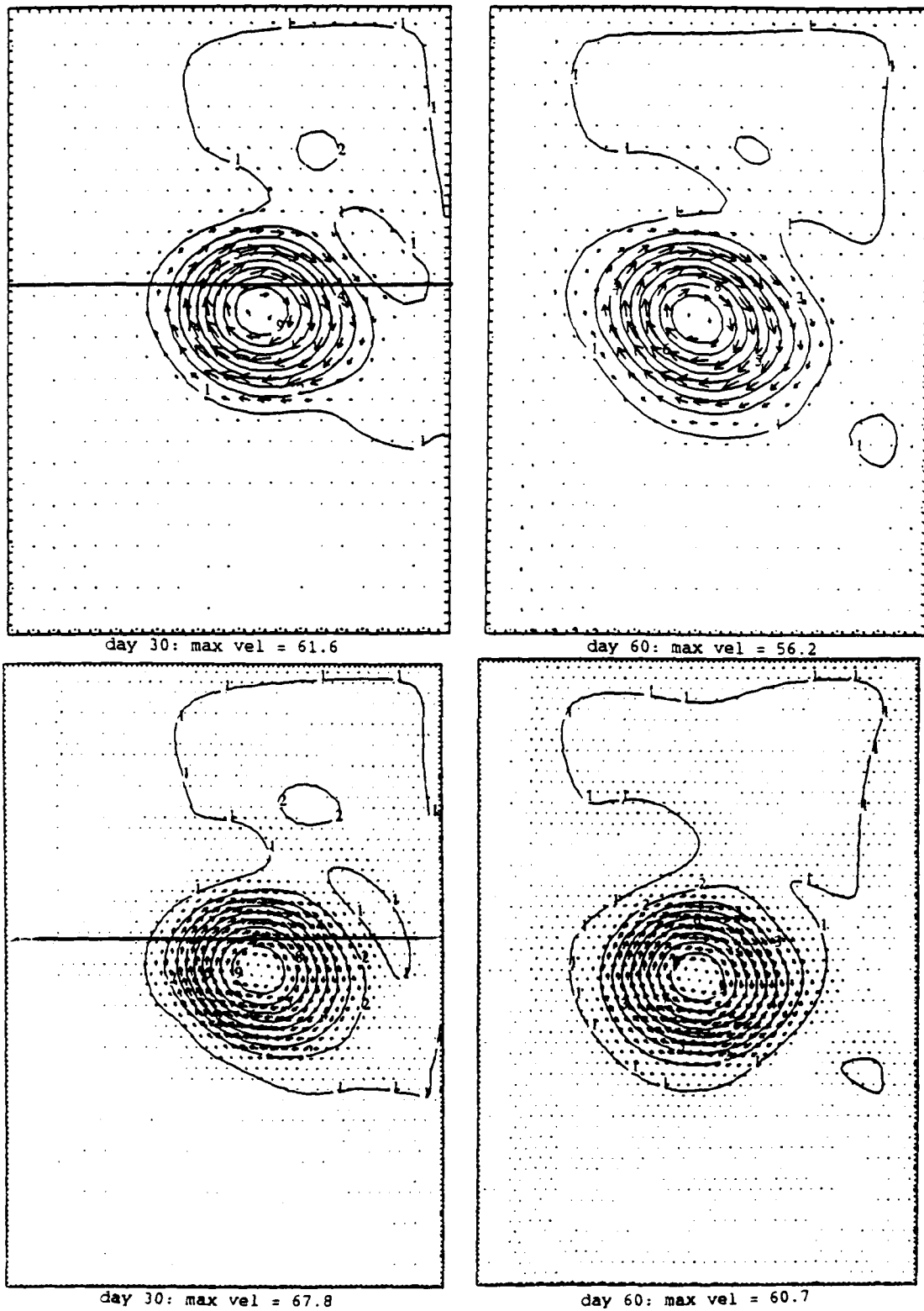
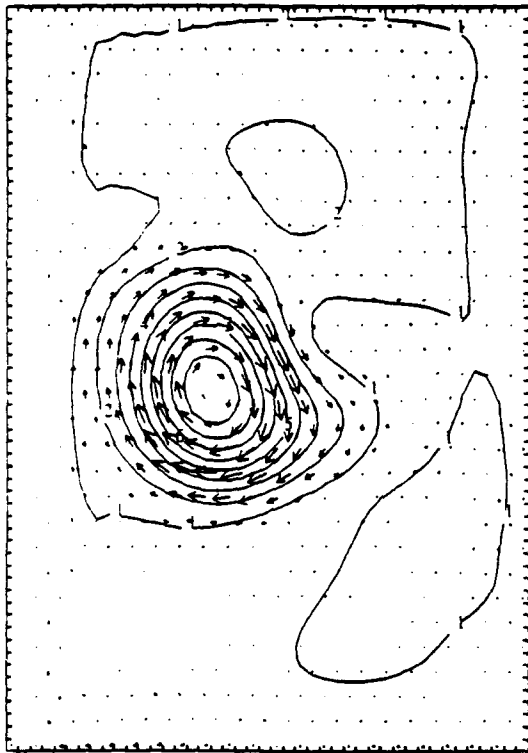
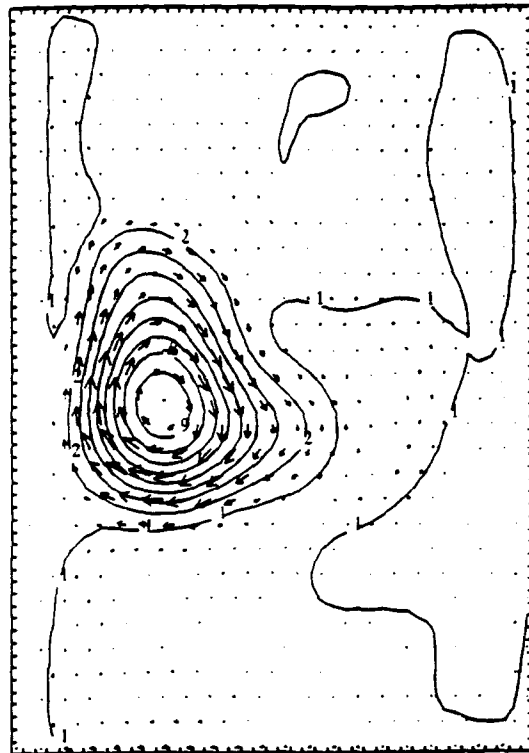


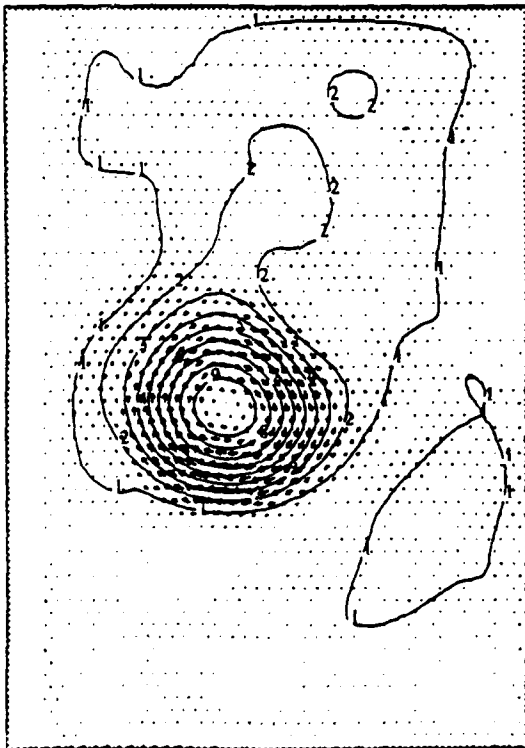
Figure 14a. Top Level Results (P and V) for Days 30 and 60. The upper panels are results with 20 km resolution and 20 levels. The lower panels are results with 10 km resolution and 40 levels. Contour increments are 1/10 the difference between the maximum and minimum values of pressure or temperature. Maximum velocities are given in cm/sec.



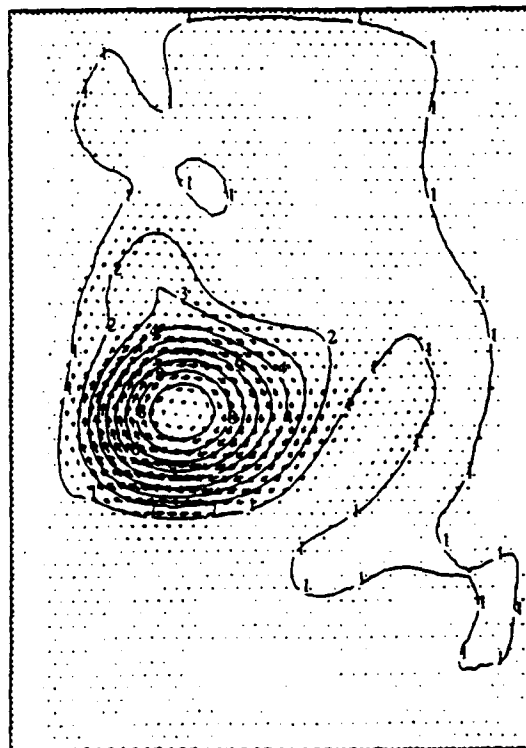
day 90: max vel = 52.2



day 120: max vel = 52.8

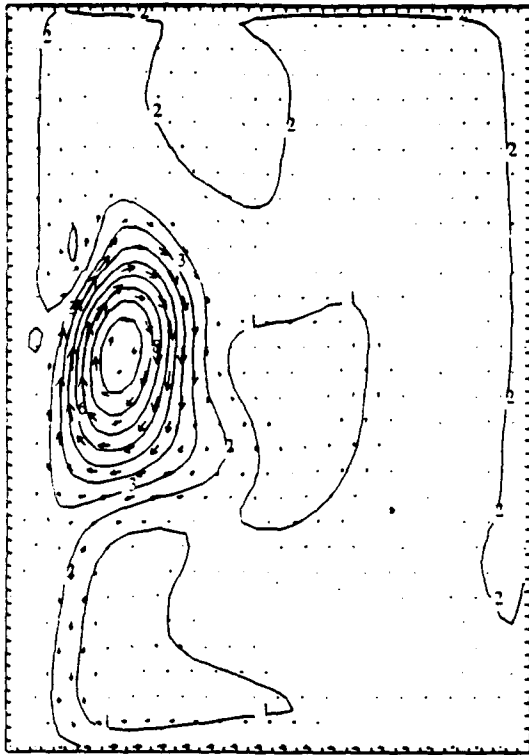


day 90: max vel = 65.3

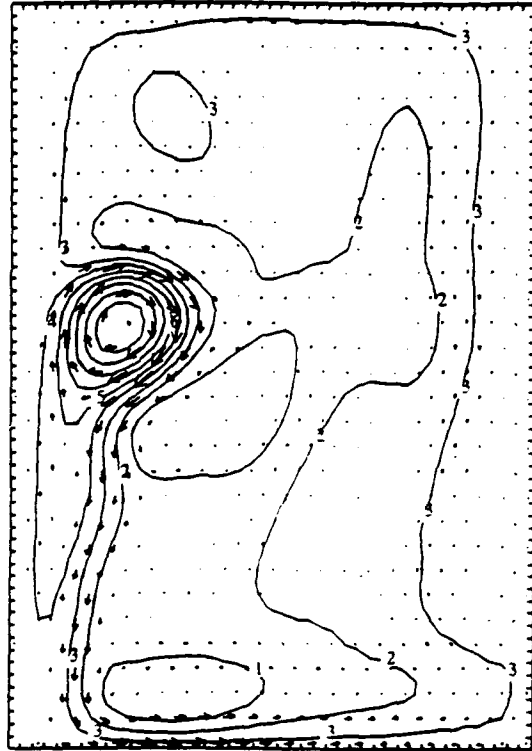


day 120: max vel = 60.6

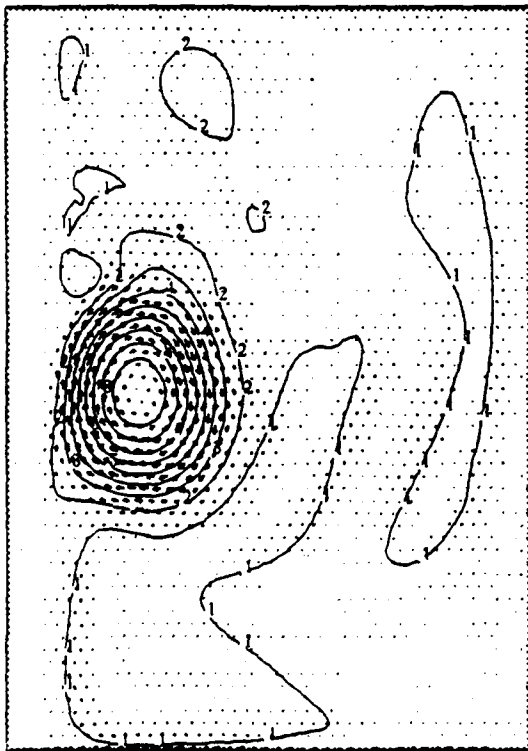
Figure 14a (Continued). Top Level Results (P and V) for Days 90 to 120.



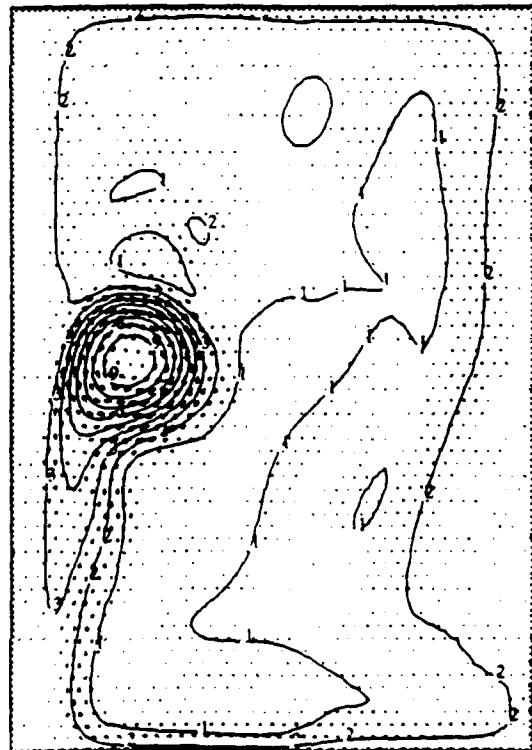
day 150: max vel = 65.7



day 180: max vel = 56.5

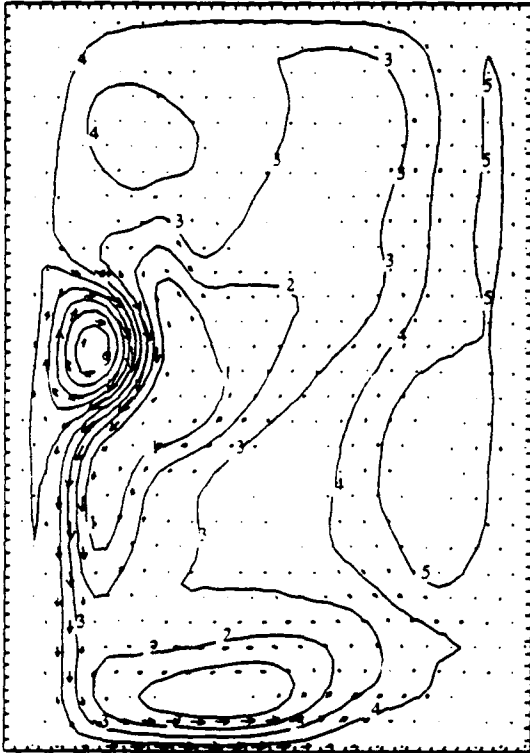


day 150: max vel = 70.9

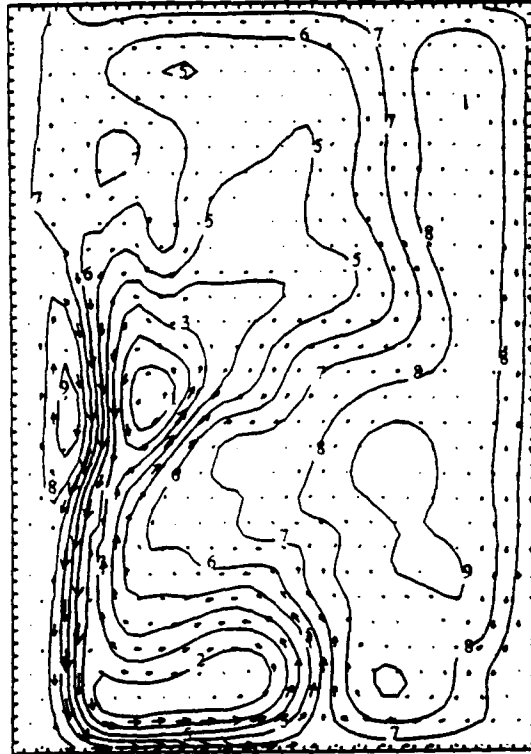


day 180: max vel = 82.6

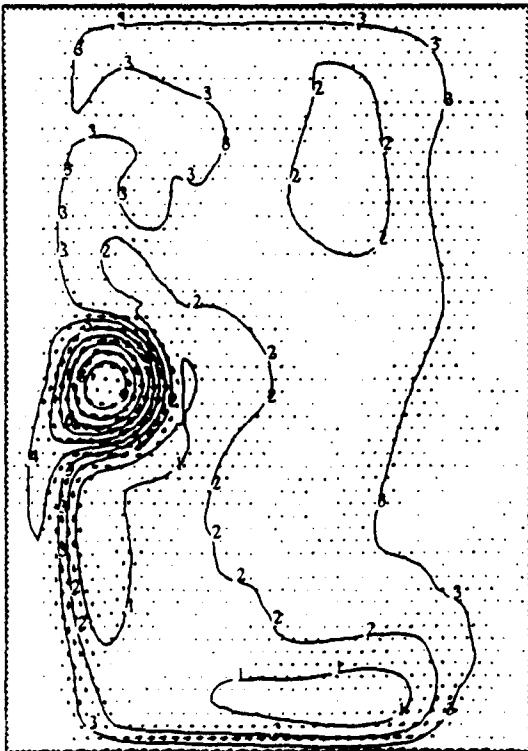
Figure 14a (Continued). Top Level Results for (P and V) for Days 150 and 180.



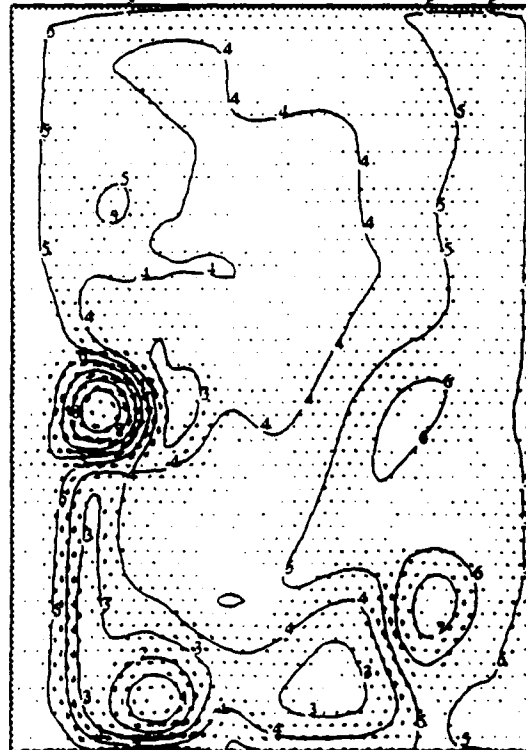
day 210: max vel = 47.9



day 240: max vel = 31.8

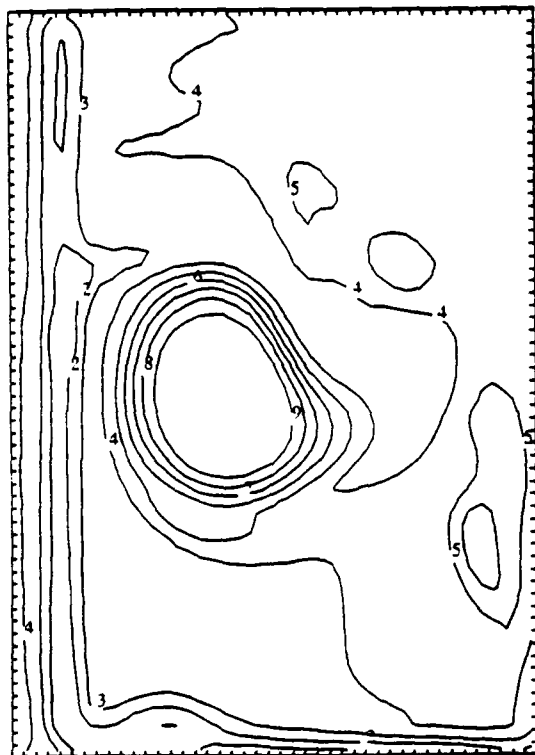


day 210: max vel = 78.2

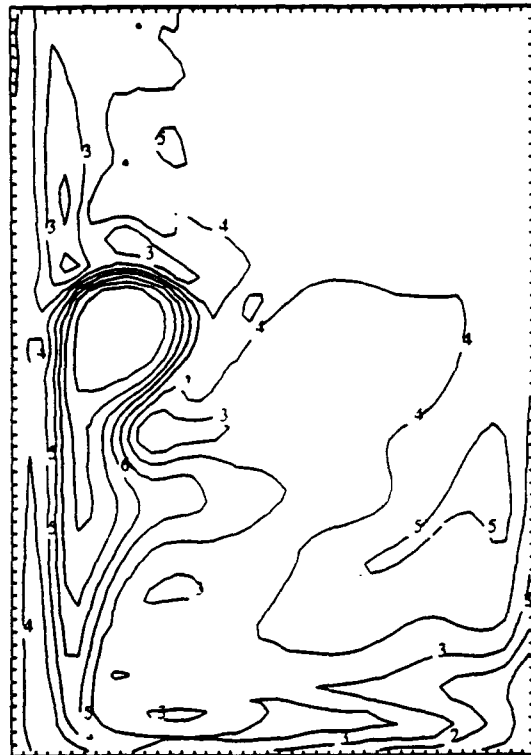


day 240: max vel = 56.5

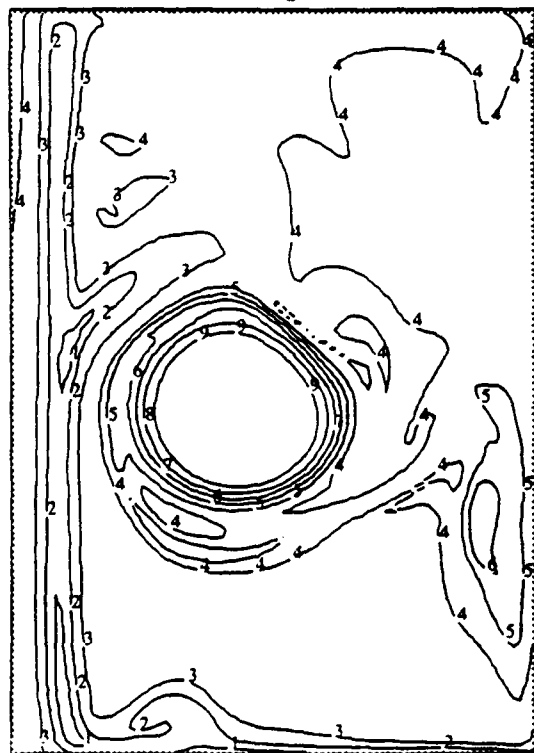
Figure 14a (Continued). Top Level Results for (P and V) for Days 210 and 240.



day 90



day 180



day 90



day 180

Figure 14b. Top Level Results (T) at Days 90 and 180.

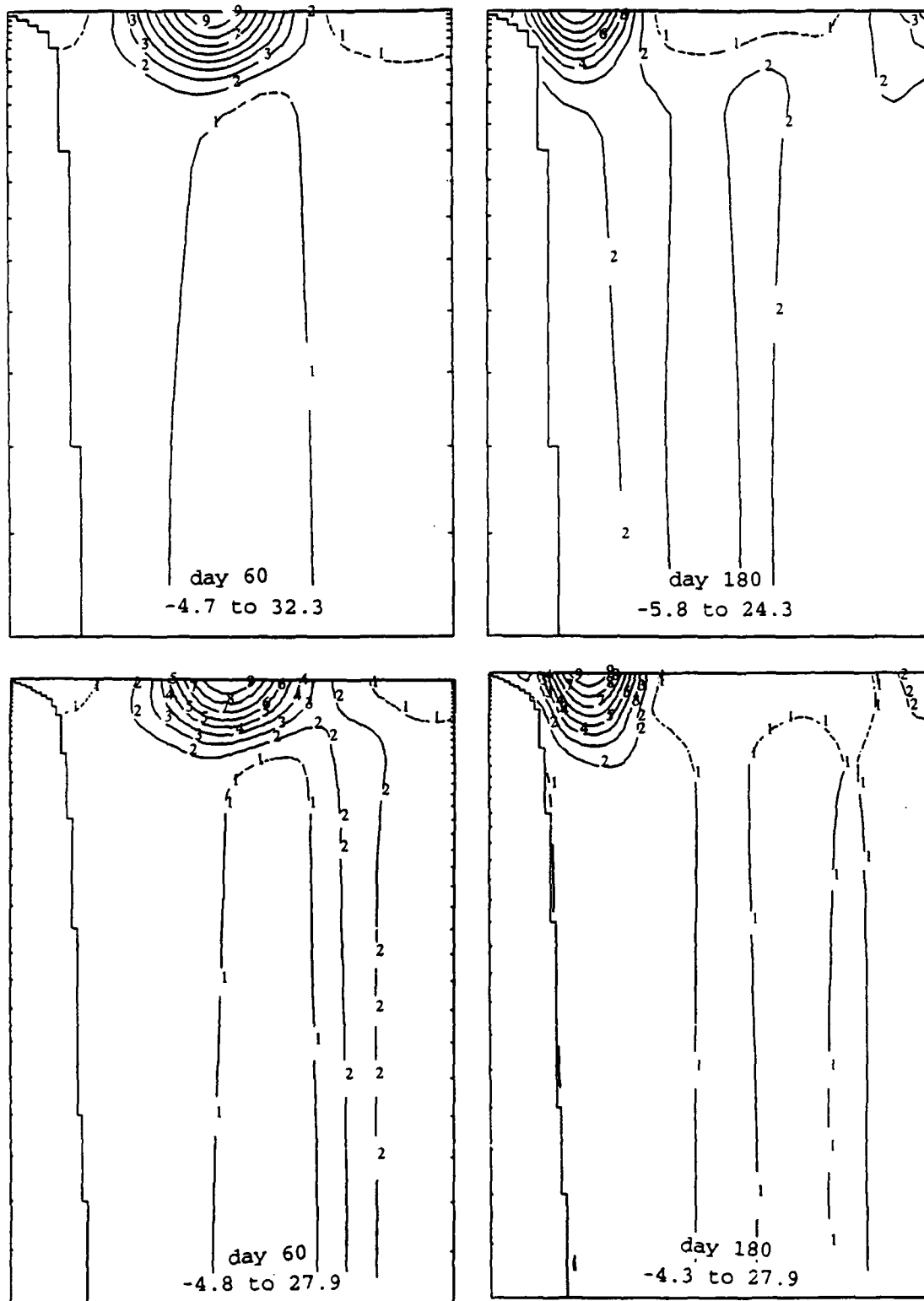


Figure 15a. Longitudinal cross-sections of results from resolution sensitivity study (for pressure). The upper panels are results with 20 km resolution and 20 levels. The lower panels are results with 10 km resolution and 40 levels. The left panels are at day 60; the right panels are at day 180. The locations of these cross-sections are indicated in the Day 30 panels of Figure 14. Pressures ranges are given in equivalent free-surface-height anomalies in cm.

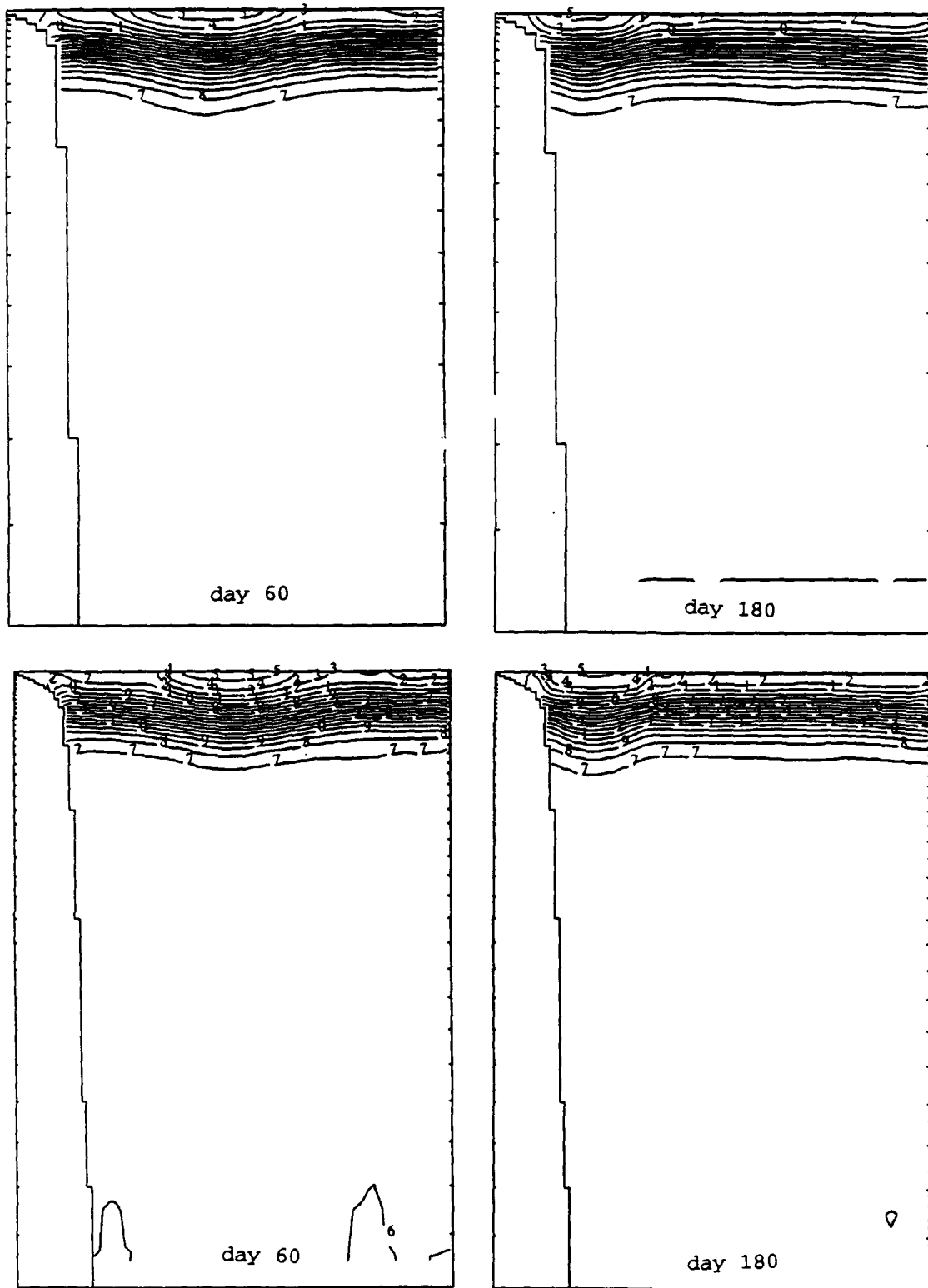


Figure 15b. Longitudinal cross-sections of results from resolution sensitivity studies (for temperature).

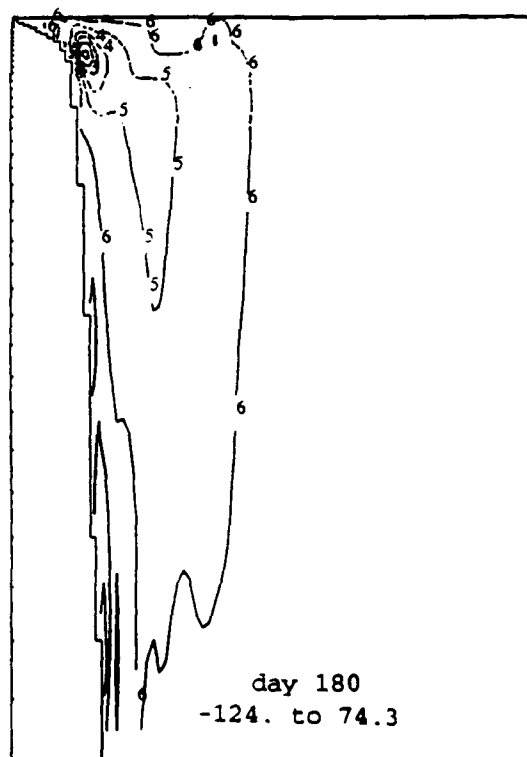
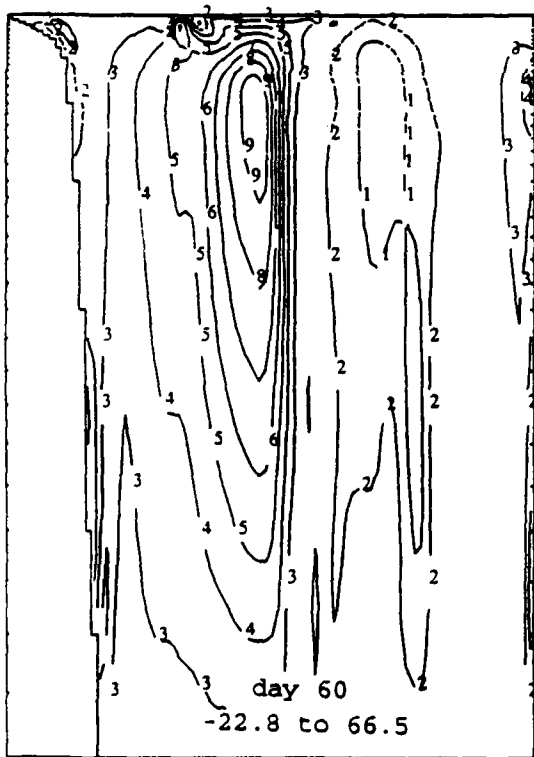
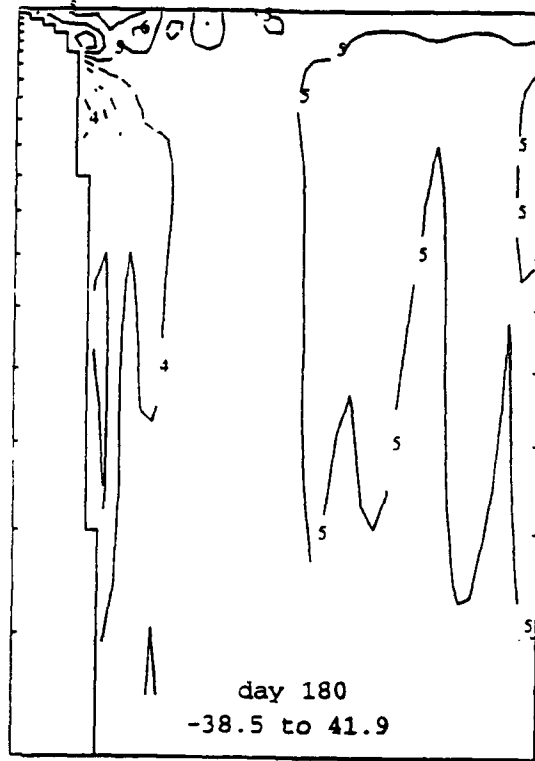
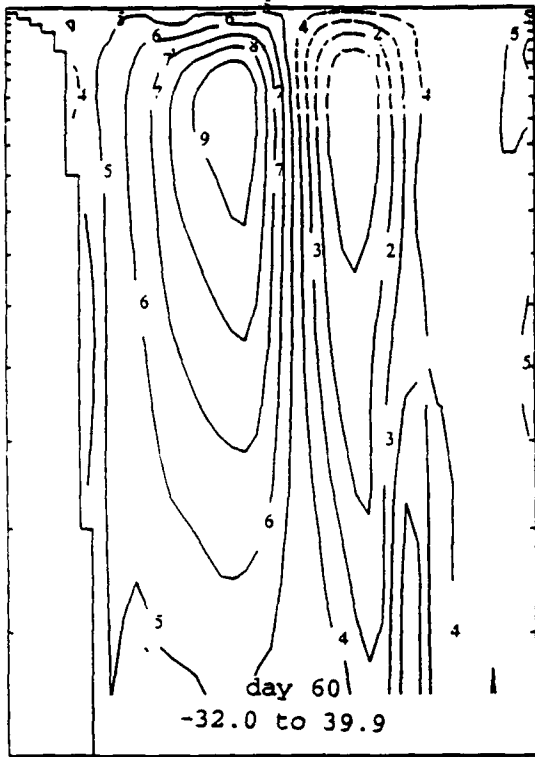


Figure 15c. Longitudinal cross-sections of results from resolution sensitivity study (for vertical velocity). Negative contours are dashed (but only in upper part of plot). The maximum and minimum are given in microns/sec (multiply by 0.6 to get meters/week).

The idealized shelf problem is good for high resolution studies of shelfbreak interactions. The longitudinal coordinate could be stretched to get better resolution near the shelfbreak, where it is needed most. This problem can also be used to assess potential benefits of a domain decomposition approach in which a lateral-boundary-fit coastal regime model is fully coupled to a deep water model.

## 5. NUMERICAL STUDIES OF THE GOM GENERAL CIRCULATION AND COMPARISONS WITH OBSERVATIONS

The Gulf of Mexico is an appropriate place to study many phenomena and to evaluate ocean models because: it is small enough to be readily modeled, and yet has main physical parameters (Rossby number, Rossby radius of deformation, large Reynolds number for major eddies) similar to most ocean regions; its general circulation is simpler and better known than most ocean regions; and its boundary conditions, which are critical in modeling physical systems, are simple and quite accurately known. Although certain aspects have been analyzed, the phenomena involving the interaction between deep water and shelf regions are not understood in detail.

Cooper and Thompson (1989, a-b) analyzed the response of coupled shelf and deep water regions to a hurricane by modeling a basin with a longitudinally independent continental shelf and deep water patterned after the northern GOM. Gawarkiewicz and Chapman (1991) applied a simplified linear three-dimensional free-surface model to address generic shelf flows. Their flows were forced by along-shelf inflows at the upstream direction relative to the propagation of coastal trapped waves. They note that buoyancy effects not addressed by their simplified study might be significant. Their results show that bottom boundary layer flows can lead to a shelfbreak front of passive scalars independent of buoyancy effects. Smith and O'Brien (1983) explored nonlinear deep water topographic effects on isolated quasi-geostrophic eddies. Topography-induced vortex stretching is well represented by their 2-layer model formulation. Their lower layer eddies do not

encounter bottom stress until reaching the sloping bottom. (Although lateral gradients associated with the slope are involved, they are similar in effect to bottom stress.) Their eddies have smaller scale and larger Rossby number than typical old warm core eddies in the western GOM. Also, bottom drag-like effects are not well resolved vertically, because the topography is totally contained in the bottom layer for numerical reasons.

The detailed interaction of deep water features with continental shelf processes has received less attention. Major water flow features can move into shallow water, as on western continental shelves, because of Rossby wave effects. Rossby wave dynamics are analyzed in detail by McWilliams and Flierl, 1979. When this happens, the bottom stress can greatly increase, because in deep water the energy is usually concentrated in the top 1000 m, with bottom flows being relatively small. Secondary bottom boundary layer flows can reduce the bottom pressure gradient and thus make the deep water drag even smaller (Peggion, 1984).

Dietrich and Lin (1993) applied the present model to the GOM and northwestern Caribbean. Lateral resolution and parameter (mainly stratification) sensitivity tests were done in an idealized flat bottom basin with ports patterned after the GOM. With two levels (Eulerian z-level vertical representation), the results were quite similar to those from two-layer (Lagrangian) simulations in the GOM work by Hurlburt and Thompson (1980, 1982). Dietrich and Lin (1993) showed that 20 km resolution is adequate for addressing the main features of Loop Current penetration and eddy shedding, whose scales are  $O(300)$  km. They also included a higher 16-level vertical resolution run using real GOM topography. The results compare well with many observed GOM features and indicate that dissipation of old Loop Current eddies involves higher order baroclinic modes.

Vertical stratification effects were also analyzed according to quasi-geostrophic vertical motion omega equation and vortex dynamics. Stratification effects were shown to be significant for scales smaller than the Rossby radius of deformation. Thus, for the smaller

scales of interest in GOM dynamics, especially those involving continental shelfbreak effects that are of interest here, conservation of absolute potential vorticity ignores significant buoyancy effects as well as bottom drag.

In this research, we resolve shallow continental shelf regions in the GOM by increasing the vertical resolution so that six layers are included on the continental shelf. We do not resolve the shelf bottom boundary layer, but realistic bottom drag is used to parameterize the main effects.

Our model setup is described in Section 5.1. In Section 5.2, we address lateral diffusivity effects in cases using our early "best guess" of Caribbean inflow conditions. In Section 5.3, we slightly modify the Caribbean inflow to reflect larger inflows from the Windward Passage reported by Schmitz and Richardson (1991) and further address sensitivity to lateral diffusivities. We include a run with a constant 25 Sverdrups total Caribbean inflow instead of the 29 Sverdrup value based on the Schmitz and Richardson data. We thought this was our best case even before finding that 25 Sverdrups is a better estimate for the annual mean (Hamilton, 1992). This best case is described in detail. Section 5.4 analyzes results described in Sections 5.2 and 5.3. Section 5.5 addresses truncation error effects. This includes runs designed to address the effects of the staircase boundary approximations

### 5.1. Model Formulation

The phenomena are controlled by the Yucatan Strait inflow and associated Loop Current and separated eddies. These can lead to significant shelf flows and dominate the cross-shelfbreak flow, especially in the western GOM. Except for occasional intense events such as hurricanes, local wind forcing leads to very little cross-shelfbreak flow. Outside of thin boundary layers, the wind-forced shelf flow tends to follow constant  $f/H$  contours, where  $f$  is the local Coriolis parameter and  $H$  is the local depth. Thus, although local wind forcing is important in very shallow water, it leads to little total

volume flow across the shelfbreak. Even in shallow regions, the wind-independent circulation component is of interest. We ignore local wind forcing in this early shelf-resolving study. We also ignore local thermohaline forcing and annual inflow cycles into the Caribbean.

Here we use a modified version of the original SOMS model. To save computation, the modified version does not include the Mellor-Yamada level 2.5 turbulence closure scheme (Mellor and Yamada, 1982) or the SOMS thin shell bottom boundary layer submodel. The modeled region includes the northwestern Caribbean, with time independent inflows specified at the eastern and southern boundaries of the modeled Caribbean region. The southern boundary inflow is a barotropic western boundary current. The eastern inflow, independent of latitude, is related to the inflow density distribution by the thermal wind relation based on geostrophic and hydrostatic assumptions, and is mostly trapped above a realistic sloping thermocline.

Temperature and salinity are dynamically coupled to the flow only through their effects on density through the equation of state. With equal heat and salinity diffusivities and a linear equation of state, the salinity effects can be parameterized in the temperature initial and boundary conditions (see Appendix II).

The lateral resolution is 20 km. The main difference from Dietrich and Lin (1993) is in the much higher vertical resolution in the upper levels. Using 20 layers instead of 16, and an expanding vertical grid with expansion factor of 1.19, the top six layer interface depths are: 21, 46, 76, 111, 153, and 203 m. The deepest interface, at the bottom of layer 20, is at 3500 m depth, where deeper GOM water is truncated. This should not significantly affect the GOM general circulation, because there is very little deeper water and its velocity is very small.

Initial conditions are zero velocity and horizontally constant density with vertical variations patterned from observations. The

inflows are switched on full at the first time step. Because of the rigid-lid approximation, this initial kick gives a non-geostrophic flow everywhere. However, the flow quickly becomes quasi-geostrophic.

Vertical heat and momentum diffusivities are  $1 \text{ cm}^2/\text{sec}$  plus an additive variable numerical contribution that decreases with increasing resolution. The numerical contribution is chosen such that the local vertical cell Reynolds number matches the user specified value, where we use 10. The resulting maximum vertical diffusivities are less than  $10 \text{ cm}^2/\text{sec}$  in the simulations reported, and are much smaller away from shelf regions. Lateral heat and momentum diffusivities are constant in all runs. Lateral diffusivities and other main parameters varied in the runs described in Table 2. Lateral boundary conditions are free-slip and insulated.

In all cases, we use insulated bottom conditions and a drag coefficient of  $D = 0.002$ . The magnitude of the drag acceleration is  $D \cdot u^2/DZ$ , where  $u$  is the bottom layer velocity magnitude and  $DZ$  is the bottom layer thickness. Its direction is opposite to the bottom layer velocity. We use lateral diffusivities from 2 to  $200 \text{ m}^2/\text{sec}$ , in the range of physically plausible parameterizations of subgrid-scale eddies. Cases B1, B1A, and B2 shed only one eddy during the first 1800 days, so

are not considered in a regular shedding regime. All eddy phase speeds are 4.0 to  $4.5 \text{ cm}/\text{sec}$ . Cases B0 and B0A are run with a straight (latitude-independent) western Caribbean continental shelf.

## 5.2 Effects of Lateral Diffusivity on Eddy Shedding

Case A1 is based on our early "best guess" of Caribbean inflow conditions. It produces regular eddy shedding after an initial delay. The delay appears related to a cool core cyclonic eddy on the north side of the Loop Current that slows its early northward penetration. The results show that this positive vorticity eddy forms as a result of the separation of cool positive vorticity water from the Yucatan continental shelf. Suspecting that such separation depends on Reynolds number we ran Case A1B that is identical to Case A1 except for its reduced lateral diffusivity.

### 5.2.1 Low Diffusivity: Case A1

The first case uses  $20 \text{ m}^2/\text{sec}$  lateral diffusivity. The result is regular eddy shedding. Six major warm core eddies are shed during the calculation. After the first eddy shedding at day 590, five more eddies are shed during the next 1380 days, giving an average eddy shedding period of 276 days as shown by Figure 16.

Table 2. Summary of Model Parameters

Case	Lateral Diffusivity $\text{m}^2/\text{sec}$	Caribbean Inflows Sverdrups		Eddy Shedding Period Days
		Total	Eastern	
A1	20	27.5	4.43	276
A1B	2	27.5	4.43	no shedding
B0	2	29.0	7.27	no shedding
B0A	200	29.0	7.27	180
B1	20	29.0	7.27	800 (1 only)
B1A	40	29.0	7.27	600 (1 only)
B1B	100	29.0	7.27	225
B2	20	27.5	7.27	600 (1 only)
B3	20	25.0	7.27	254
B3B	100	25.0	7.27	240

The 276-day eddy shedding period is close to the 37-week average period observed (Sturges and Welsh, 1991). Figure 16 also shows that the phase speed of the shed eddies is about 4 cm/sec. This is close to values from observations, theory, and previous GOM simulations (Vukovich and Crissman, 1986).

The first eddy shedding is delayed by the early development of a cold core cyclonic eddy on the north side of the Loop Current (Figure 17), which temporarily slows the Loop Current penetration needed for major warm-core eddy shedding. Figure 18 shows the time average top layer pressure for the six year simulation.

### 5.2.2 Ultra-Low Diffusivity: Case A1B

This development of a cold-core cyclonic eddy on the north side of the Loop Current involves the separation of cool positive vorticity Caribbean western boundary current from the continental shelf. This separation generally depends on the Reynolds number.

To examine the Reynolds number effects on this cool positive vorticity boundary current separation, a second run, Case A1B (Table 2), was done with lateral diffusivity reduced to 2 m<sup>2</sup>/sec. We justify using this unconventionally small value in Section 5.2.3.

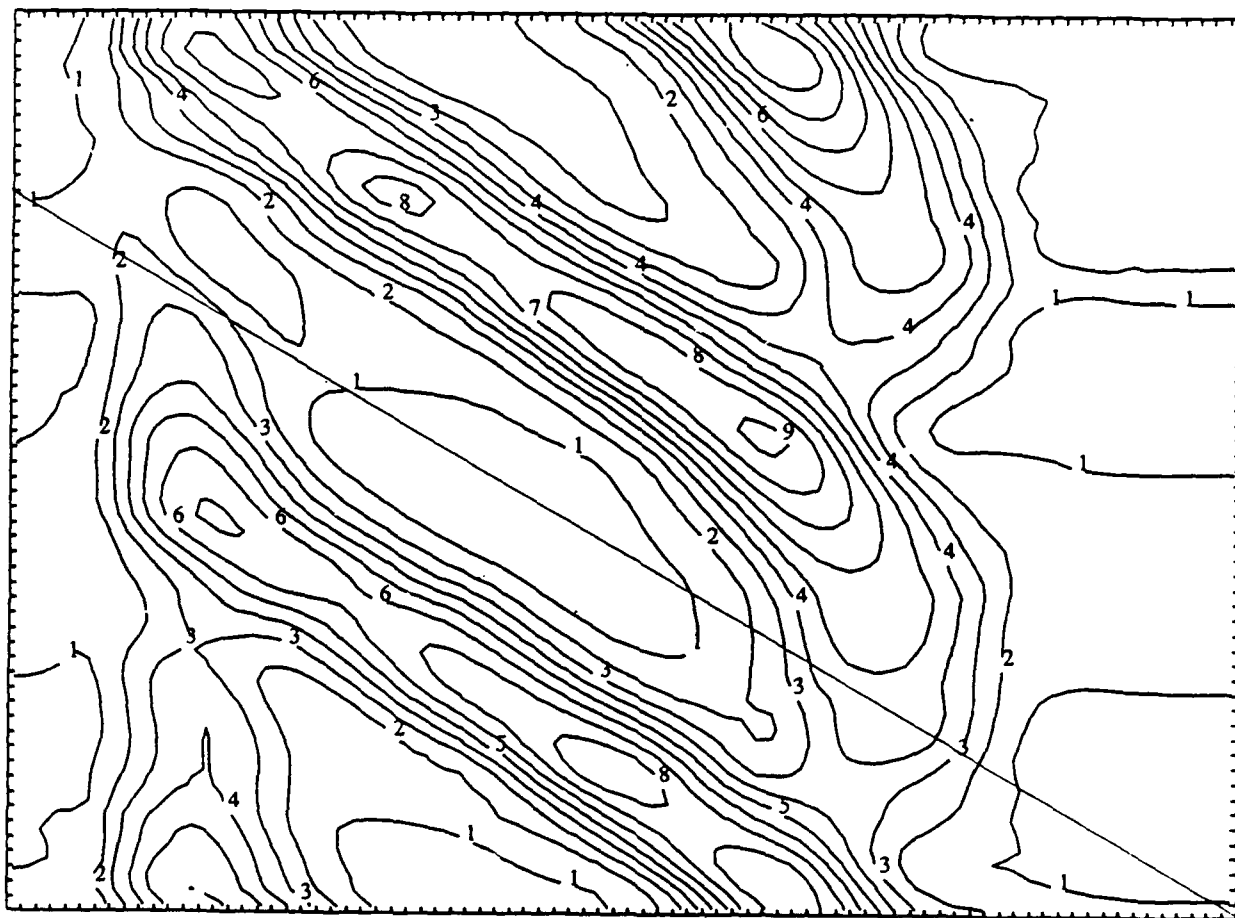
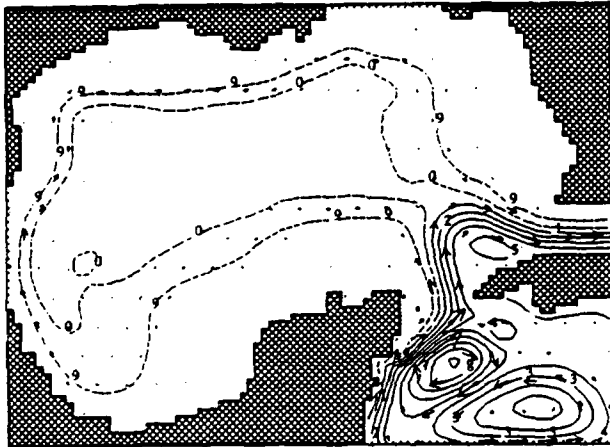
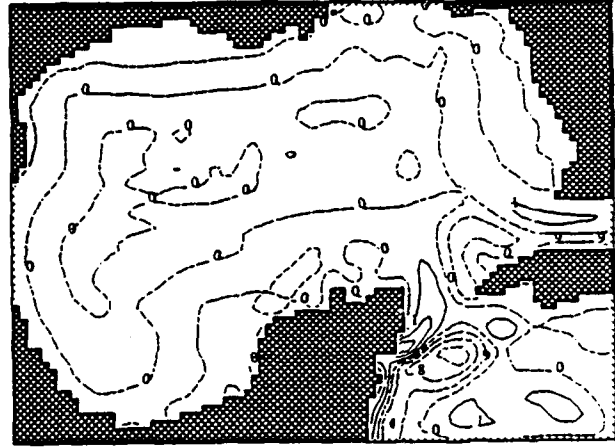


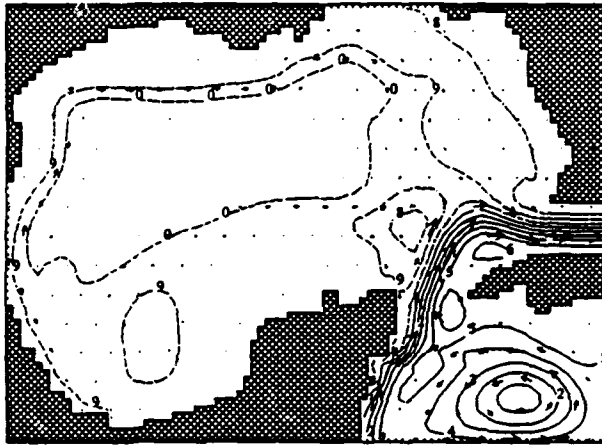
Figure 16. Longitude/Time Section of Equivalent Free Surface Height Anomaly ( $P$ ) for the Eddy Shedding Case A1. The free surface height is calculated hydrostatically from DieCAST top layer pressure (at depth 10 m). The period shown covers days 840 to 1440. The longitudinal dimension is 1660 km. The diagonal line corresponds to a phase velocity of 4 cm/sec. The pressure is averaged over the band of latitudes. Tick marks on the ordinate axis indicate the 10-day spacing of the data saved. Tick marks on the abscissa correspond to the model resolution (20 km). Ten contours are uniformly distributed.  $P_{max} - P_{min} = 41$  cm.



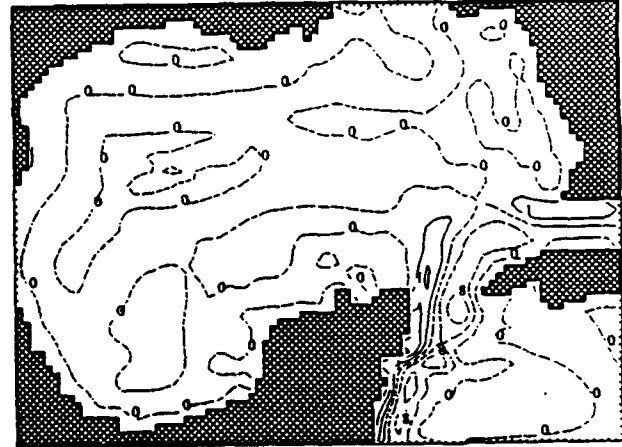
A1 / 14 P(eq. (5a, cm) and Vel(cm/sec) at day 60, depth= 10.0 m. Pdif= 62.3, Vmax=133.4



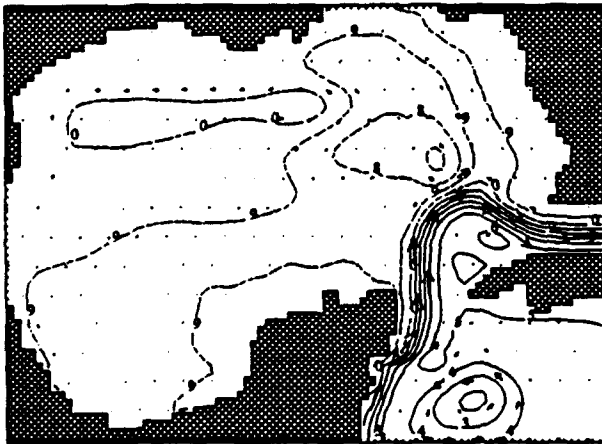
A1 / 13 vorticity (per week) at day 60, depth= 10.0 m. min=-21.2, max= 25.8



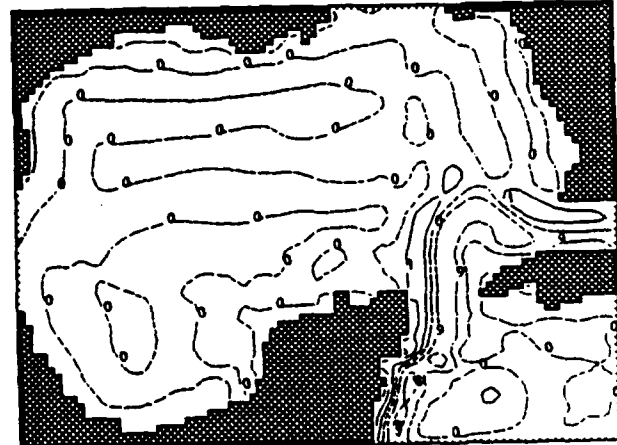
A1 / 79 P(eq. (5a, cm) and Vel(cm/sec) at day 90, depth= 10.0 m. Pdif= 48.2, Vmax=107.0



A1 / 78 vorticity (per week) at day 90, depth= 10.0 m. min=-17.6, max= 20.9



A1 / 223 P(eq. (5a, cm) and Vel(cm/sec) at day 210, depth= 10.0 m. Pdif= 48.0, Vmax=103.8



A1 / 224 vorticity (per week) at day 210, depth= 10.0 m. min=-17.3, max= 21.4

PRESSURE AND VELOCITY

VORTICITY

Figure 17. Top Layer Case A1 Results. Pressure units are equivalent free-surface height anomaly in cm. Pdif is Pmax - Pmin. Velocity units are cm/sec. Vorticity units are per week.

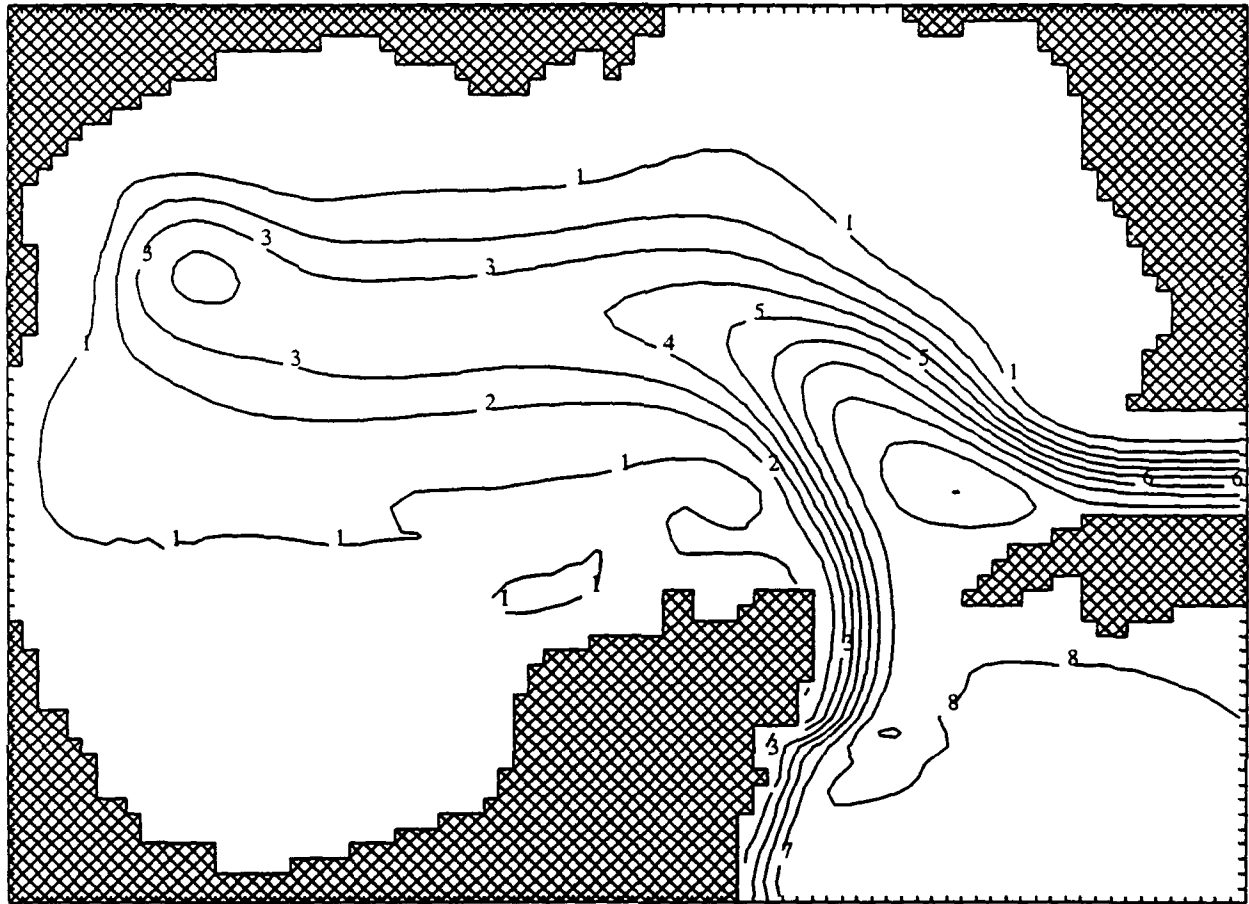


Figure 18. Eddy-Shedding Case A1 Time Average Free Surface Height Anomaly for Days 0 to 2160. Ten Contours are uniformly distributed between the maximum and minimum.  $P_{max} - P_{min} = 46$  cm.

The result is no eddy shedding at all during a four-year simulation. There is a persistent cyclonic block, as indicated by the time averaged flow (Figure 19). This cyclonic block contrasts with the time averaged flow of the eddy shedding case (Figure 18). The eddy shedding Case A1 shows an anticyclonic time-averaged flow in the deep water of the central GOM because of the regular anticyclonic shed-eddy passage. On the other hand, the non-eddy-shedding Case A1B shows a cyclonic deep water flow, although a relatively narrow Loop Current figure occasionally bulges northward along the Florida Shelfbreak.

Starting from the eddy shedding Case A1 results at three years, with diffusivity reduced to the A1B value, also leads to a non-eddy-shedding regime; only one further eddy shedding (at about day 1500) occurs during the next three years, while continuation of Case A1 with its larger  $20 \text{ m}^2/\text{sec}$  diffusivity leads to continued eddy shedding, with eddies shed at days 1160, 1410, 1700, and 1970.

Thus, there is a high Reynolds number cutoff to eddy shedding with the present model. Such cutoff has not previously been noted. This is consistent with all of our results, as Table 1 indicates.

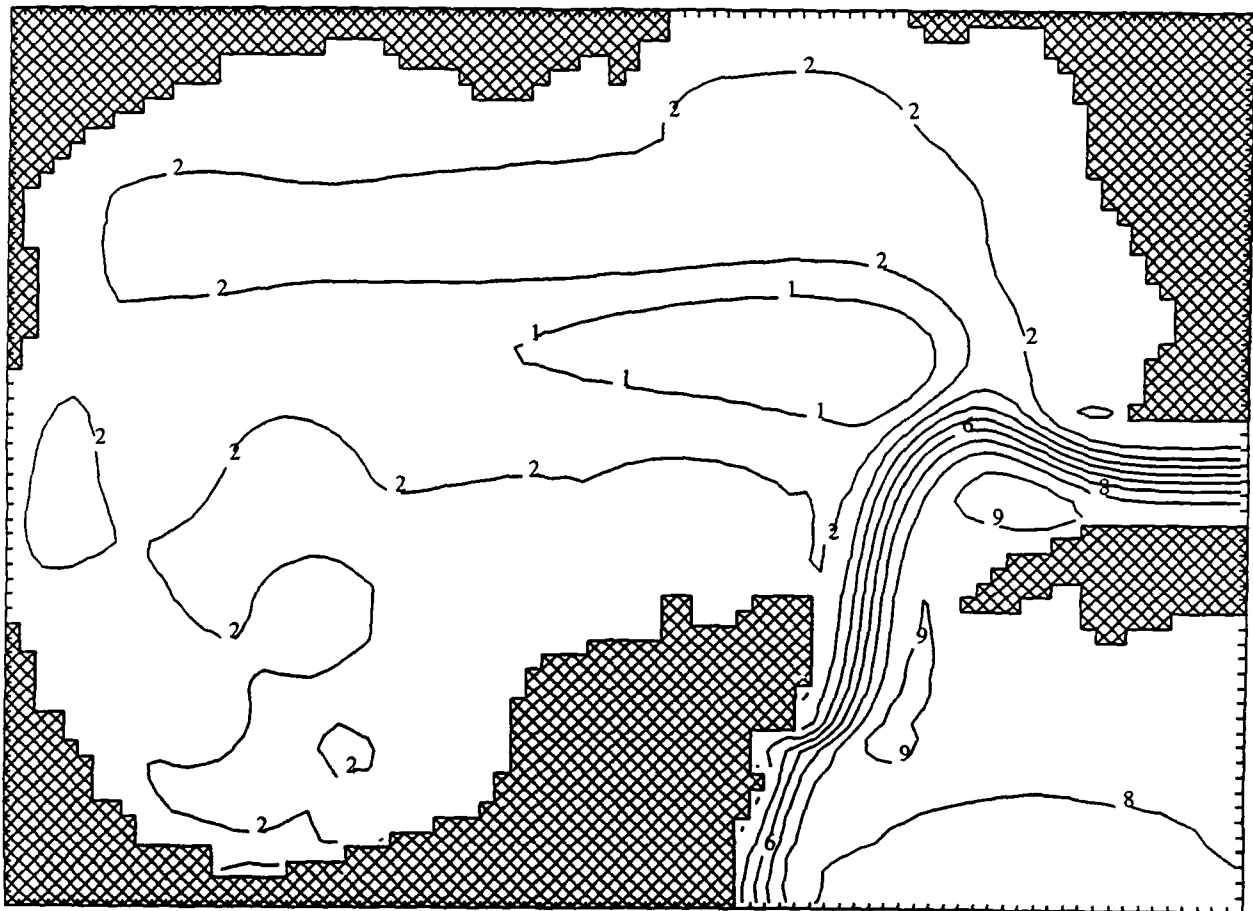


Figure 19. As in Figure 18 except results are from non-Eddy-Shedding Case A1B for Days 0 and 1440. Case A1B is similar to A1 except for smaller lateral diffusivities.  $P_{max} - P_{min} = 49$  cm.

### 5.2.3 On Using Ultra-Low Lateral Diffusivity

The small Case A1B lateral diffusivity ( $2 \text{ m}^2/\text{sec}$ ) is in the range of plausible values, although much smaller than typically used by other models with 20 km resolution. We have found (see Section 4.1) that the larger values:

- Significantly reduce the maximum Loop Current velocities;
- Strongly diffuse sharp fronts as Loop Current eddies propagate through deep water; and
- Greatly reduce the strength of paired cyclonic eddies that are similar to those that are observed in the western GOM.

Using such small lateral diffusivity is numerically acceptable only if enough dissipation and dispersion occurs (by bottom drag, vertical diffusivity, internal waves and numerical effects); energetic eddies with diameters 50 km or less must not dominate the deep water flow, where the natural eddy scales are larger. If the energy spectrum had a large component in the smallest resolved scales, it would be desirable to increase the resolution and/or the lateral diffusivity.

Three uniquely geophysical factors limit the development of small scale flow components. First, the resolved flow is quasi-linear; the momentum equations are quasi-geostrophic, with the barotropic mode being dominated by the linear beta term; and even the omega equation for quasi-geostrophic

vertical velocity is dominated by the linear beta term. Second, the flow tends to be nearly parallel to density contours, especially near fronts, thus reducing nonlinear term amplitudes in the density equation. Third, flow variations that are small compared to the Rossby radius of deformation tend to disperse rapidly. These factors tend to reduce energy cascades compared to other transient effects, while allowing enstrophy cascades and front formation. Although fronts contain small scale components, they have more energy in large scale components, as in the Fourier series of a step function.

These uniquely geophysical factors plus physical/numerical dissipative/dispersive effects, are sufficient to keep the small scale activity that develops at reasonable amplitudes in the results. The numerical effects are small compared to the extra dissipation that would occur by using the lateral diffusivities normally used with 20 km resolution. However, even with the unconventionally low lateral diffusivity of 2 m<sup>2</sup>/sec used, the flow does not become dominated by small scale eddies.

Section 5.3.3 results show that short-lived small-scale [O(100) km] eddies occasionally develop in deep water. This occurs by instability rather than by energy cascade near sharp, shallow Loop Current fronts. These apparent baroclinic instabilities are reasonably resolved with the 20 km resolution used. Otherwise, small-scale eddies tend to develop only in shallow regions, especially near shelfbreak fronts, consistent with the relatively small local Rossby radius of deformation. When advected toward deeper water, with larger local Rossby radius of deformation, these tend to organize into larger-scale flows.

### 5.3 Simulations Based on Detailed Caribbean Inflow Observations

After running the Section 5.2 cases, and examining a study on the sources of the Florida Current by Schmitz and Richardson (1991), we decided to modify our Caribbean inflows to more closely reflect this new information. The main difference was to use a time averaged Yucatan flow of 29 instead of

27.5 Sverdrups, with a larger portion coming through the Windward Passage than we initially assumed.

The modeled region is north of the other Caribbean main passages. It is reasonable to assume that water entering these passages organizes into a western boundary current before entering the southern limit of the Northern Caribbean region modeled. It is also reasonable to assume the Windward Passage water crosses the modeled Caribbean region and forms a western boundary current, because the weak Caribbean wind stress curl does not support much latitudinal excursion. In the present "first cut" calculation, which starts west of the Windward Passage, we treat this water as a latitudinally uniform inflow at the model eastern boundary in the Caribbean.

#### 5.3.1 Caribbean Inflow Conditions

A laterally constant initial temperature is specified everywhere. The bottom temperature (at 3500 m depth) is 6°C. A vertical temperature gradient of 0.2°C per kilometer is then used to determine the initial temperature up to about 200 meters depth, at which the stratification is increased to 40°C per kilometer and a temperature jump of 15°C is added. This gives a maximum interior initial temperature of about 26°C. The higher vertical resolution used addresses deep water stratification patterned after observations.

The eastern inflow temperature matches the initial interior temperature except that a latitudinal temperature gradient is added which depends only on depth. Its largest value is at about 200 meters depth (where it has a total difference of 5°C between the southern coast of Cuba and the southern boundary of the modeled Caribbean region). It drops rapidly away from that depth with a decay scale of 50 m. It is added by integrating northward starting by assigning the specified initial stratified interior value for each depth at the southern boundary of the eastern inflow region. To get inflow trapped in the upper layers, the temperature must increase with latitude in this region.

The eastern inflow velocity is zero at the bottom. Its remaining values are then derived

from the geostrophic thermal wind relation. The resulting total eastern inflow is given in Table 2. The remainder of the specified total inflow is put in a barotropic western boundary current inflow, a 60 km wide uniform jet. Its inflow temperature matches the initial stratified interior value at each depth.

The eastern inflow temperature distribution for all cases in this section is shown in Figure 20. It is dominated by a sloping, realistically strong thermocline.

As indicated previously by Figure 2, the model accurately simulates the mean thermocline. The model's deep water temperature is 6°C in both the initial conditions and the water entering the Caribbean, rather than the 5°C observed. The linear equation of state used is optimized for the large gradient region near the surface, and gives a bottom density at 6°C equal to the true nonlinear value at 5°C.

### 5.3.2 Diffusivity Effects with 29 Sverdrup Inflow

The first case with the estimated 29 Sverdrups Caribbean inflow (Case B1-Table 2) uses the same lateral diffusivities as the eddy shedding Case A1. The result is no eddy shedding until day 800, and no more at least through day 1440.

One might get regular eddy shedding with the inflow and lateral diffusivities used in Case B1 by using higher resolution including the entire Caribbean with accompanying better inflow representation in the simulation or including a realistic annual cycle. However, in view of the results in Section 5.2, it is reasonable to increase the lateral diffusivity. We found that increasing to 40 m<sup>2</sup>/sec still does not lead to regular eddy shedding (Case B1A-Table 2), although the single eddy shedding occurs earlier. By further increasing to 100 m<sup>2</sup>/sec regular eddy shedding results (Case B1B-Table 2), the eddy shedding period is about 225 days (Figure 21). Although a temporary cyclonic block occurs early in time, the cyclone quickly expands, propagates westward because of Rossby wave effects, and decays in Figure 22. Cases B1A and B1B are identical to B1 except for their larger lateral diffusivities.

### 5.3.3 Low Diffusivity 27.5 and 25 Sverdrup Cases

These results led us to two experiments, which are identical to the non-eddy-shedding low diffusivity 29 Sverdrup Case B1 except the Yucatan flow is reduced. Smaller than average inflows are of interest because there is a substantial annual cycle. Case B2 (Table 2) assumes 27.5 Sverdrups. The results still do not show regular eddy shedding. Case B3 (Table 1) assumes 25.0 Sverdrups. After running B3, we found that recent observations (Hamilton, 1992) give 25 Sverdrups as a best estimate of the annual averaged flow through the Florida Strait. This leads to regular eddy shedding, with excellent agreement with many observations.

After an initial transient, eight eddies were shed during the seven year simulation. The approximate eddy shedding times were: 570, 900, 1210, 1490, 1730, 1950, 2220, and 2480 days. This gives a mean eddy shedding period of 254 ((2480-1210)/5) days after the third eddy is shed, close to the observed 37 week average period (Sturges and Welsh, 1991). Figure 23 shows this eddy shedding during the last 600 days. The upper level GOM flow is in near statistical equilibrium with eddy phase velocities about 4 cm/sec, and significant intensification of eddy activity occurs near the western GOM continental shelf. This intensification is further indicated by GEOSAT observations and model results (rms sea surface height deviation from its long term average) in Figure 24. The rigid-lid SOMS gives better comparison with the rms free-surface height anomaly from satellite observations than results from the two free-surface models also shown in Figure 24. This indicates that the model transient eddy activity is consistent with observations.

All three models shown in Figure 24 use an Arakawa "c" staggered grid for horizontal representation. The NRL model uses a three-layered vertical representation with constant inflow and monthly wind forcing. The Princeton model uses sigma vertical coordinates with 21 levels. The SOMS model used 20 z-levels. All calculations were done with about 20 km lateral resolution.

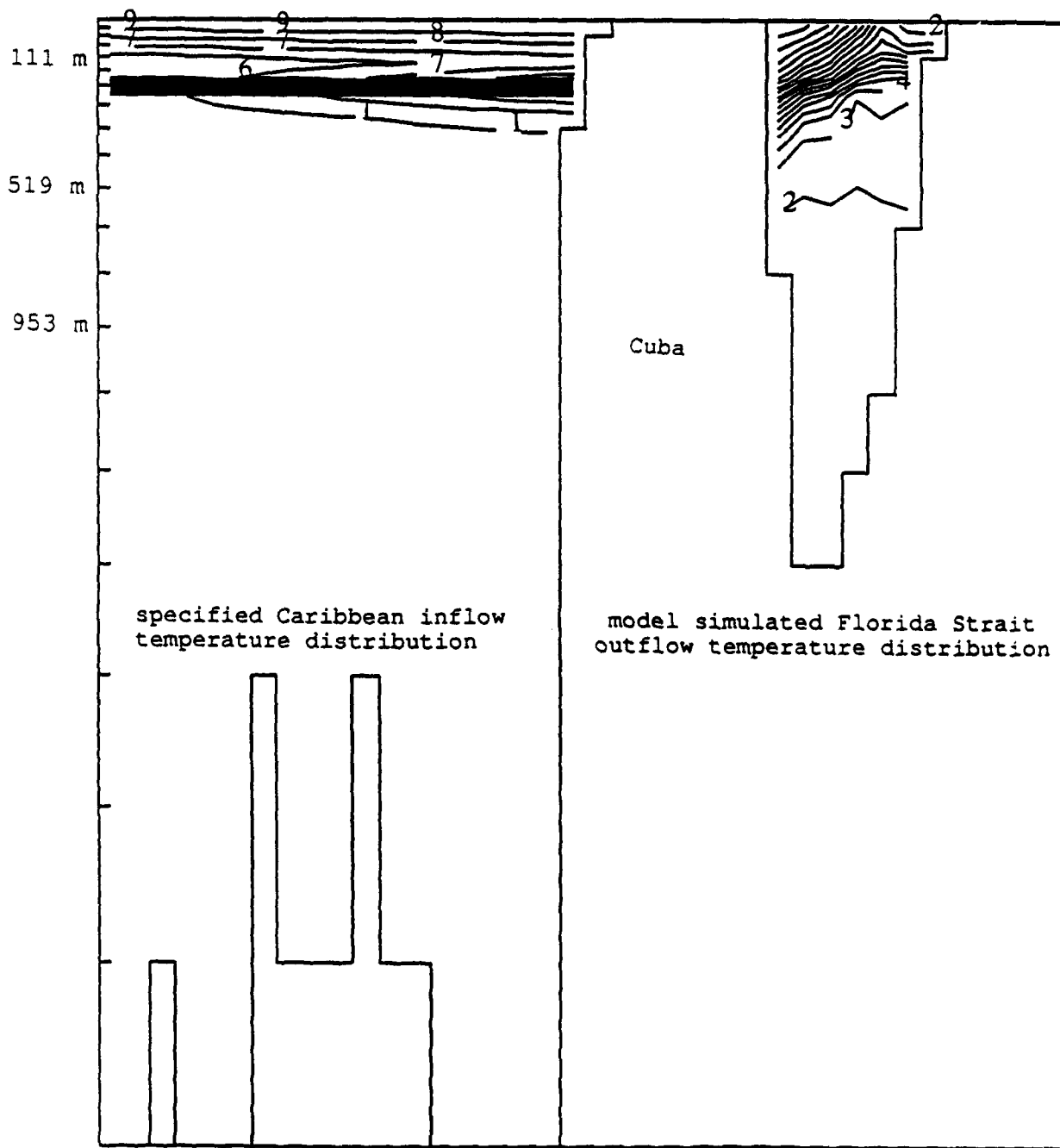


Figure 20. Latitude/Depth Section of Eastern Boundary Temperatures. Twenty contours are uniformly distributed between the maximum (26.7°C) and minimum (6.0°C). The single-digit contour labels are given by  $N = \text{MOD}(M, 10)$ , where  $M = (T - 6.0) \times 20.1 / (26.7 - 6.0)$ . The flow is weakly stratified (0.2°C per km) in the deep water. No contours appear below 1000 m because less than one degree variation occurs there.



Figure 21. Longitude/Time Section of Equivalent Free Surface Height Anomaly ( $P$ ) for Case B1B covering Days 840 to 1440.  $P_{max} = P_{min} = 51$  m.

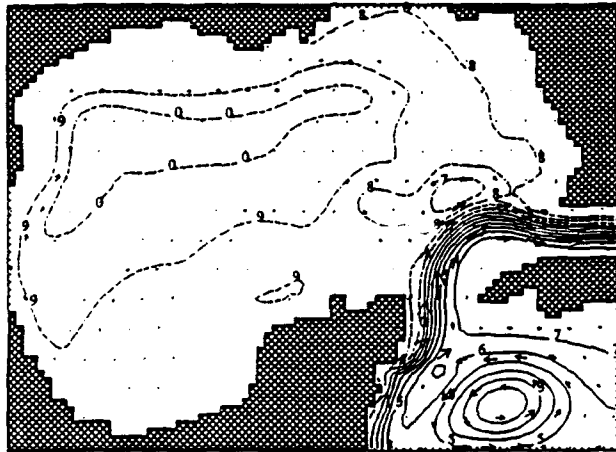
Regards calculation time, the NRL model was by far the fastest. The Princeton model included the most physics and required the most computation.

Both the amplitude and location of the primary and secondary maximums from SOMS agree well with observations. Further, the decay of eddy activity west of the primary maximum is in reasonable agreement with observations. This clearly demonstrates the applicability of rigid-lid models to the GOM general circulation. Tidal effects have been removed from the satellite data. Tides have little effect on the much longer time scale flow components that dominate the GOM general circulation.

The excellent comparison of SOMS results with the GEOSAT data reflects a

combination of low dissipation, accurate Coriolis term treatment (Dietrich, et al, 1990; Dietrich, 1993), and realistic representation of continental shelf processes.

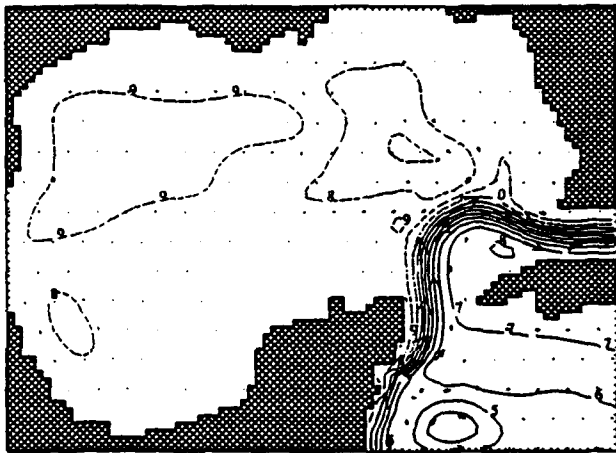
Brooks and Kelly (1986) discuss the development of a paired cool-core positive vorticity eddy on the north side of an old warm-core negative vorticity Loop Current eddy near the western GOM shelfbreak. Our results show similar behavior each time an eddy reaches the western GOM shelfbreak (see Figure 5). Merrell and Morrison (1981) report a similar paired eddy event (Figure 25). Similar comparison of NRL model GOM results with this vortex pair is noted by Hurlburt (1984), and qualitative similarity of idealized calculations is noted by Smith and O'Brien (1983).



B1B/ 79 P(eq. (sa, cm) and Vel(cm/sec) at day 90, depth= 10.0 m. Pdf= 38.9, Vmax=125.0



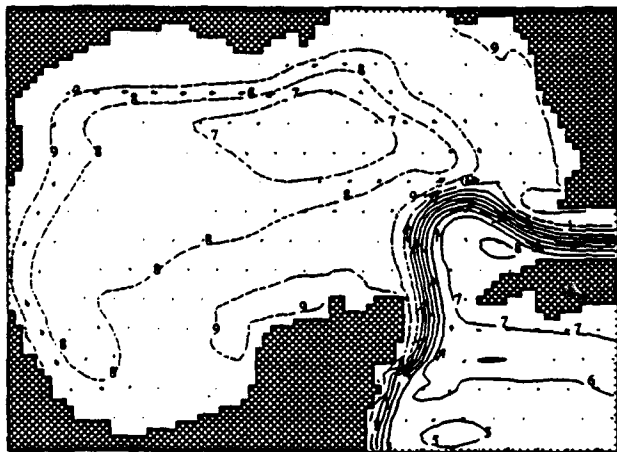
B1B/ 379 P(eq. (sa, cm) and Vel(cm/sec) at day 360, depth= 10.0 m. Pdf= 64.5, Vmax=118.1



B1B/ 160 P(eq. (sa, cm) and Vel(cm/sec) at day 180, depth= 10.0 m. Pdf= 56.7, Vmax=122.5



B1B/ 598 P(eq. (sa, cm) and Vel(cm/sec) at day 540, depth= 10.0 m. Pdf= 90.8, Vmax=139.4



B1B/ 298 P(eq. (sa, cm) and Vel(cm/sec) at day 270, depth= 10.0 m. Pdf= 61.0, Vmax=118.6



B1B/ 839 P(eq. (sa, cm) and Vel(cm/sec) at day 720, depth= 10.0 m. Pdf= 85.8, Vmax=129.2

Figure 22. Top Layer Case B1B Results.

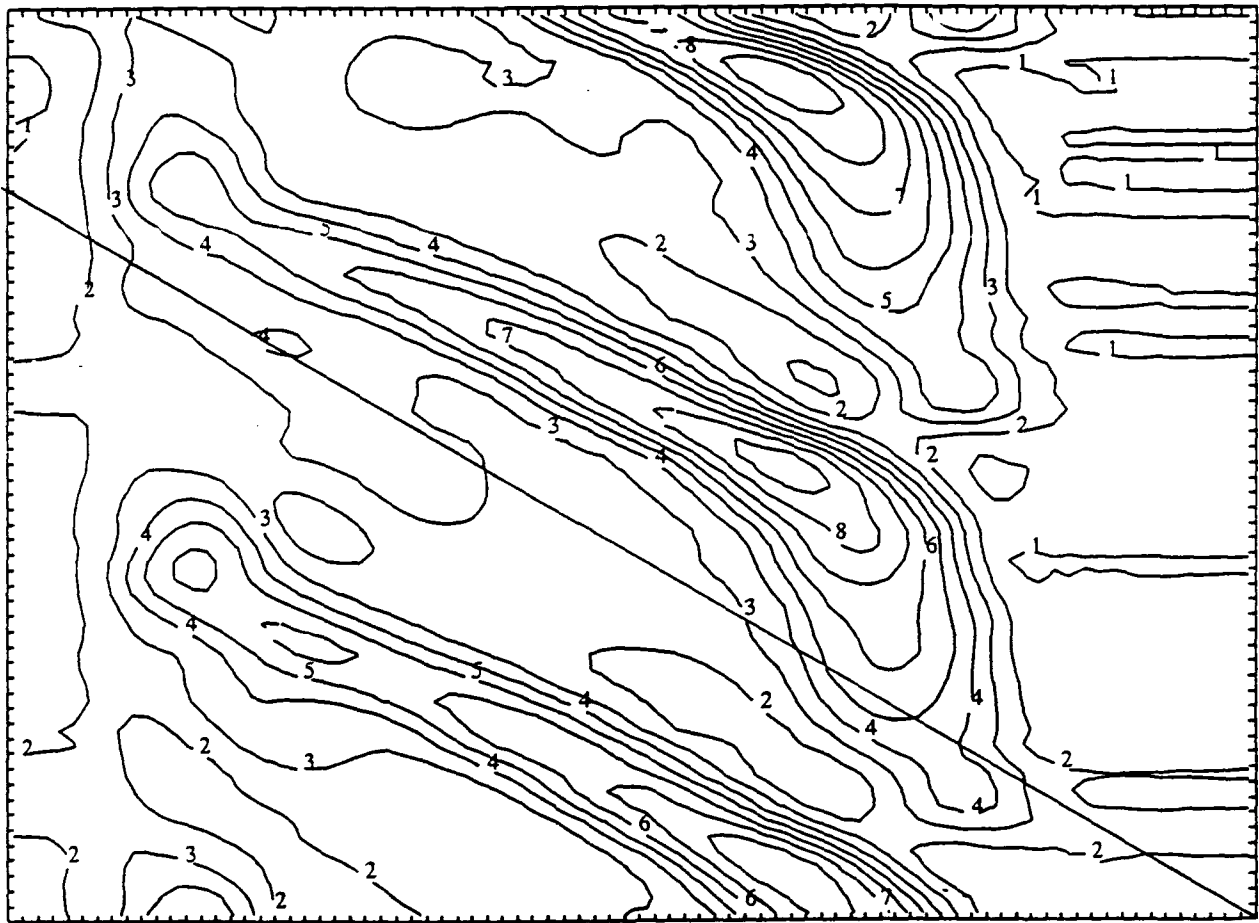
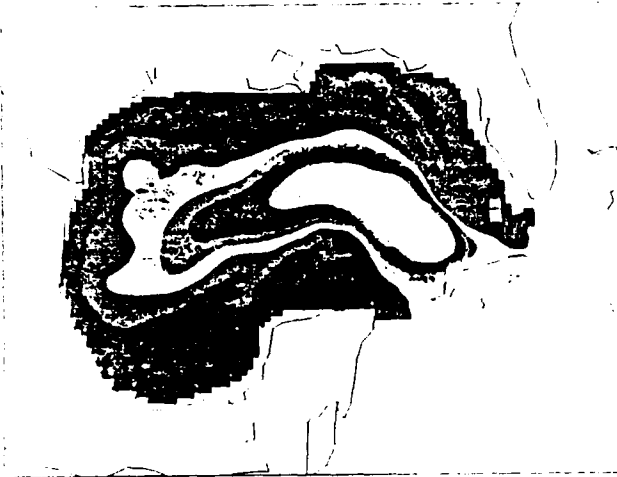


Figure 23. Longitude/Time Section of Equivalent Free Surface Anomaly ( $P$ ) for Case B3 covering Days 1920 to 2520.  $P_{max} - P_{min} = 49$  cm.

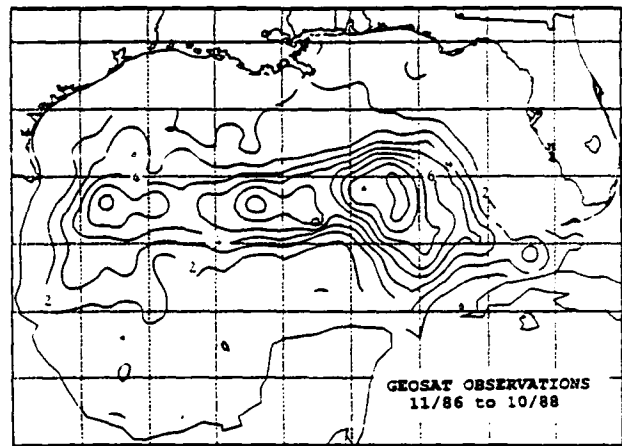
Our model and the Brooks and Kelly observations (see Figure 5) show the formation of a paired cool-core cyclonic eddy on the north side of an old warm-core Loop Current eddy. Both show a small-scale paired eddy at the shelfbreak early in the development, and a larger-scale, stronger paired eddy on the north side of the old Loop Current eddy about 75 days later. The longer time sequence in the Figure 26 series also shows that our modeled old warm-core eddy moves eastward on a longer time scale similar to the Brooks and Kelly observations. Such western GOM vortex pairs are common in our simulations. Figure 27 shows a sequence of GEOSAT SSH measurements that is quite similar to Figure 26, especially during the first 120 days.

Figures 23 to 27 and Figures 2 to 5 show that our SOMS model simulates observed shelf and deep water phenomena even though no observations have been assimilated by the model. This clearly demonstrates its ability to address continental shelf and deep water dynamics, including their interactions across shelfbreaks. We now discuss this interaction in more detail, based on our model results.

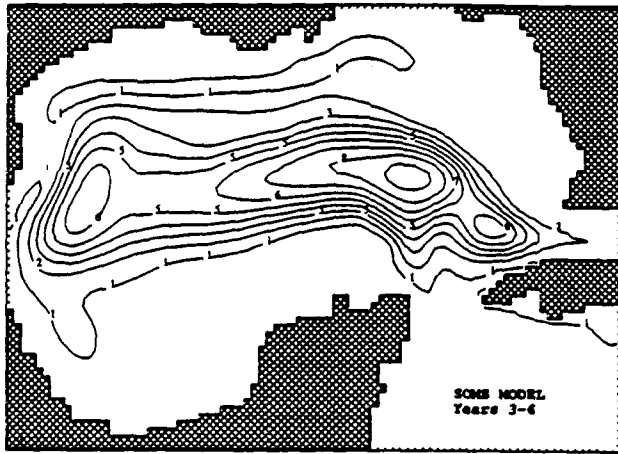
When an old warm core Loop Current eddy reaches the western GOM continental shelfbreak, cool positive vorticity water is generated on the shelf by the mechanisms described in Section 5.4. There is a rapid steepening and concentration of the isotherms above the shelfbreak as seen in Figure 28. The longitudinal line in the first panel in Figure 26 shows the location of these vertical



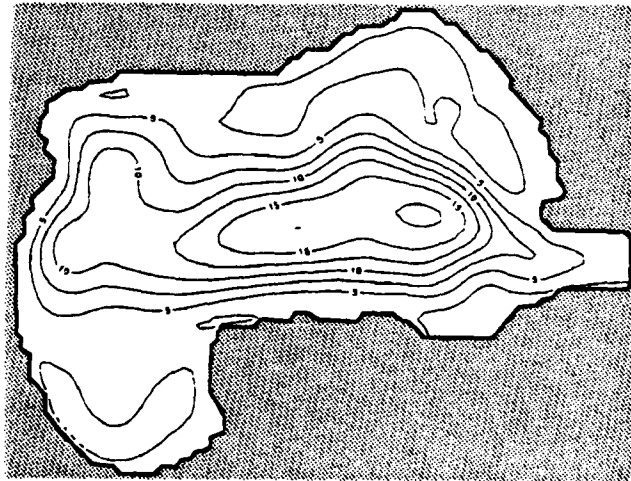
Princeton Model Max=25.0 cm



RMS SSH Variation from GEOSAT  
Max=24.0 cm



SOMS Model Max=23.8 cm



NRL Model Max=17.9 cm

*Figure 24. Intercomparison of Princeton, NRL, and SOMS models outputs and GEOSAT data. Princeton model output provided by Dr. Dana Thompson and Dr. Lakshmi Kantha. NRL model output provided by Dr. Thompson and Dr. Alan Wallcraft. Contour intervals are 2.5 cm in each case.*

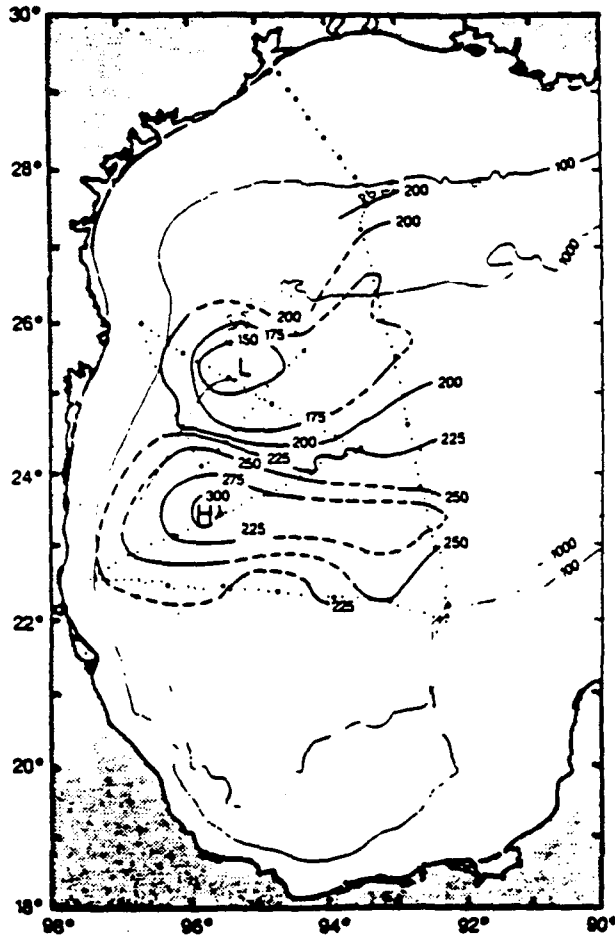


Figure 25. Counter-rotating vortex pair in the western GOM shown as the depth of the 15°C isotherm (in meters) observed April 1978. The cyclonic vortex is to the north and the anticyclonic is to the south. The contour interval is 25 m (Merrell and Morrison, 1981).

cross-sections. Figure 28 shows the substantial upwelling of about 5 meters per day that occurs near the shelfbreak, along with positive vorticity on the shelf. The vorticity front, along with cool shelf water, can be advected off the shelf by the northeastward current maintained near the shelfbreak by the westward movement of the old warm core eddy. Figures 26 to 28 reveal this behavior. Figure 26a-c show the time sequence of the top level (10 m below surface) fields every 30 days between day 1920 and 2070. Figure 26b shows that the central core vorticity of the Loop Current and separated eddies is nearly constant, indicating near-rigid

body rotation. Eddy decay occurs primarily through erosion of its outer fringe vorticity; the central core negative vorticity remains relatively constant while its diameter gradually decreases.

The location and orientation of the front and shelfbreak region flow at day 1920 is similar to observations (Vidal, et al 1992). As the separated cool positive vorticity water is advected toward deeper water on the north side of the old warm-core eddy, quasi-geostrophic dynamics can result in its organization into larger-scale eddies more appropriate for regions with larger Rossby radius of deformation as shown in Figure 26. This time sequence of eddy interaction near the western GOM shelfbreak is similar to the results of Smith and O'Brien (1983). We note the roles of the energy absorbing nonlinear critical areas, and the upwelled cool-shelf water advection off the shelf, in addition to offshore advection of positive shelf vorticity. Without the cool water reinforcement, the offshore cyclonic eddy would not develop as strongly as it does. The reason is that in the absence of cool-water advection, upwelling would occur under the region of offshore positive vorticity advection according to the quasi-geostrophic omega equation. The resulting upper level divergence would then reduce the cyclonic surface vorticity. The cool water offshore advection opposes this, resulting in a stronger surface cyclone.

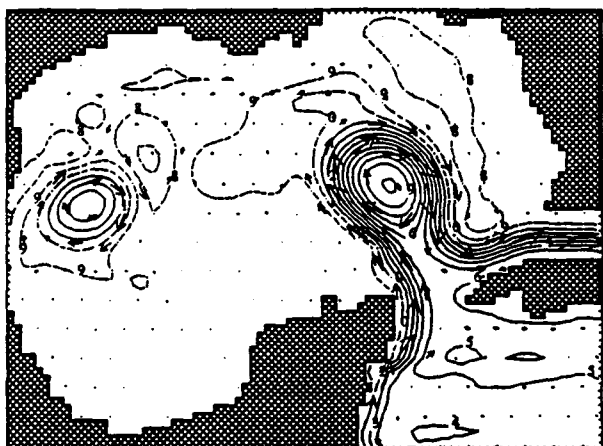
Sometimes the cold core cyclonic eddy grows, at the expense of the dissipating old warm core anticyclonic Loop Current eddy, until it has more energy than the old warm core eddy. It can then move southward, splitting the old warm core eddy, and/or reverse its formation process. The latter leads to a new warm core eddy, or an intensification of the old one, on its south side. This involves downwelling on the western GOM shelf as the cold core eddy moves westward and dissipates. This westward movement occurs due to its increased size, and the greatly weakened offshore advection by the old warm core eddy. At day 2040, we see that the dissipating cold-core eddy has also advected the warm core eddy eastward, where it is about to merge with a new warm core Loop Current eddy. Again, we note similar behavior by Brooks and Kelly.



B3 / 225 P(eq. fsa, cm) and Vel(cm/sec) at day 1921, depth= 10.0 m. Pdf= 64.3, Vmax=112.8



B3 / 438 P(eq. fsa, cm) and Vel(cm/sec) at day 2011, depth= 10.0 m. Pdf= 62.8, Vmax= 91.9



B3 / 296 P(eq. fsa, cm) and Vel(cm/sec) at day 1931, depth= 10.0 m. Pdf= 67.0, Vmax=112.4



B3 / 509 P(eq. fsa, cm) and Vel(cm/sec) at day 2041, depth= 10.0 m. Pdf= 57.9, Vmax=91.4

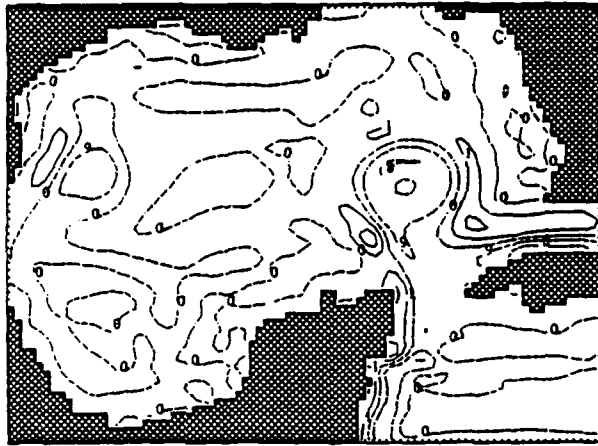


B3 / 367 P(eq. fsa, cm) and Vel(cm/sec) at day 1981, depth= 10.0 m. Pdf= 63.7, Vmax= 99.6

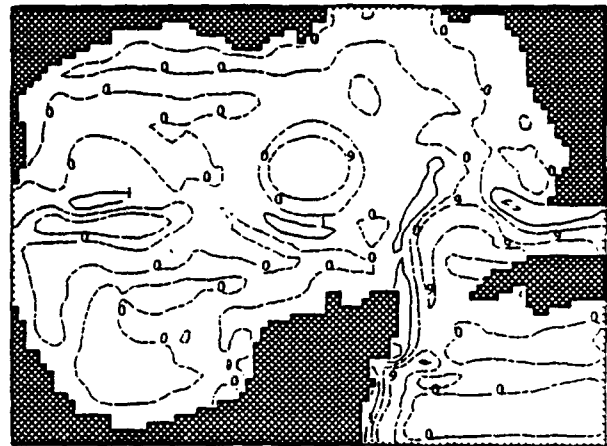


B3 / 580 P(eq. fsa, cm) and Vel(cm/sec) at day 2071, depth= 10.0 m. Pdf= 51.3, Vmax=105.1

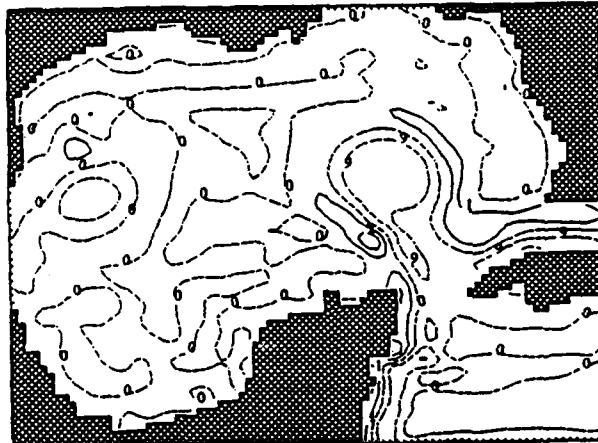
Figure 26a. Top Layer Case B3 results for Pressure and Velocity.



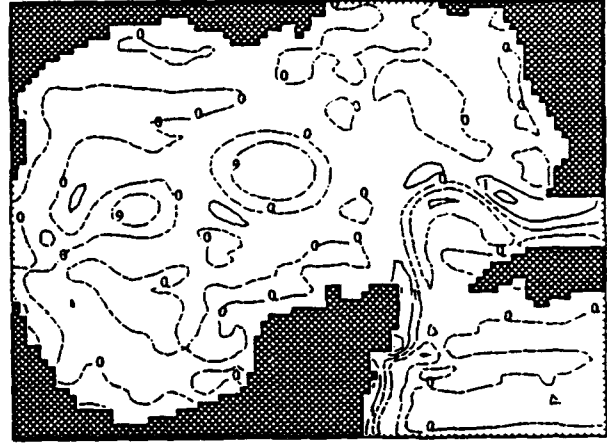
B3 / 224 vorticity (per week) at day 1921, depth= 10.0 m. min=-16.6, max= 21.6



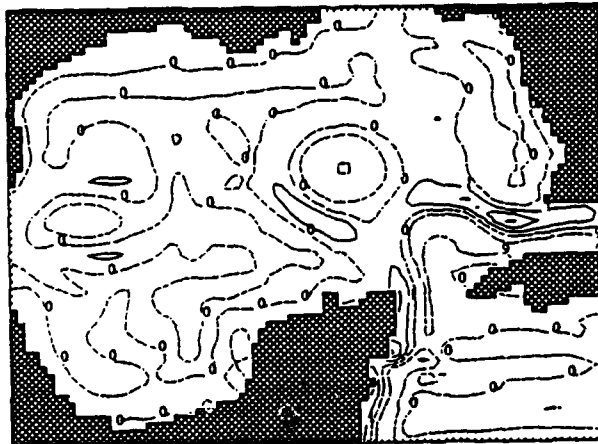
B3 / 437 vorticity (per week) at day 2011, depth= 10.0 m. min=-15.3, max= 21.6



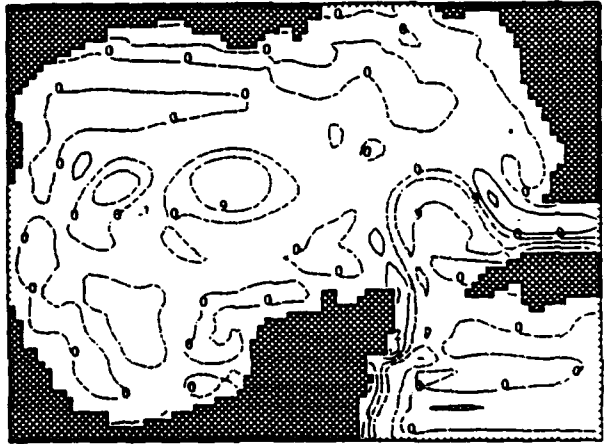
B3 / 293 vorticity (per week) at day 1951, depth= 10.0 m. min=-15.5, max= 22.1



B3 / 508 vorticity (per week) at day 2041, depth= 10.0 m. min=-15.3, max= 22.1

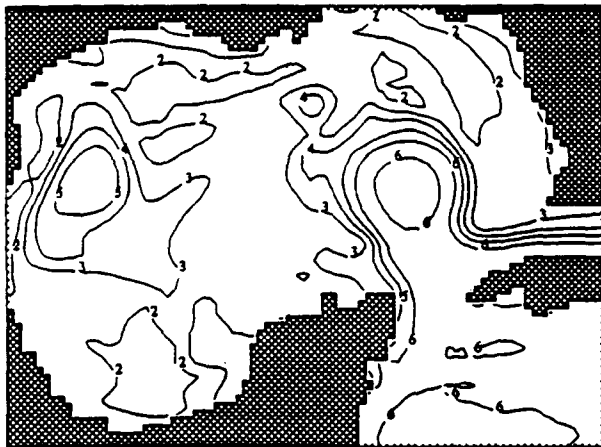


B3 / 366 vorticity (per week) at day 1981, depth= 10.0 m. min=-15.4, max= 23.0

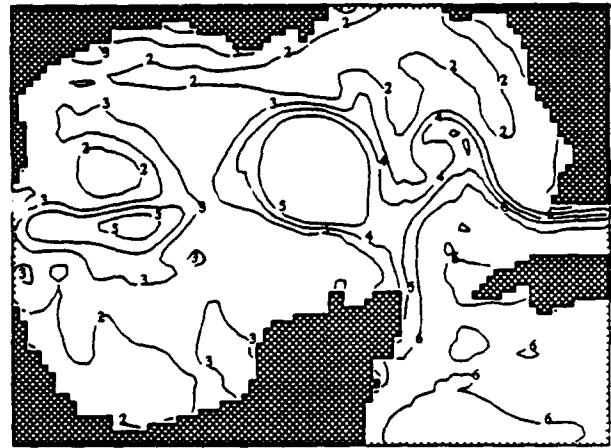


B3 / 579 vorticity (per week) at day 2071, depth= 10.0 m. min=-15.2, max= 22.7

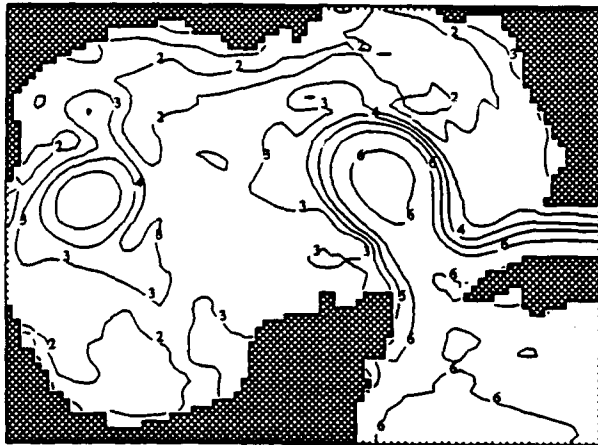
Figure 26b. Top Layer Case B3 results for Vorticity.



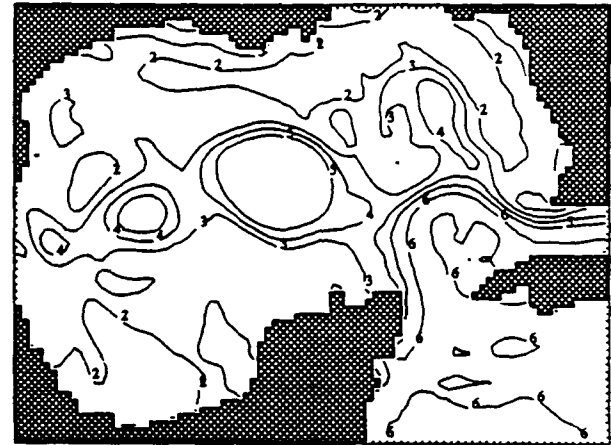
B3 / 226 temperature (degrees c) at day 1921, depth= 10.0 m. min= 20.4, max= 27.8



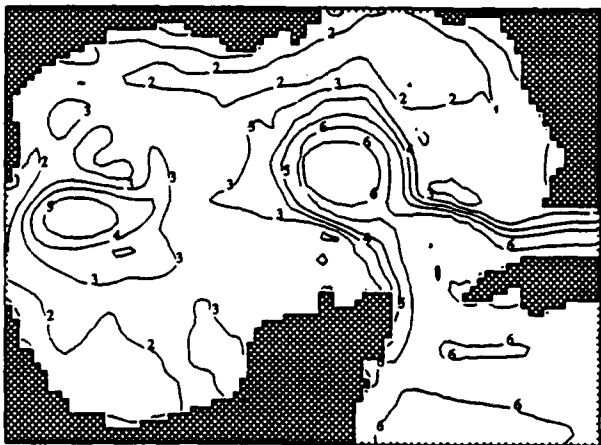
B3 / 499 temperature (degrees c) at day 2011, depth= 10.0 m. min= 20.7, max= 27.7



B3 / 297 temperature (degrees c) at day 1951, depth= 10.0 m. min= 20.7, max= 27.7



B3 / 510 temperature (degrees c) at day 2041, depth= 10.0 m. min= 20.0, max= 27.8



B3 / 368 temperature (degrees c) at day 1981, depth= 10.0 m. min= 20.4, max= 27.7



B3 / 581 temperature (degrees c) at day 2071, depth= 10.0 m. min= 20.6, max= 27.9

Figure 26c. Top Layer Case B3 results for Temperature.

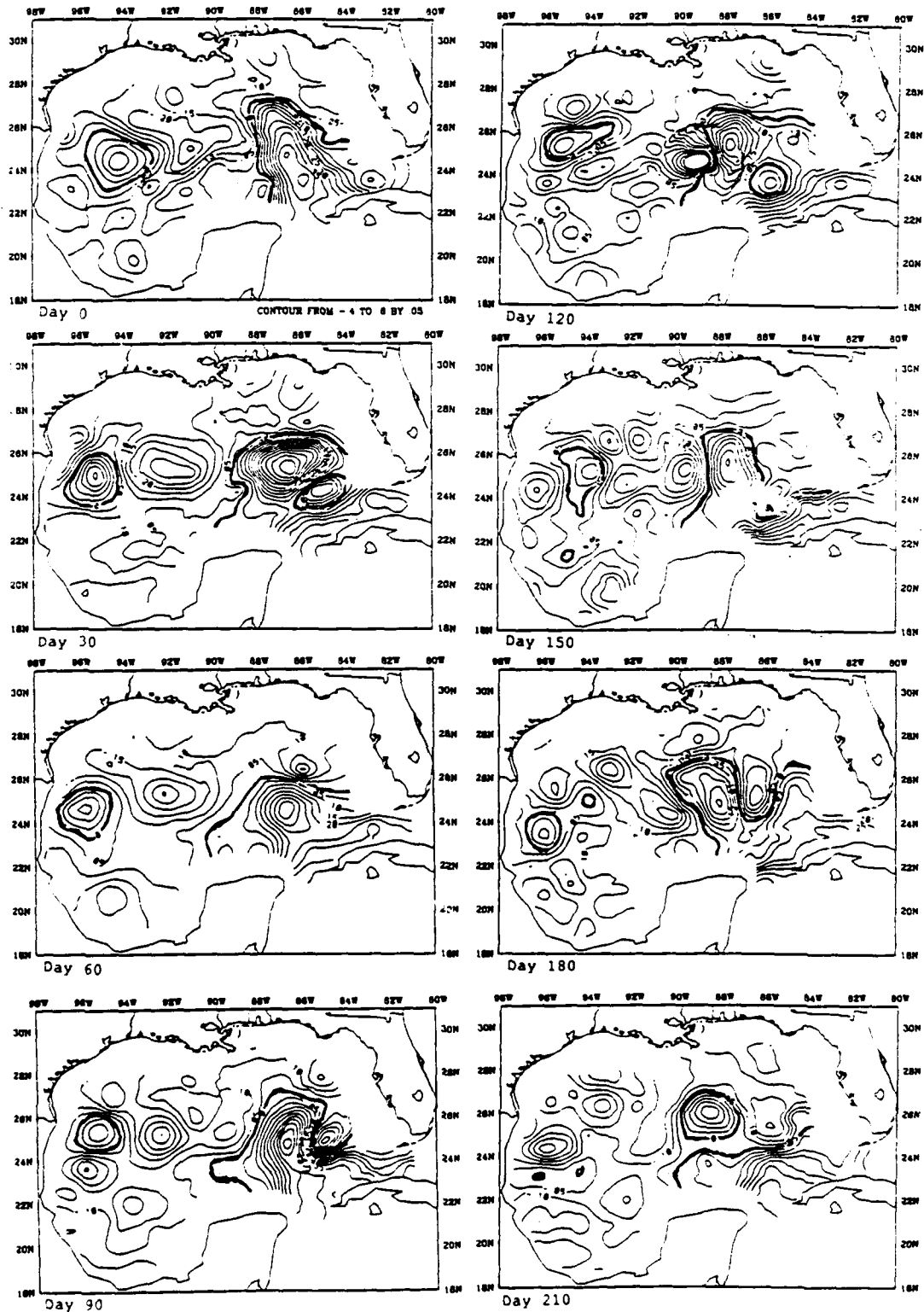


Figure 27. GEOSAT observations of SSH every 30 days from May 8, 1987 to March 3, 1988. An area average has been subtracted out to help identify high and low areas. The zero line defining the Loop Current and western GOM warm-core eddy locations is darkened.

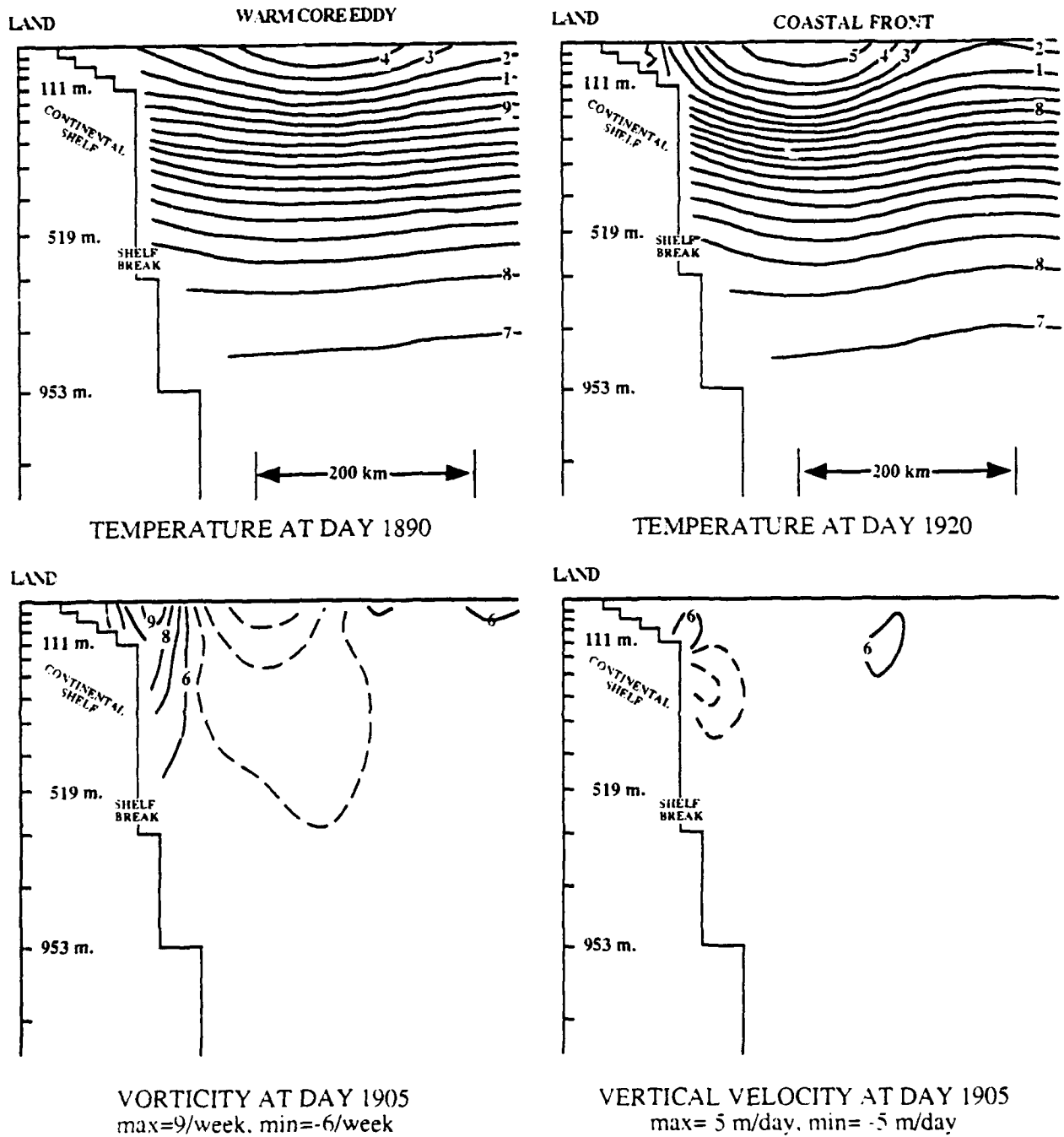


Figure 28. Longitudinal/depth sections of temperature, vorticity, and vertical velocity from model simulation showing interaction of warm-core eddy with continental shelf. Negative contours (i.e., anticyclonic vorticity, upwelling) are dashed.

Typically, the offshore flow between the eddies occurs in a jet spurt, with a front between them. The warm-core eddy usually occurs on the south side of the cold-core eddy as they interact through nonlinear western GOM continental shelf processes (relatively small-scale vorticity generation and cool water upwelling, followed by offshore advection), but sometimes the parent eddy advects one or more new eddies around itself before they can collectively absorb a major part of the parent eddy energy.

These processes are "catalytic", in that the shelf regime dynamics results in significant energy transfer among deep water eddies, even when energy accumulation on the shelf is relatively small. Potential energy is temporarily stored on the shelf, because of the cool water upwelling driven by pressure forces, then advected off the shelf by the deep water eddies where it is converted to eddy kinetic energy.

Thus, shelf processes act in a catalytic manner to transfer energy between paired deep water eddies. These processes are nonlinear, and involve bottom boundary layers, shelfbreak fronts, nonlinear quasi-geostrophic dynamics and, possibly, breaking internal waves and nonlinear critical areas.

## **5.4 Further Interpretation of Results**

### **5.4.1 Continental Shelf Water Formation**

A mechanism for the cool positive vorticity western Caribbean boundary current water follows. Rossby wave effects act to propagate the western boundary current onto the shelf. The current then experiences significant bottom drag in the shallower water. This reduces the along-shelf flow near the bottom, while creating a westward secondary bottom boundary layer flow. The reduced along-shelf flow, compared to the fast-moving boundary current core at the same depth to the east, implies positive vertical vorticity.

East of its axis, where its maximum velocity occurs, the western boundary current has negative vorticity. This reflects the beta term in the vorticity equation. If one assumes that the water entering the Caribbean has

relatively little vorticity, then the magnitude of the negative vorticity, in an element of western boundary current water, depends mainly on the difference between its latitude and the latitude at which it entered.

Therefore, increasing Caribbean inflow should have an asymmetric effect on the Caribbean western boundary current, and lead to a larger increase of positive vorticity on the shore side of the current axis than the increase of negative vorticity magnitude on the deep water side. This asymmetry favors Loop Current blocking by separated cool positive vorticity water.

The aforementioned secondary westward Ekman layer flow is toward shallower water, and implies upwelling of deeper, cooler bottom boundary layer water into shallower shelf bottom boundary layer regions. As the upwelling cooler Ekman layer water approaches the coast, it tends to form a return flow toward the shelfbreak in the upper levels, as illustrated by Figure 29. Thus, reduced velocity, cool upwelled water returns to upper levels near shelfbreak. (This upper level return flow opposes westward propagation of the boundary current. Accordingly, a quasi-balance between the off-shore advection by the return flow, and westward Rossby wave propagation, helps keep the positive vorticity region of the boundary current in a concentrated jet near the shelfbreak. Its equilibrium scale is such that onshore movement resulting from Rossby wave effects, roughly balances its offshore advection, thereby involving wave propagation, dissipation, and nonlinear effects. Loss of negative vorticity from the boundary current core by its westward propagation and dissipation by shelf bottom drag is opposed by the latitudinal advection "beta" contribution.)

In summary, low velocity, cool water accumulates in the shallow shelf regions. This is reflected by a steep shelfbreak front with concentrated vorticity.

### **5.4.2 Trapping of Separated Cool Positive Vorticity Water**

Some of the separated cool positive vorticity shelf water can be trapped north of

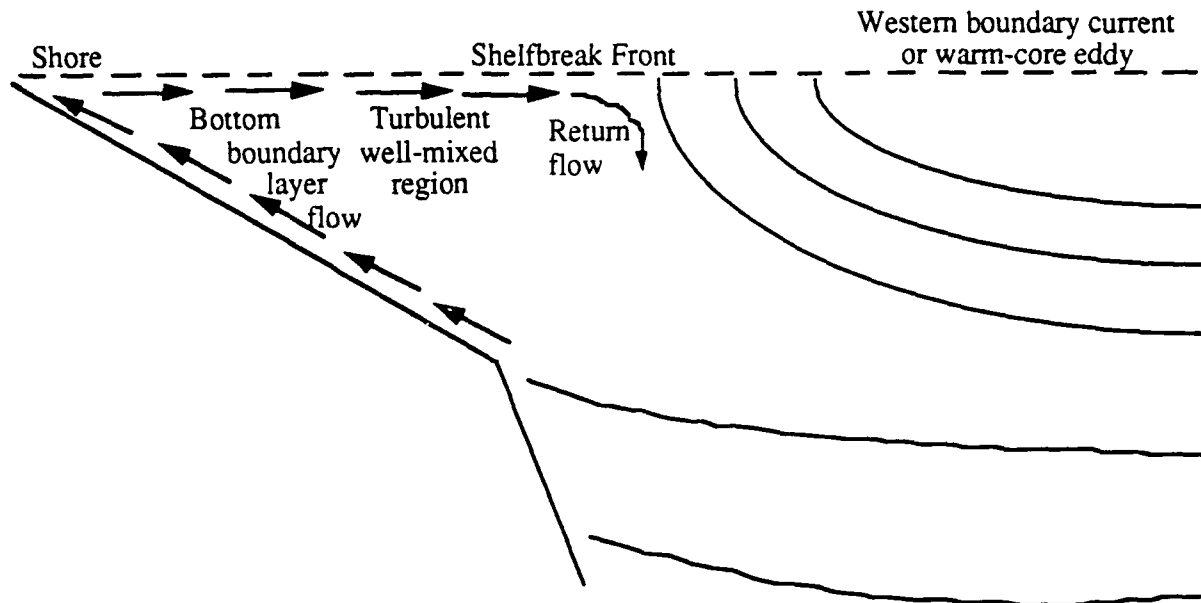


Figure 29. Schematic Shelf Flow. The arrows represent idealized mean flow that can lead to a shelfbreak front similar to the model results discussed by Gawarkiewicz and Chapman (1991).

the Loop Current in spite of its tendency to propagate westward due to Rossby wave effects. Such trapping is expected in regions where the off-shelf positive vorticity advection balances the westward propagation effect. In Case A1B such region forms on the north side of the Loop Current jet, where the separated cool positive vorticity water remains trapped (Figure 19). This trapping is affected by the Florida shelfbreak. Such trapping can also occur on the north side of separated Loop Current eddies when they interact with the western GOM continental shelf (Figures 5, 25, and 26). Such regions can be called nonlinear critical areas. These seem related but are not the same as the nonlinear critical layers of theoretical fluid dynamics (Warn, 1992). The critical areas are not fixed, as the effective advection velocity and Rossby wave speed of the dominant scale of the cool positive vorticity water vary with time. The dominant scale is affected by advection, diffusion and internal wave dispersion. Although a more complete description of what occurs requires discussion of absolute potential vorticity, these qualitative effects are seen in the model.

The trapping of cool positive vorticity water on the north side of the Loop Current

affects the eddy shedding dynamics. Although positive vorticity water would occur even without bottom drag, as a result of the Caribbean western boundary current separation, the bottom drag can also have a significant role. This trapping relates to the high Reynolds number cutoff of eddy shedding noted in Section 5.2.2.

Blocking by separated cool positive vorticity Caribbean shelf water constrains Loop Current penetration needed for eddy shedding. Even if the Loop Current penetrates, the separated positive vorticity can counteract the tendency for westward bending caused by quasi-geostrophic divergence effects.

Increasing lateral diffusivity eliminates the smallest scales in the narrow current of separated positive vorticity water. This facilitates its westward propagation together with the negative vorticity Loop Current core by Rossby wave effects. This favors eddy shedding, unless the diffusivity is so large that even the Loop Current core is strongly affected. More rapid eddy shedding is also expected with increasing diffusivity (compare Cases B3 and B3B). These interpretations are

consistent with our runs (Table 2). Thus, there is a diffusive destabilization of the Loop Current for intermediate diffusivities and stabilization for very large diffusivities.

The tendency for the larger-scale negative vorticity Loop Current core to propagate westward, more rapidly than the separated positive vorticity water immediately to its west, suggests a potential for the development of small-scale disturbances in this region. Our model results show many disturbances that mix the opposite vorticity water. The resulting diffused positive vorticity water can then propagate westward more rapidly.

Higher Reynolds number flows tend to separate sooner and more completely than lower Reynolds number flows. Thus, the very small Case A1B lateral diffusivities result in more complete separation of the Caribbean western boundary current than in Case A1; a larger portion of cool cyclonic vorticity water near the coast separates compared to the warm core negative vorticity water on the east side of the boundary current. The boundary current also separates further upstream, rather than following the Yucatan shelf depth contours around to the west, thus leading to separated positive vorticity water accumulation on the north side of the Loop Current. This leads to cyclonic flow dominating the GOM interior (Figure 19), and to a long term cyclonic block of the warm core Loop Current penetration needed for warm core eddy shedding.

In Case A1B, Rossby waves propagate the separated cool positive vorticity water westward until the entire GOM interior is filled with a cyclonic gyre, which then breaks up. The Loop Current penetration continues to be blocked by newly separated cool positive vorticity water from the Caribbean western boundary current although occasional narrow extensions propagate northward along the Florida shelfbreak and shed small short-lived warm-core eddies north of the persistent blocking cyclonic flow.

These results suggest that the enlargement of a blocking cool positive vorticity eddy, leading to more rapid westward propagation of the separated vorticity in westward-

propagation Rossby waves, might sometimes be the precursor of a major Loop Current eddy shedding event. Such enlargement can be caused by lateral mixing, trapping of separated boundary current water in evolving nonlinear critical areas, and/or quasi-geostrophic dynamics through the nonlinear omega equation.

Finally, we note that cold core, positive vorticity eddies also develop as the Loop Current interacts with the Florida shelf, and these can affect the eddy shedding process. This is reinforced by the southward advection of positive earth's vorticity. However, the ultimate source of the large cyclonic blocking gyre in the non-eddy shedding regime clearly involves the separation of the Caribbean western boundary current. The trapping of cool positive vorticity Caribbean continental shelf water north of the Loop Current plays a major role.

#### 5.4.3 Other Mechanisms

In full ocean basin simulations, with thermohaline effects not included in these GOM studies, there are other mechanisms besides bottom drag on sloping bottoms for the cool water coastal upwelling. Early work with SOMS in a flat-bottom basin patterned after the North Atlantic showed a western boundary current with cool water coastal upwelling and reverse undercurrents. The western boundary current was found to be significantly enhanced by thermodynamics.

The shelfbreak front implies a strong thermal wind consistent with observed reverse undercurrents in western boundary current regions. Such undercurrents are maintained by the supply of cool water from the polar oceans. The cool water upwells, mixes with warm surface currents, and provides energy available for deep water baroclinic instabilities after it separates from shallow shelf regions.

The cool water upwelling near western boundary currents can play a significant role in the deep water heat budget. It provides locally downward heat flux, which opposes the upward heat flux in the polar oceans that occurs with cold water formation. There can be no net vertical heat flux in an equilibrated ocean with insulated bottom (Bryan, 1987).

Potential-to-kinetic energy converting vertical heat flux must be compensated by conductive and radiative downward heat transfer. Thus, thermohaline processes in themselves probably do not give much net kinetic energy to the ocean. Indeed, because of the upward heat transport by small scales in the northern oceans, one would expect the large-scale circulation to transport heat downward and thus be indirect. This does not favor baroclinic instability being a dominant mechanism. A majority of the kinetic energy dissipation thus must be balanced by wind forcing.

Breaking internal waves can occur above the shelf, especially when a strong current occurs along the shelfbreak of a relatively broad shelf. These can produce a wide range of scales. The oscillation of steep isotherms that sometimes occurs in the present model results (Figure 28) suggests these phenomena. However, full GOM models cannot resolve the small-scale real phenomena that occur, so only resolved scales show the effects. The real phenomena would probably include significant nonhydrostatic effects.

Thus, the shelfbreak effects extend upward to the free surface. This can at least partially justify a vertical wall approximation, but the natural dynamics involve small vertical scales that should be resolved to get appropriately sharp fronts and vorticity.

Figure 26 showed a shallow instability of the Loop Current front (Day 1920), rapid northward penetration of a narrow Loop Current extension along the Florida shelfbreak starting about day 2010, and other observed Loop Current eddy shedding features. The day 2010 Loop Current extension occurred immediately after the westward propagation of the cyclonic eddy north of the Loop Current. However, it also had scale similar to the apparent baroclinic instability at day 1920, suggesting that baroclinic instability mechanisms might also be involved (Hurlburt, 1986). This relatively small scale suggests the phenomena involve higher order baroclinic modes with associated smaller Rossby radius of deformation.

## 5.5 Truncation Error Effects

Previously (see Section 3.2) we compared the Arakawa "c" grid SOMS model with the Arakawa "a" grid DieCAST model. The remarkably close comparison suggests that truncation errors are quite small, especially for the well-resolved major eddy dynamics.

Boundary current vorticity and other shelfbreak phenomena can be affected by truncation errors associated with our staircase approximation to topography. However, unlike drag effects and beta term effects, it is not clear that these lead to systematic vorticity generation. To check whether our high Reynolds number cutoff to eddy shedding is strongly influenced by such truncation errors and more clearly link the Loop Current blocking to the separation of cool positive vorticity western Caribbean continental shelf water, we did two simulations, Cases B0 and B0A (see Table 2), with a straight latitude-independent western Caribbean continental shelf. The results are similar to those with the realistic topography. Paired eddy formation also occurs with a straight latitude-independent western GOM continental shelf and results with 10 km resolution and 40 layers are similar to those with 20 km resolution and 20 layers (see Section 4).

## 6. PRELIMINARY APPLICATIONS OF DIECAST IN THE SOUTH CHINA SEA, STRAIT OF SICILY, LABRADOR CURRENT, AND GREAT LAKES

This report extensively discussed the application and validation of SOMS to the general circulation of the Gulf of Mexico and showed that DieCAST produced very similar results. This included extensive discussion of parameter and resolution sensitivity.

In the area of relocatable models, it is a complex process to set-up a numerical ocean model for any given region of the world, particularly in coastal and semi-enclosed seas. The modeler has the tedious task of manually assembling the various model components. The necessary datasets of bathymetry, wind-forcings, tides, observations, and transports exist in different formats and resolutions.

After such data are selected and extracted, they need to be interpolated to the model grid in its coordinate scheme. The model and graphics postprocessors are often run on different computer systems. Thus, it is highly desirable to have an ocean model wherein each of these steps can be easily performed within the same environment. DieCAST, in conjunction with applications developed by the MSU CAST, appears to provide both the model and environment needed to accomplish this. DieCAST facilitates this by first having a user-friendly front end for all data input. This not only helps relocatability, but also avoids having to recompile the model unless resolution parameters are changed. The model is set up to use the full arrays defined by the resolution parameters, so as not to waste storage. Second, DieCAST has an automated robust open boundary condition on the rectangular logical grid boundary defined by the resolution parameters. The lateral open boundaries and (optionally) surface layer restore toward specified values which can be derived from climatology or larger-domain models. When there is outflow, a semi-upwind approximation is automatically combined with the climatological restoring. At this point, only the normal flow on the rectangular boundary is included in the upwinding, but later more fully upwind outflow approximations are planned. All boundary conditions, including these open lateral conditions, are done with efficient clean coding that vectorizes on the boundaries by using masking arrays. It should be noted that the model uses centered differencing at all interior points. Third, all DieCAST plotting and animation is performed by postprocessors, including interactive previewing each plot with options for postscript hardcopy generation. Fourth, DieCAST does not require any topography filter, thus avoiding the aggravating compromise between accuracy and numerical stability required by other models. And, finally DieCAST is being fully integrated into the total CAST data base management, graphics, and model evaluation environment. We now show "first cut" applications of DieCAST to other geographical areas of the globe.

### 6.1 South China Sea

A closed basin approximation, forced by climatological annual average winds and 30-day restoring to surface temperature and salinity climatology, is used in this "first cut" simulation shown in Figure 30. Initial conditions are also from Levitus climatology. Unfiltered realistic topography was used with 1/6 degree lateral resolution and 10 layers. A "first cut" run with lateral diffusivities of 100 m<sup>2</sup>/sec is compared to an almost identical twin run with diffusivities reduced to 10 m<sup>2</sup>/sec being the only change. This work was done in cooperation of Dr. Le Ngoc Ly of the Naval Postgraduate School.

### 6.2 Labrador Current

"First cut" results from applications to a northeastern section of the North Atlantic Ocean using 1/4 degree resolution and 20 layers are shown in Figure 31. This included restoring to surface climatology and the general open boundary condition. This work was done in cooperation of Dr. Richard Greatbatch of Dalhousie University.

### 6.3 Strait of Sicily

A rectangular Mediterranean region including the Strait of Sicily was simulated using 1/12 degree resolution and 10 layers as shown in Figure 32. This included initial and open boundary stratification patterned after climatology. A "first cut" run with lateral diffusivities of 100 m<sup>2</sup>/sec showed greatly decreased eddy activity and 30 percent smaller maximum velocity compared to an almost identical twin run with diffusivities reduced to 10 m<sup>2</sup>/sec. The larger diffusivity also eliminated a significant cross-strait current which separated from the western side of the Strait. This work is being done in collaboration with Dr. George Heburn of the Naval Research Laboratory.

### 6.4 Great Lakes

The modeling of Lake Erie (Figure 33) is being done in collaboration with Dr. William O'Connor of the Great Lakes Environmental Research Laboratory. Dr. O'Connor has also modeled Lake Michigan as shown in Figure 34.

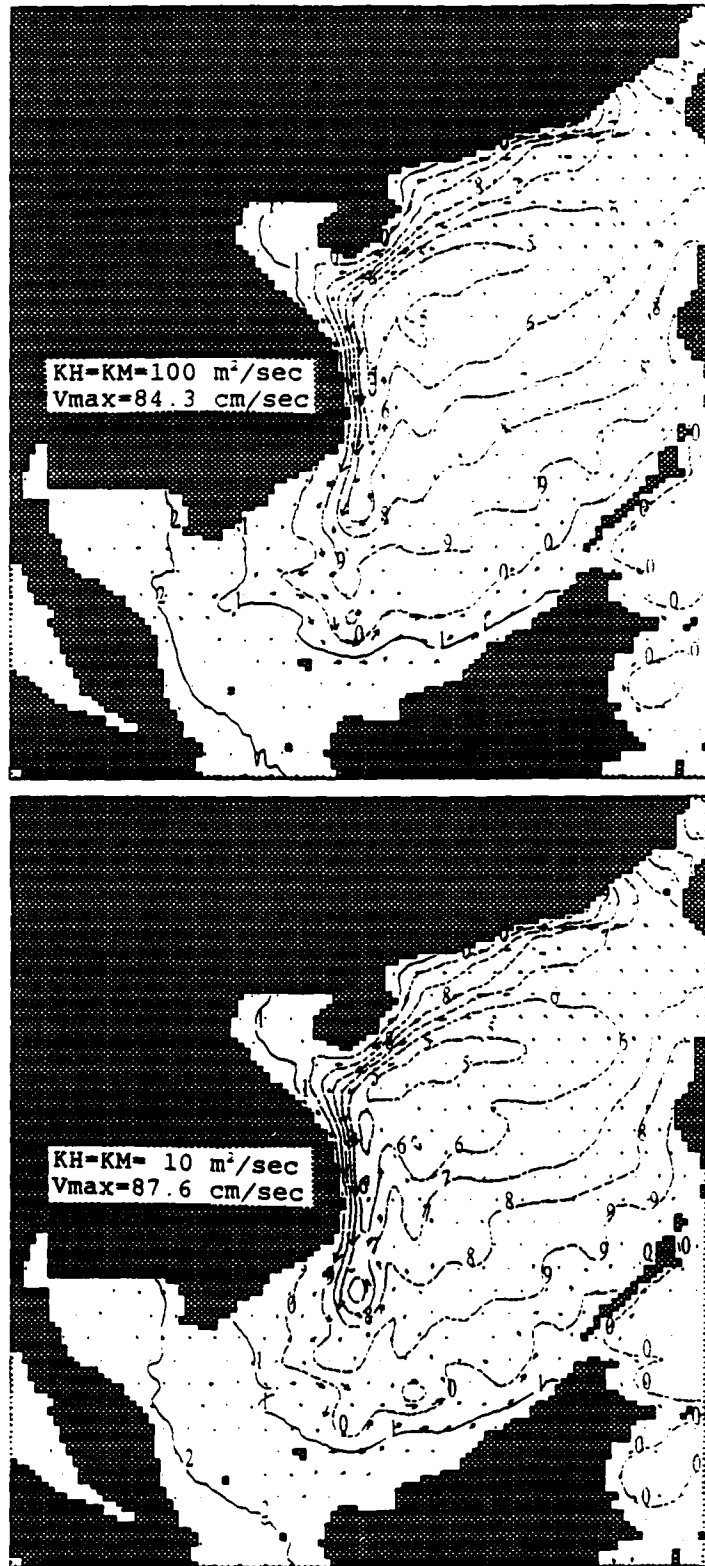


Figure 30. South China Sea. Day 360 top layer (depth = 10 m) velocity and pressure from first cut simulation. Climatological annual average wind stress is used, with 30-day restoring to surface temperature and salinity. Maximum velocity = 84.4 cm/sec.

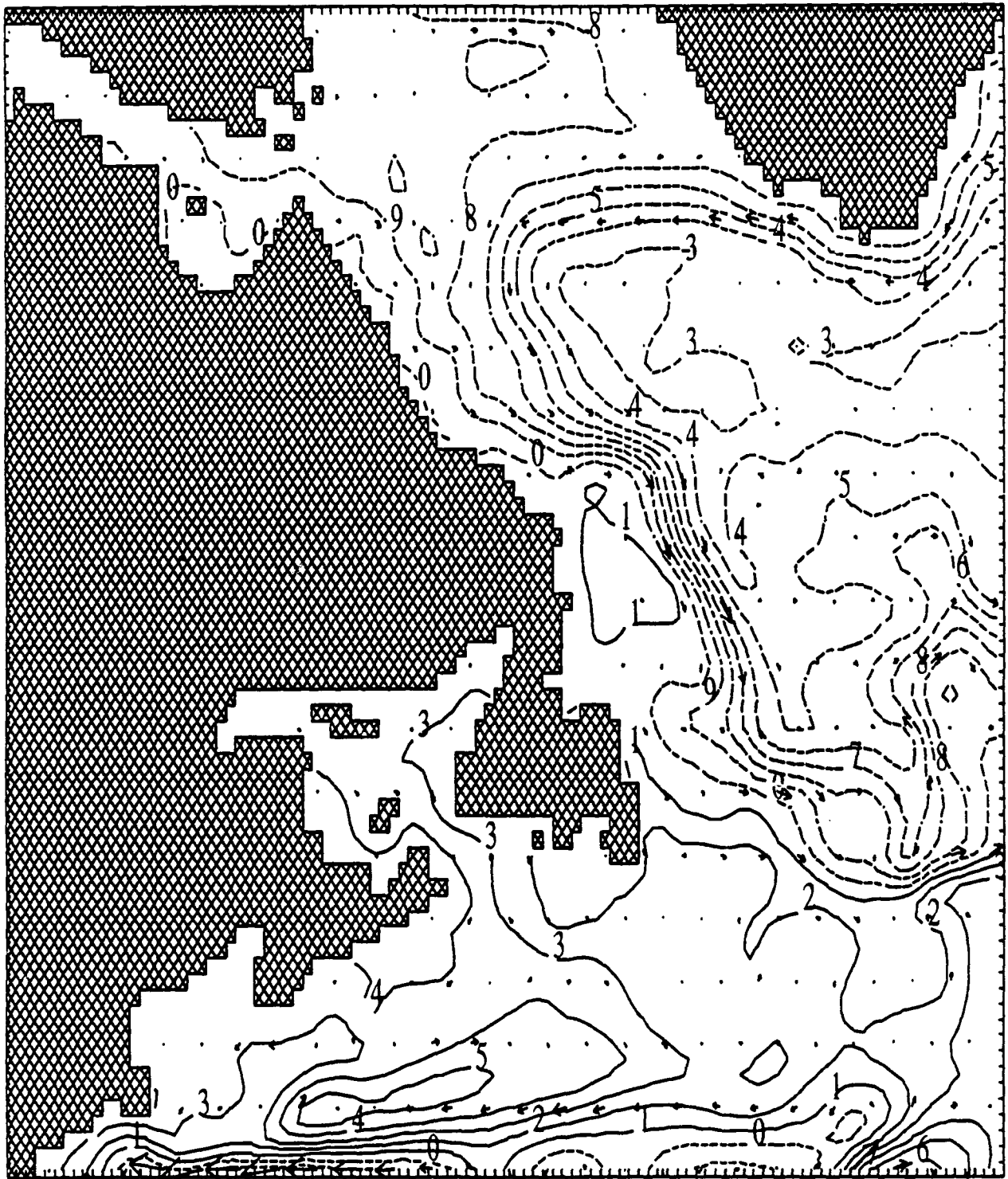


Figure 31. Labrador Current. Day 1080 top layer (depth = 20 m) velocity and pressure from first cut simulation. Climatological annual average wind stress is used, with 30-day restoring to climatological surface temperature and salinity. Open lateral boundaries restore to climate at inflows and use modified upwind for outflows. Maximum velocity = 70.2 cm/sec.

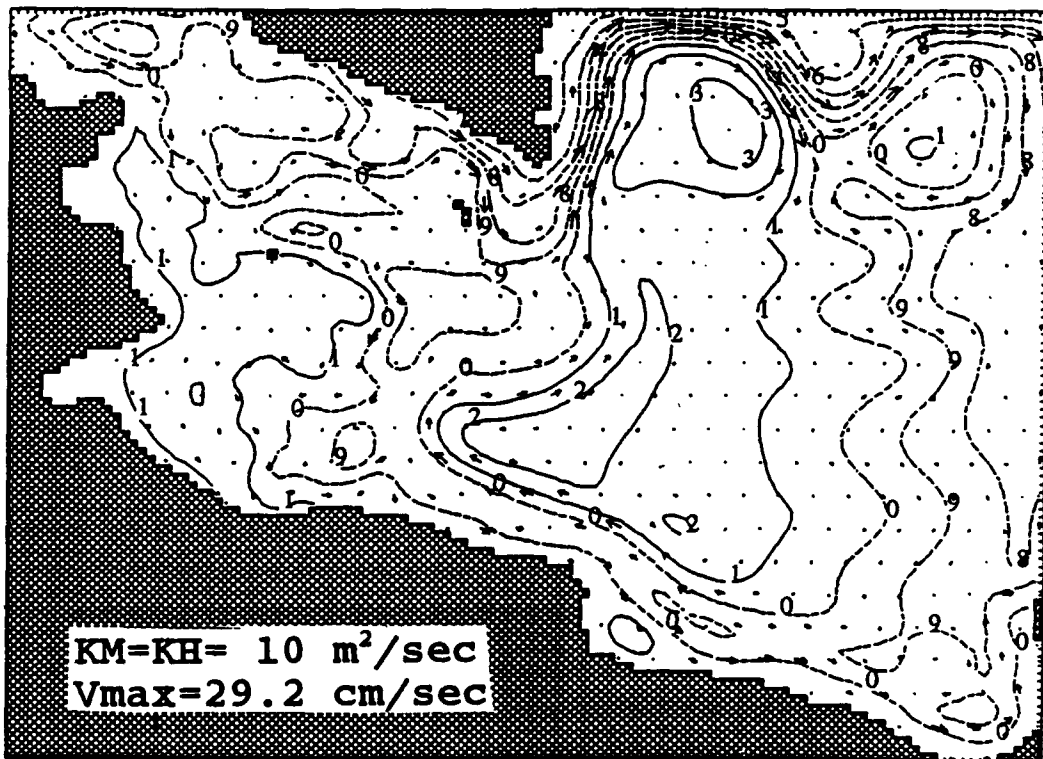
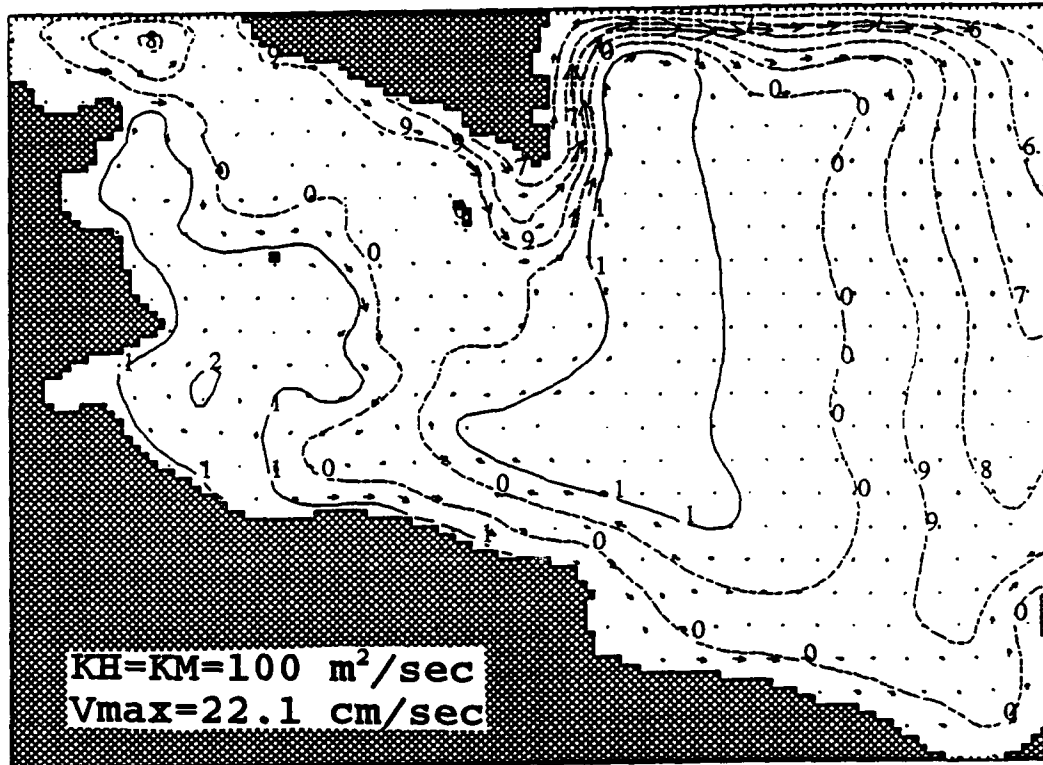


Figure 32. Strait of Sicily. Day 360 top layer (depth = 20 m) velocity and pressure from first cut simulations. Open boundary conditions include reverse undercurrents.

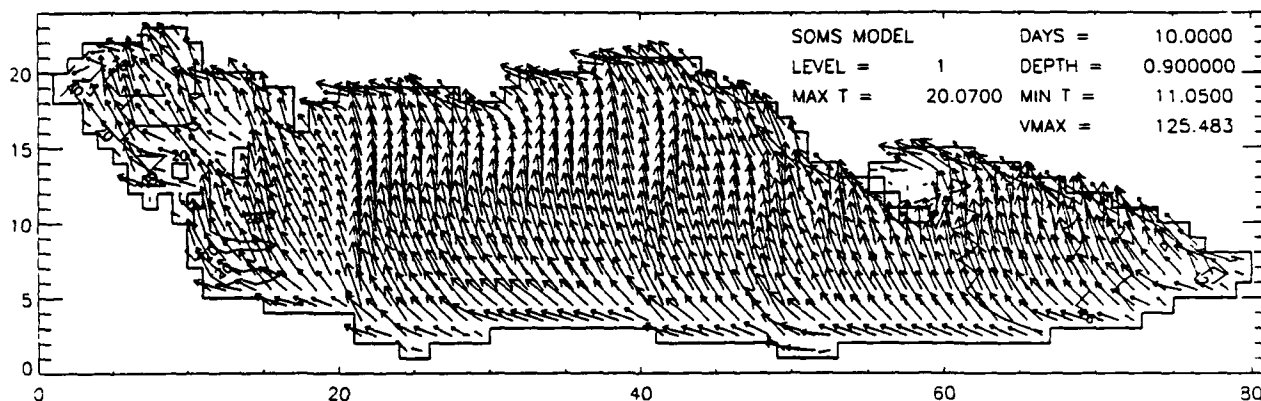


Figure 33. Lake Erie. Top layer (depth = 0.9 m) flow resulting from strong wind event. Vertical mixing is limited by strong stratification.

## 7. CONCLUDING REMARKS

Shelf resolving GOM studies reveal significant, complex interaction between shelf and deep water flows that are addressable only by high resolution fully nonlinear numerical models. Our SOMS and DieCAST results have been validated extensively by observations, theory, and previous model results.

This interaction should be investigated in more detail, including the different physical effects as indicated by term balances in the vorticity equation and quasi-geostrophic omega equation. This is a substantial undertaking in view of the possible major roles of fronts, breaking internal waves, and nonlinear critical areas. While easy to evaluate local advection, it is difficult to evaluate the advection of a dynamic, evolving feature that interacts with the advecting background flows, for which appropriate values are difficult to determine. The finite differencing of the omega equation itself requires great care to make it correspond to the finite difference equations used, and requires a 3-D elliptic solver in general geometry. Even then, it is only an approximation to the equations used. Thus, detailed analysis is truly a major effort.

Herein, we include many confirmations of the model results, all from a single run (Case B3) forced only by specified Caribbean inflows based on annual average observations. The spatial distribution of rms sea surface height deviation, from its time average in the model, agrees with satellite data in both the amplitudes and locations of the primary and

secondary centers of transient eddy activity. The mean thermocline, vertical density profile, and vertical empirical orthogonal functions are in close agreement with those derived from observations. The average Loop Current eddy shedding period is about 254 days in the model compared to 259 days observed in the GOM. The shed eddy size, phase speed, dispersion rate, and vorticity are close to observations and theory. The location, amplitude, and development time for paired cyclonic eddies near the western GOM shelfbreak are similar to observations. Loop Current and shed eddy structures reflect observations in remarkable detail, including scale height, cool pool near surface, and a small-scale vertically coherent kink under separated western Caribbean boundary current water. A small-scale cool core eddy occurs along the Florida shelfbreak just before eddy shedding in both model and observations. Small-scale eddies/waves develop and propagate along the Loop Current front as in observations and previous model results. Rapid northward penetration of a narrow Loop Current extension occurs along the Florida shelfbreak after eddy shedding.

These confirmations support the credibility of SOMS and DieCAST. Notably, they occur without assimilating any time dependent observations or initial conditions into the model, and clearly demonstrate the model's dynamic similarity to the GOM, even when using resolution permitted on modern workstations. Such dynamic similarity is needed for success not only in independently addressing general circulation features, but

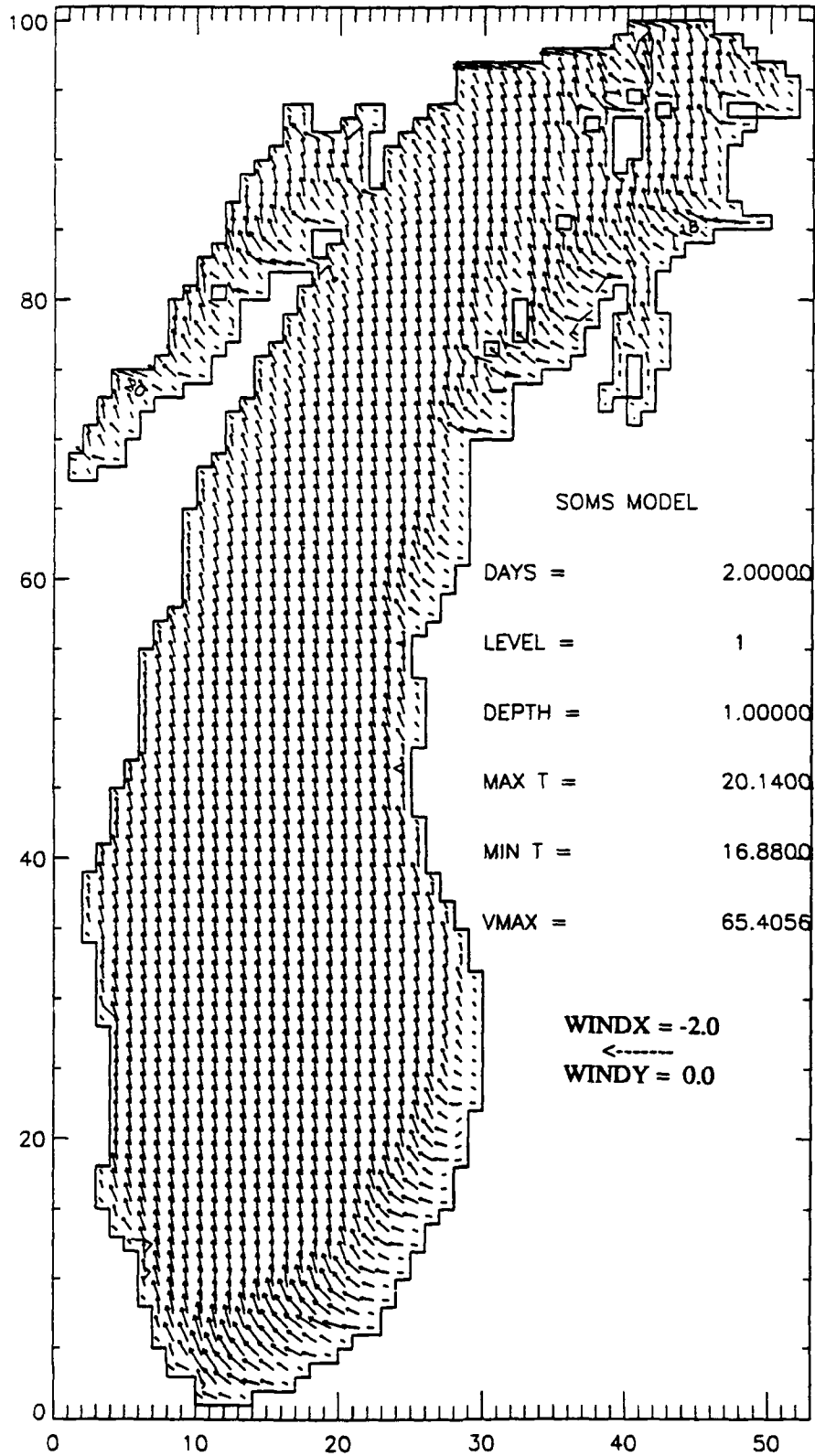


Figure 34. Lake Michigan. Top Layer (depth = 1.0 m) flow resulting from strong wind event.

also in coupled atmosphere/ocean nowcast/forecast applications that assimilate real data as it becomes available. This dynamic similarity is as important as using advanced data assimilation schemes.

As demonstrated by diffusion and other parameter sensitivity studies, such dynamic similarity is possible because of the model's robustness with realistically low dissipation. Also, the special dominant term treatment used by SOMS and DieCAST allows dynamic similarity with lower resolution than conventional treatments.

In the future, to increase accuracy and efficiency in modeling shelf processes, an attractive approach would be to use special shelf region models with lateral boundary fitted coordinates that have extra high resolution normal to the shelfbreak. This should be most beneficial to sigma coordinate models, by greatly improving horizontal density gradient approximation near shelfbreaks. Also, more accurate description of the shelf region bottom boundary layer is desirable. To efficiently resolve the bottom boundary layer, a sigma coordinate system (Blumberg and Mellor, 1987) or a thin shell bottom boundary layer submodel (Dietrich, et al, 1987) could be used. In either approach, a turbulence closure scheme such as the Mellor-Yamada level 2.5 scheme should be included in the shelf region model. Such shelf model, properly coupled to a deep water model, would accurately and efficiently address important shelf processes such as those affecting the dynamics of paired eddies in the western GOM, and the Caribbean western boundary current separation near the Yucatan Strait.

## APPENDIX I

### APPROACH TO CONTOURING GRAPHICS

Our contour plots use computer-automated one-digit semi-random contour labeling. Such one-digit labeling is useful when showing plots with detailed structures. Contour levels are given mod(10) so that an arbitrary number of levels can be labeled. For example, the 25°C temperature contour is labeled with a "5". Negative contours are dashed. When a contour segment passes

sufficiently close to a cell center, and there are no other contours in the cell and no contour labels in a user-specified neighborhood, we draw the contour label instead of the segment. The gap in the contour thus shows the contour to which the label belongs. This approach allows automatic, unambiguous, space-saving and unobtrusive (not clashing with nearby contours) contour labeling. In some plots, the contours drawn are distributed uniformly between the field maximum and minimum. In others, including temperature, the contours are chosen specially to show round-number characteristic values of the field, as is often done with published observations; observations generally show the location of the 15 or 20 degree isotherm rather than fractional values such as 17.216. Temperature contour labels are given by:

$$N = \text{MOD}(T, 10)$$

where T has units °C. Again there is no ambiguity, because top level temperature is always between 20°C and 30°C.

Pressure is converted hydrostatically to equivalent free surface height anomaly in centimeters, because the latter is closely related to satellite measurements. Pressure contours are labeled by single digit integers, whose formula is:

$$N = \text{MOD}[(P + 50)/5, 10]$$

where P is the free surface anomaly. Thus, the contour interval is 5 cm and  $N = 6$  for  $P = -20$  or for  $P = 30$ . This leaves no ambiguity, because the contours are also dashed for negative P.

Vorticity contour labeling is similar for P except its units are per week. Thus, a vorticity value of 4 pi (12.5664) corresponds to one rotation per week. For a value of 10, its contour label would be "2".

## APPENDIX II

### LINEAR EQUATION OF STATE

For sufficiently small ranges of temperature (T) and salinity (S), the following linear equation for density (D) is a good approximation:

$$D = D_0 + A*(S-S_0) + B*(T-T_0) \quad (1)$$

where A and B are constants, and D0 is the reference state density (when S = S0 and T = T0).

Then:

$$\begin{aligned} dD/dt &= (\partial D/\partial S)*dS/dt + (\partial D/\partial T)*dT/dt \\ &= A*dS/dt + B*dT/dt \\ &= \nabla \cdot K_S \nabla (A*S) + \nabla \cdot K_T \nabla (B*T) \end{aligned} \quad (2)$$

where  $K_S$  and  $K_T$  are turbulent diffusivities of S and T.

If  $K_S$  and  $K_T$  are roughly equal, then:

$$\begin{aligned} dD/dt &= \nabla \cdot [K \nabla (A*S + B*T)] = \nabla \cdot [K \nabla D] \\ \text{where } K &= K_S = K_T \end{aligned} \quad (3)$$

It follows that a separate transport equation for salinity is dynamically redundant, if the range of S and T experienced by typical fluid material elements is small (during typical GOM eddy life cycles). The excellent agreement of DieCAST with GOM observations, while using a linear relation for density as a function of T, only confirms this approximation.

More intuitively, a typical fluid element entering the GOM experiences a relatively small range of density, temperature, and salinity during its residence time compared to the existing variations and its incoming fluid. Thus, interior density is accurately determined by incoming fluid density. It follows that salinity is dynamically redundant in the GOM. Thus, we assume a linear equation of state and parameterize salinity effects on density into the temperature field.

#### ACKNOWLEDGEMENTS

We are indebted to the advice and support of Paul Martin, Harley Hurlburt, J. Dana Thompson, Steve Piacsek, Aaron Lai, Alan Wallcraft, Jeff Hawkins, Chris Mooers, and Tom Warn. We also appreciate the extensive effort and long hours spent by MSU's Evelyn Lott in preparing this manuscript. This research was supported by the Office of Naval Research's Navy Ocean Modeling and Prediction Program under Cooperative Agreement N00014-90-CA-0001

with the Institute for Naval Oceanography and Research Grant N00014-92-J-4109 with Mississippi State University.

#### REFERENCES

Asselin, R. (1972). Frequency Filter for Time Integrations. Mon. Weather Rev., 7, 187-190.

Blumberg, A.F. and G.L. Mellor (1987). A Description of A Three-Dimensional Ocean Circulation Model in Three Dimensional Coastal Ocean Models, N.S. Heaps (ed.), 1-16. American Geophysical Union, Washington, DC.

Brooks, D.A. and F.J. Kelly (1986). The Interaction of a Loop Current Ring with the Continental Shelf in the Western Gulf of Mexico. Proceedings of the Seventh Annual Gulf of Mexico Information Transfer Meeting, New Orleans, LA, November 4-6, 1986. OCS Study/MMS Report 87-0058, 255-300.

Bryan, F. (1987). Parameter Sensitivity of Primitive Equation Ocean General Circulation Models. J. Phys. Oceanogr., 17, 970-985.

Cooper, C. and J.D. Thompson (1989a). Hurricane-Generated Currents on the Outer Continental Shelf, 1, Model Formulation and Verification. J. Geophys. Res., 94, 12513-12539.

Cooper, C. and J.D. Thompson (1989b). Hurricane-Generated Currents on the Outer Continental Shelf 2, Model Sensitivity Studies. J. Geophys. Res., 94, 12540-12554.

Dietrich, D.E., M.G. Marietta, and P.J. Roache (1987). An Ocean Modelling System with Turbulent Boundary Layers and Topography: Numerical Description. Int. J. Num. Methods in Fluids, 7, 833-855.

Dietrich, D.E., P.J. Roache, and M.G. Marietta (1990). Convergence Studies with the Sandia Ocean Modeling System. Int. J. Num. Methods in Fluids, 11, 127-150.

Dietrich, D.E. (1992). The Sandia Ocean Modeling System. Programmers Guide and Users Manual, SAND92-7286. Sandia National Laboratories, Albuquerque, NM 87185.

- Dietrich, D.E. (1993). On Modeling Geophysical Flows having low Rossby Numbers. Atmosphere/Ocean, 31, 57-71.
- Dietrich, D.E. and C.A. Lin (1993). Numerical Studies of the Gulf of Mexico Circulation. Part 1: Eddy Shedding. Accepted J. Geophys. Res.
- Dukowicz, J.K. and R.C. Malone (1992). Parallel Ocean General Circulation Modeling, Report LA-UR-92-200 Los Alamos National Laboratories, Los Alamos, NM 87545.
- Elliott, B.A. (1982). Anticyclonic Rings in the Gulf of Mexico. J. Phys. Oceanogr., 12, 1292-1309.
- Farristall, G.Z., K.J. Schaudt and C.K. Cooper (1992). Evolution and Kinematics of a Loop Current Eddy in the Gulf of Mexico During 1985. J. Geophys. Res., 97, 2173-2184.
- Gawarkiewicz, G. and D.C. Chapman (1991). Formation and Maintenance of Shelfbreak Fronts in an Unstratified Flow. J. Phys. Oceanogr., 21, 1225-1239.
- Hamilton, P. (1992). Personal Communication
- Hurlburt, H.E. and J.D. Thompson (1980). A Numerical Study of Loop Current Intrusions and Eddy Shedding. J. Phys. Oceanogr., 10, 1611-1651.
- Hurlburt, H.E. and J.D. Thompson (1982). The Dynamics of the Loop Current and Shed Eddies in a Numerical Model of the Gulf of Mexico. Hydrodynamics of Semi-Enclosed Seas, J.C.J. Nihoul (ed.) Elsevier Scientific Publishing Company, Amsterdam.
- Hurlburt, H.E. (1984). The Potential for Ocean Prediction and the Role of Altimeter Data. Marine Geodesy, 8, 17-66.
- Hurlburt, H.E. (1986). Dynamic Transfer of Simulated Altimeter Data into Subsurface Information by a Numerical Ocean Model. J. Geophys. Res., 91, 2372-2400.
- Kirwan, A.D. and J.K. Lewis (1987). Genesis of a Gulf of Mexico Ring as Determined from Kinematic Analysis. J. Geophys. Res., 92, 11727-11740.
- Ko, D.-S. (1992) Synthetic Temperature Profiles in the Gulf of Mexico: Part 1. Statistical Relationship between Modal Amplitudes and Dynamic Height at Surface. Institute for Naval Oceanography Report TM-8, May 1992.
- McWilliams, J.C., and G.R. Flierl (1979). On The Evolution of Isolated, Nonlinear Vortices. J. Phys. Oceanogr., 1155-1182.
- Mellor, G.L., and T. Yamada (1982). Development of a Turbulence Closure Model for Geophysical Fluid Problems. Rev. Geophys. Space Phys., 20, 851-875.
- Merrell, W.J. and J.M. Morrison (1981). On the Circulation of the Western Gulf of Mexico with Observations from April 1978. J. Geophys. Res., 86, 4181-4185.
- Peggion, G. (1984). The Effects of the Benthic Boundary Layer on the Physics of Intense Mesoscale Eddies. Mesoscale Air-Sea Interaction Group Technical Report Florida State University, Tallahassee, FL.
- Roache, P.J. and D.E. Dietrich (1988). Evaluation of the Filtered Leapfrog-Trapezoidal Time Integration Method. Numer. Heat Transfer, 14, 149-164.
- Roache, P.J. (1976). Computational Fluid Dynamics. Hermosa Publishers, Albuquerque, NM.
- Schmitz, W.J. and P.L. Richardson (1991). On the Sources of the Florida Current. Deep-Sea Research, 38, S379-S409.
- Smith, D.C., IV and J.J. O'Brien (1983). The Interaction of a Two-Layer Isolated Mesoscale Eddy with Bottom Topography. J. Phys. Oceanogr., 13, 1681-1697.
- Sturges, W. and S. Welsh (1991). Numerical Modeling Studies of the Gulf of Mexico and the Caribbean Sea Using The Bryan-Cox Model. MMS Report 91-0061.

Vidal, M.V., F.V. Vidal, and J.M. Perez-Molero (1992). Collision of a Loop Current Anticyclone Ring against the Continental Shelf in the Western Gulf of Mexico. J. Geophys. Res., 94, 2155-2172.

Vukovich, F.M. and B.W. Crissman (1986). Aspects of Warm Rings in the Gulf of Mexico. J. Geophys. Res., 91, 2645-2660.

Warn, T. (1992). Personal Communication.

Zuur, E.A.H. and D.E. Dietrich (1990). The SOMS Model and its Application to Lake Neuchatel. Aquatic Sci., 52, 115-129.

# REPORT DOCUMENTATION PAGE

Form Approved  
OMB No. 0704-0188

Public reporting burden for this collection of information is estimated to average 1 hour per response, including the time for reviewing instructions, searching existing data sources, gathering and maintaining the data needed, and completing and reviewing the collection of information. Send comments regarding this burden estimate or any other aspect of this collection of information, including suggestions for reducing this burden, to Washington Headquarters Services, Directorate for Information Operations and Reports, 1215 Jefferson Davis Highway, Suite 1204, Arlington, VA 22202-4302, and to the Office of Management and Budget, Paperwork Reduction Project (0704-0188), Washington, DC 20503.

1. Agency Use Only (Leave blank).	2. Report Date. 1 JULY 1993	3. Report Type and Dates Covered. TECHNICAL REPORT	
4. Title and Subtitle. ON THE APPLICATION AND EVALUATION OF THE RELOCATABLE DIECAST OCEAN CIRCULATION MODEL IN COASTAL AND SEMI-ENCLOSED SEAS		5. Funding Numbers.  Program Element No.  Project No.  Task No.  Accession No.	
6. Author(s). David E. Dietrich Dong-Shan Ko Lanny A. Yeske		7. Performing Organization Name(s) and Address(es).  Mississippi State University Center for Air Sea Technology (CAST) Stennis Space Center, MS 39529-6000	
8. Performing Organization Report Number.  CAST Technical Report 93-1		9. Sponsoring/Monitoring Agency Name(s) and Address(es).  Office of Naval Research 800 North Quincy Street Code 1242 Arlington, VA 22217-5000	
10. Sponsoring/Monitoring Agency Report Number.  Report 93-1		11. Supplementary Notes.  Research performed under Office of Naval Research Contract/Grant No. N00014-92-J-4109/ Office of Naval Research Cooperative Agreement N00014-90-CA-0001.	
12a. Distribution/Availability Statement.  Approved for public release; distribution is unlimited		12b. Distribution Code.	
13. Abstract (Maximum 200 words).  To improve coastal and semi-enclosed seas modeling, a new DieCAST Ocean Model has been developed. In application to the Gulf of Mexico (GOM), this model gives remarkably similar results to that obtained from the Sandia Ocean Model System (SOMS) and at a computational speed much faster than SOMS or other ocean models presently available. The results are supported by many GOM observations including GEOSAT rms sea-surface-height anomaly data; mean thermocline and empirical orthogonal functions; the evolution of vortex pairs in the western GOM; major Loop Current eddy shedding period; shed eddy size, phase speed, dispersion rate and vorticity; and detailed Loop Current and shed eddy structure. Finally, and a major advantage of DieCAST is its capability to be easily relocated to any geographical region of the globe. Preliminary applications in several regions such as the Mediterranean, South China Sea, Great Lakes, and Labrador Current are described.			
14. Subject Terms. (U) DieCAST      (U) Model      (U) Relocatable      (U) CAST  (U) Ocean      (U) Application      (U) Evaluation      (U) Coastal		15. Number of Pages. 79	
16. Price Code.		17. Security Classification of Report. UNCLASSIFIED	
18. Security Classification of This Page. UNCLASSIFIED		19. Security Classification of Abstract. UNCLASSIFIED	
20. Limitation of Abstract.			

DISTRIBUTION LIST

Office of Naval Research  
800 North Quincy Street  
Arlington, VA 22217-5000

Arthur Bisson  
Alan Brandt  
Ed Chaika  
Thomas Curtin  
David Evans  
Robert Feden  
Emanuel Fiadeiro  
Gary Geernaert  
Thomas Kinder  
Mark Kurzius  
Robert Peloquin (3)  
Alan Weinstein

Administrative Grants Officer  
Office of Naval Research  
Resident Representative N66020  
Administrative Contracting Officer  
Georgia Institute of Technology  
206 O'Keefe Building  
Atlanta, GA 30332-0490

Defense Technical Info Center (2)  
Building 5, Cameron Station  
Alexandria, VA 22304-65145

Naval Research Laboratory  
4555 Overlook Avenue, SW  
Washington, DC 20375-5000  
Timothy Coffey  
Paul Gaffney  
Eric Hartwig

Naval Research Laboratory  
Building 1103, Room 248  
Stennis Space Center, MS 39529  
Budd Adams  
Rick Allard  
Herb Eppert  
Ed Franchi  
Patrick Gallacher  
John Harding  
George Heburn  
Harley Hurlburt  
Don Johnson  
Edward Johnson  
John Kindle  
Paul Martin  
Joe McCaffrey

William Mosely  
Steve Piacsek  
Ruth Prellor  
Kim Saunders

Naval Research Laboratory  
Monterey, CA 93943-5006  
Ed Barker  
John Hovermale

Don Durham  
Naval Oceanography Command  
Building 1020  
Stennis Space Center, MS 39529

Fleet Numerical Oceanography Center  
Monterey, CA 93943  
Mike Clancy  
Jim Cummings  
Robert Plante

Naval Oceanographic Office  
Stennis Space Center, MS 39529  
Landry Bernard  
Michael Carron  
Steve Haeger  
Martha Head  
Charles Horton  
Andrew Johnson  
David Martin

Naval Postgraduate School  
Monterey, CA 93943  
Mary Batteen  
Robert Bourke  
Ching-Sang Chiu  
Peter Chu  
Curt Collins  
Robert Haney  
Le Ngoc Ly  
Albert Semtner  
Edward Thornton

A.D. Kirwan  
Dept. of Oceanography  
Old Dominion University  
Norfolk, VA 23529-0276

George L. Mellor  
Princeton University  
P.O. Box CN710  
Princeton, NJ 08544

Kirk Bryan  
Princeton University  
P.O. Box 318  
Princeton, NJ 08540

Tal Ezer  
Princeton University  
P.O. Box 308  
Princeton, NJ 08540

John Apel  
Applied Physics Laboratory  
Johns Hopkins University  
Laurel, MD 20723

Woods Hole Oceanographic Institution  
Woods Hole, MA 02543  
Bob Beardsley  
Ken Brink  
Dave Chapman  
Steve Lentz  
William Schmitz

Allan R. Robinson  
Harvard University  
29 Oxford Street, Room 100D  
Cambridge, MA 02138

Massachusetts Institute of Technology  
Department of Earth, Atmospheric  
and Planetary Science  
Cambridge, MA 02139  
Paola Rizzoli  
Carl Wunsch

Ron McPherson  
National Meteorological Center  
5200 Auth Road  
Camp Springs, MD 20746

Minerals Management Service  
381 Elden Street  
Herndon, VA 22070-4817  
Bob Labelle  
Theresa Paluszkiwz

John Overland  
NOAA Office of Ocean and Atmospheric  
Research  
Seattle, WA 98115

Oregon State University  
Department of Oceanography  
Corvallis, OR 97331-2849  
John Allen  
Andrew Bennett  
Bob Holman  
Alberto Mestez-Nunez

John Bane  
University of North Carolina  
Venable Hall 045-A  
Chapel Hill, NC 27514

Robert Barry  
Ball Aerospace  
Mail Code RA2  
Boulder, CO 80306

Dong-Ping Wang  
State University of New York  
Stony Brook, NY 11794

University of Miami  
4600 Rickenbacker Causeway  
Miami, FL 33149-1098  
Otis Brown  
Dong-Shan Ko  
Christopher Mooers

Scripps Institute of Oceanography  
LaJolla, CA 92093  
L. Cheng  
Robert Guza  
Peter Niiler  
Richard Sommerville  
Clint Winant

Jay McCreary  
NOVA University  
Dania, FL 33004

Roger Bauer  
Compass System, Inc.  
4640 Jewell Street, #204  
San Diego, CA 92109

Donna Blake  
Division of Atmospheric  
Science Programs  
National Science Foundation  
1800 G Street, NW  
Washington, DC 20550

Lakshmi Kantha  
University of Colorado  
Campus Box 431  
Boulder, CO 80309-0431

Rutgers University  
P.O. Box 231  
New Brunswick, NJ 08903-0231  
Scott Glenn  
Dale Haidvogel

Texas A&M University  
Dept. of Oceanography  
College State, TX 77843  
David Brooks  
Robert Reid

Murray Brown  
Minerals Management Services  
1201 Elmwood Park Blvd.  
New Orleans, LA 70123-2394

J.F. Bennett  
Minerals Management Service  
310 Eldon Street  
Herndon, VA 22070-4817

Arthur Cosby  
Director, Centers and Institutes  
P.O. Box 6343  
Mississippi State, MS 39762

Lynne Chronister  
Sponsored Programs Administration  
P.O. Box 6156  
Mississippi State, MS 39762

Joe Thompson  
Engineering Research Center  
P.O. Drawer 6176  
Mississippi State, MS 30762

University of Southern Mississippi  
Building 1103  
Stennis Space Center, MS 39529  
Ranjit Passi  
Germana Peggion  
Louise Perkins  
Robert Willems

Markku Santala  
Exxon Production Research Co.  
P.O. Box 2189  
Houston, TX 77252-2189

John Leese  
Department of Meteorology  
University of Maryland  
College Park, MD 30742

James Lewis  
Atlantic Applied Research Corp.  
207 S. Seashore Avenue  
Long Beach, MS 39560

Florida State University  
MS B-174, 012 LOV  
Tallahassee, FL 32306-3041

Mark Luther  
James J. O'Brien  
Tony Sturges  
Mark Weatherly

Sandia National Laboratory  
Albuquerque, NM 87185  
Bill Camp  
Margaret Chu  
Julio Swisthelm

William O'Connor  
NOAA Great Lakes  
Environmental Research Laboratory  
2205 Commonwealth Boulevard  
Ann Arbor, MI 48105

William Schramm  
NOAA Center for Ocean Analysis  
and Prediction  
2560 Garden Road  
Monterey, CA 93940

National Center for Atm Research  
P.O. Box 3000  
Boulder, CO 80303  
William Holland  
Stephen Schneider  
Wayne Shiver  
Warren Washington

Robert Winokur  
Oceanographer of the Navy  
Naval Observatory  
34th & Massachusetts Avenue NW  
Washington, DC 20390

Alan Blumberg  
Hydro-Qual, Inc.  
1 Lethbridge Plaza  
Mahway, NH 07430

Tony Dalrymple  
Center for Applied Coastal Research  
University of Delaware  
Newark, DE 19716

Ed Harrison  
SPAWARS  
National Center 1, Room 3E90  
Arlington, VA 22202

Peter Ranelli  
SPAWARS 165  
5 Crystal Park, Room 301  
Arlington, VA 22202

D.J. LaVoy  
Requirements/Assessment Branch  
Expeditionary Warfare Division  
Code N858, Pentagon Room 4A720  
Washington, DC 20350-2000

Lie-Yauw Oey  
Dept. of Civil Engineering  
Stevens Institute of Technology  
Hoboken, NJ 07030

Los Alamos National Laboratory  
Los Alamos, NM 87545  
Sumner Barr  
Chick Keller  
Aaron Lai

Frank Schatzle  
Gulf Weather Corporation  
Building 1103  
Stennis Space Center, MS 39529

R.F. Beyer  
Bettis Atomic Power Laboratory  
P.O. Box 79  
West Hifflin, PA 15122

J.R. Bates  
Goddard Space Flight Center  
Data Assimilation Office  
Greenbelt, MD 20771

R.L. Watters  
Department of Energy Office of  
Health and Environmental Research  
Washington, DC 20545

R. Dyer  
Environmental Protection Agency  
AW-458 Waterside Mall East  
Washington, DC 20545

Environmental Protection Agency  
Building 1103  
Stennis Space Center, MS 39529  
Fred Kopfler  
Douglas Lipka

Waterways Experiment Station  
Coastal Engineering Research Center  
P.O. Box 631  
Vicksburg, MS 39180  
Norman Scheffner  
Martin Miller  
Robert Bernard

Malcolm Spaulding  
Applied Sciences Associates  
70 Dean Knauss Drive  
Narragansett, RI 02882-1143

Dave Peters  
Conoco Incorporated  
600 N. Ashford  
P.O. Box 2197  
Houston, TX 77252

Patrick Roache  
Ecodynamics  
P.O. Box 9229  
Albuquerque, NM 87119

Curt Coney  
Lawrence Livermore Laboratory  
Program for Climate Model  
Diagnosis & Intercomparison  
Livermore, CA 94550

Lawrence Livermore Laboratory  
P.O. Box 808  
Livermore, CA 94550  
Phil Gresho  
Mike McCracken

Ken Schaudt  
Marathon Oil Company  
Operations and Construction  
P.O. Box 3128  
Houston, TX 77253

David Szabo  
Mobil Research & Development Corp.  
Offshore Engineering  
13777 Midwam Road  
Farmers Branch, TX 75234

Abe Cheng  
Sverdrup Technology, Inc.  
Stennis Space Center, MS 39529

George Forristal  
Shell Development Company  
P.O. Box 481  
Houston, TX 77001

Stephen Murray  
Louisiana State University  
Coastal Studies Institute  
Baton Rouge, LA 70803-7527

Antonio Baptista  
Oregon Graduate Institute  
19600 NW Von Neumann Drive  
Beaverton, OR 97006

Robert Whitaker  
Texas A&M University  
P.O. Box 1675  
Galveston, TX 77553

Peter Sheng  
University of Florida  
336 Weil Hall  
Gainesville, FL 32611

Joannes Westerink  
University of Notre Dame  
Department of Civil Engineering  
Notre Dame, IN 46117

University of Rhode Island  
Department of Oceanography  
Kingston, RI 02881  
Peter Cornillon  
Thomas Rossby

Roger Pielke  
University of Virginia  
Dept. of Environmental Sciences  
Charlottesville, VA 22903

G.R. Heath  
University of Washington  
Department of Oceanography  
Seattle, WA 98195

Roland Byron-Scott  
13 Penfold Street  
Bedford Park, 5042  
South Australia, Australia

Canadian Climate Center  
4905 Dufferin Street  
Downsview, Ontario  
M3H 5T4 CANADA  
George Boer  
Robert Daly  
Norm McFarland

Institute of Ocean Sciences  
9860 W. Saanich Road  
Sidney, British Columbia  
V8L 4B2 CANADA  
Joseph Chernlowky  
Bill Crawford  
Greg Holland

Richard Greatbach  
Department of Physics  
Memorial University  
St. Johns, Newfoundland  
A1B 3X7 CANADA

McGill University  
Department of Atmospheric Sciences  
805 Sherbrooke Street West  
Montreal, Quebec  
CANADA H3A 2K6  
Jacques Derome  
Charles Lin

Michael Beland  
RPN-2121 Trans Canada Highway  
Dorval, Quebec  
CANADA H9P 1J3

Greg Holloway  
Institute of Ocean Science  
P.O. Box 6000  
Sidney, BC  
V81 4B2 CANADA

Alan Davies  
Proutman Ocean Laboratory  
Bidston Observatory  
Birkenhead, Morseyside  
L437RA UNITED KINGDOM

Eche Mittelstaedt  
Deutsches Hydrographisches Institute  
Bernhard-Nocht-Strasse 78  
2000 Hamburg 4  
Postfach 220 GERMANY

Eduard Zuur  
Universite de Neuchatel  
Rue Emile-Argand 11  
Case Postale 2  
CH-2007 Neuchatel  
004138-243419 SWITZERLAND